

Light-Driven Selective Dissociation of Biomolecules

Victoria Rose Gabriele

A dissertation
submitted to the Faculty of
the department of Physics
in partial fulfillment
of the requirements for the degree of
Doctor of Philosophy

Boston College
Morrissey College of Arts and Sciences
Graduate School

April 2022

Light-Driven Selective Damage of Biomolecules

Victoria Rose Gabriele

Advisor: Krzysztof Kempa, Ph.D.

Abstract

It is well established that molecules can be driven to dissociation via ionizing radiation, and this has various uses in medicine. The drawback is that ionizing radiation has little spectral resolution when applied to the human body. Consequentially, ionizing radiation damages target biological cells and healthy biological cells indiscriminately. If a truly non-invasive and selective dissociation method is desired, it is necessary to consider non-ionizing radiation for additional specificity. The first part of this thesis proposes that a selective dissociation of biomolecules is possible with non-ionizing electromagnetic radiation on the basis of nonlinear driving of molecular resonances. The second part is devoted to a “Trojan horse”-type of strategy. Experimentally, we demonstrate that visible light at moderate power levels damages metastatic cancer cells when they are sensitized with biocompatible polymeric nanoparticles. Efficient photothermal conversion of nanoparticles triggers hyperthermia-induced lysis in cells in a target-selective manner.

TABLE OF CONTENTS

Table of Contents	iv
List of figures.....	vii
ACKNOWLEDGEMENTS	x
1 Introduction 1	
1.1 Introduction	1
1.1.1 Preamble	1
1.1.2 Electromagnetic Radiation Spectrum	4
1.2 Electromagnetic Dissociation of Biospecies	6
1.3 Direct Selective Damage of Biospecies via Non-Ionizing Electromagnetic Radiation	8
1.4 Selective Damage of the Nanoparticle Sensitized Target Biospecies via Non-Ionizing Electromagnetic Radiation	9
1.5 Outline of this Document	16
2 Equipment and Methods 17	
2.1 Equipment and Methods	17
2.2 Cell culture	17
2.3 Cytotoxicity Assays	18
2.3.1 Bioluminescent Imaging	18
2.3.2 Fluorescent Assay	18
2.4 Imaging and Nanoparticle Characterization	19
2.4.1 EVOS Fluorescent Imaging	19
2.4.2 Fixation	20
2.4.3 Z-stack Imaging	20
2.4.4 Electron Beam Imaging	22
2.5 Custom Cell Holder Preparation	23

2.5.1 Micro-Patterned PDMS Devices	23
2.5.2 Macro-Patterned PDMS Gaskets	24
2.6 Leica DMRE Microscope Set-Up with Laser Coupling	27
2.6.1 Discussion of Köhler Illumination	29
2.6.2 Adjustments for Laser Coupling to Microscope in an Optical Tweezers-Like Set-Up	31
2.6.3 Knife Edge Measurement Method	33
2.7 Photothermal Experiment Protocol	34
2.7.1 Laser Experiment Initialization	34
2.7.2 Cell Irradiation Measurement	35
3 Radiation Induced DNA Damage	37
3.1 Defining the DNA Model	37
3.2 Equation of Motion for DNA Model	40
3.2.1 Nonlinear Driving Term	43
3.2.2 Initializing the Model	47
3.2.3 Introducing a Driving Force	48
3.3 Amplitude-Frequency Dissociation of DNA Model	51
3.3.1 Temperature Effects on the Trace of the System	51
3.3.2 Model Robustness Under Thermal Fluctuations	54
3.4 Selectivity of Dissociation Domains	62
3.5 Discussion	64
4 Biocompatible Melanin Nanoparticles for Photothermal Therapies	65
4.1 Melanin Nanoparticle Photothermal Therapy	65
4.2 Overview of Nanoparticles in Medicine Toward Photodynamic Therapies	66
4.2.1 Brief Overview of Nanomaterials	66
4.2.2 Brief Overview of Photodynamic Therapy	67
4.3 Motivation: The Melanin Chromophore as a Photothermal Sensitizer ..	69
4.4 Material Characterization of Melanin	71
4.5 Melanin as a Biocompatible Selective Photothermal Agent	71
4.5.1 Governing Equations For Photothermal Study	80
4.5.1.1 Approximations on the Heat Equation	82

4.6 Melanin Nanoparticle Uptake	85
4.6.1 Cell Lines and Culture Conditions	85
4.6.1.1 VM-M3 and VM-NM1 Cell Lines	86
4.6.2 Melanin Nanoparticle Uptake	87
4.6.2.1 Nanoparticle Cytotoxicity Study	88
4.6.3 VM-M3 Nanoparticle Uptake Quantification and Comparison with VM-NM1	94
4.6.3.1 Nanoparticle Uptake Quantification Analysis:	94
4.6.3.2 Particle Uptake Analysis via ImageJ:	96
4.6.3.3 Orthogonal Measure of Particle Uptake with Electron Microscopy	98
4.6.3.4 Particle Uptake Discussion	100
4.7 Photothermal Experiment	100
4.7.1 Radiation Dose Characterization: Knife Edge Measurement ...	101
4.7.2 Photothermal Experiment Results	103
4.8 Study on Population of Cells	105
4.8.1 Device Fabrication	105
4.8.2 Fluorescent Data	109
4.8.3 Results	111
4.9 Discussion	113
5 Conclusions and Future Outlook	114
5.1 Conclusion	114
5.2 Summary	114
5.3 Future Outlook	116
5.3.1 In Vitro In Vivo Correlation for Melanin Nanoparticle Photothermal Therapy	116
5.3.2 Nanoparticle Applications for Chronic Inflammation	117

LIST OF FIGURES

1.1 Forecast of nano-medicine market growth	2
1.2 The Electromagnetic Spectrum	5
1.3 FIR absorbance spectra of influenza virus, normal human lung, and human cancerous lung cells NCI-H358	10
1.4 Absorption of Oxyhemoglobin, Melanin (unspecified), and water compared with the IPL Spectrum	13
1.5 Cartoon of light penetration into human skin	15
2.1 PDMS Spin Curve	26
2.2 Schematic of LEICA DMRE confocal microscope with custom modifications adjustments made for laser light-coupling	28
2.3 Schematic of conjugate focal planes required for Kohler illumination . . .	30
3.1 Molecular Structure of the DNA Molecule	38
3.2 Normalized total equilibrium potentials vs y	42
3.3 Amplitude-frequency space (AFS) for simple harmonic model SHM . . .	46
3.4 Amplitude-frequency space (AFS) response of molecule to external driving	49
3.5 Trace Under Different Potentials	52
3.6 Comparison of Trace for different potentials and temperatures	55
3.7 Amplitude-frequency space (AFS) response of AT and GC strands to external driving	57
3.8 Plot of Average Separation vs Frequency for low temperature, low frequency regime	59

3.9 Plot of Average Separation vs Frequency for low temperature, low to high amplitude regime	61
3.10 Histograms of the normalized incidents of damage	63
4.1 Absorption Spectra of Hemoglobin (Hb), oxyhemoglobin (HbO₂), Melanin (unspecified) compared with water	70
4.2 Melanin Synthesis Pathways	72
4.3 Absorption spectra of eumelanin pigments, both synthetic and naturally derived.	75
4.4 Concentration Dependent Optical Absorbance of Sepia Melanin	77
4.5 Characterization of Synthesized Melanin Nanoparticles	79
4.6 Cell viability over four days when incubated with different concentrations of synthetic, sugar coated melanin granules	89
4.7 Nanoparticle Concentration Dependent Cell Viability after 24 hours	91
4.8 EVOS fluorescent microscopy data	93
4.9 Selected slices from a Z-stack image of cells.	95
4.10 Image Thresholding Algorithm	97
4.11 Scanning Electron Microscope images of VM-M3 cells fed with nanoparticles	99
4.12 Knife Edge Measurement	102
4.13 Melanin-Containing VM-M3 cells before and 30 seconds after irradiation with a 532 nm laser at a power level of 121 mW	104
4.14 Custom Microfluidic through-holes in PDMS for mammalian cell isolation and tracking	106
4.15 Collagen and fluorophore auto fluorescence in PDMS deices interfering	

with fluorescent assay 108

4.16 Fluorescent Data on Gridded Coverslips from EVOS at 4x 110

4.17 Population of Cells post Treatment 112

ACKNOWLEDGEMENTS

This thesis is dedicated to my first physics teacher and grandfather, Peter M. Gabriele, whose encyclopedic knowledge of the world around him inspires me to this day. I would first like to acknowledge my advisor, Prof. Kempa, for endless interesting and motivating discussions. Your method for thinking about problems, weaving discussions and your physical intuition into back of the envelope calculations, and turning those calculations into experimental directions is a level of mastery I aspire to. Prof. Naughton, who was like a co-advisor, spent a great deal of time helping me develop as an experimentalist, and your input, understanding, and experimental intuitions continue to inspire me as well. Prof. Seyfried and Dr. Purna Mukherjee spent countless hours training and helping me develop an understanding of the underlying biological systems, and without their help this work would not be possible. I owe a great deal to the physics department, the physics administrators: Jane, Sile, Nancy and Scott, for always having our best interests at heart and facilitating our time at BC. I learned a great deal from both the official coursework and training, as well as unofficial time that professors dedicated to helping me throughout my time here. I would like to especially thank Prof. Bakshi, Prof. Rubin, and Prof. Wang for their willingness to dedicate time to fundamental subjects well outside of the allotted class periods. I would like to thank Prof. Graf for his care and deep consideration of our department and receptiveness to every voice during these especially difficult last two years. I owe the foundations of much of my lab training to Nate Nesbitt, Yitzi Calm, Luke D'Imperio, and Chaobin Yang. Prof. Burch, Yiping Wang, and Vincent Plisson were essential to helping me develop my experimental set-up as well. Finally, I would like to acknowledge Mark Schiller and Tyler Dodge for being excellent lab mates and group members, respectively. Finally, I would like to thank my mother, Paula Jo Gabriele, for raising me single handedly and supporting me throughout my entire graduate school tenure. I'd like to thank my grandmother, Rosemarie Gabriele, for her ongoing support throughout college and graduate life. I would like to thank the rest of my family, whose love and encouragement was always felt and helped drive me. Finally, I would like to thank Vincent for always supporting me. I could have done it without you, but it would have been a much lonelier experience.

Chapter 1

Introduction

1.1 Introduction

1.1.1 Preamble

Nanomaterials revolutionize modern medicine by providing new treatment modalities and enhancing existing therapies. They are utilized in a wide range of medical contexts including medical imaging, targeted drug delivery, diagnostics, and therapies [1]. Applying nanomaterials toward therapeutic aims is the goal of the nanomedicine industry, which has grown both in the United States and globally. In the United States, nanomedicine related research and industries are a fast growing market, and its growth is forecast to continue, as shown in Figure 1.1.

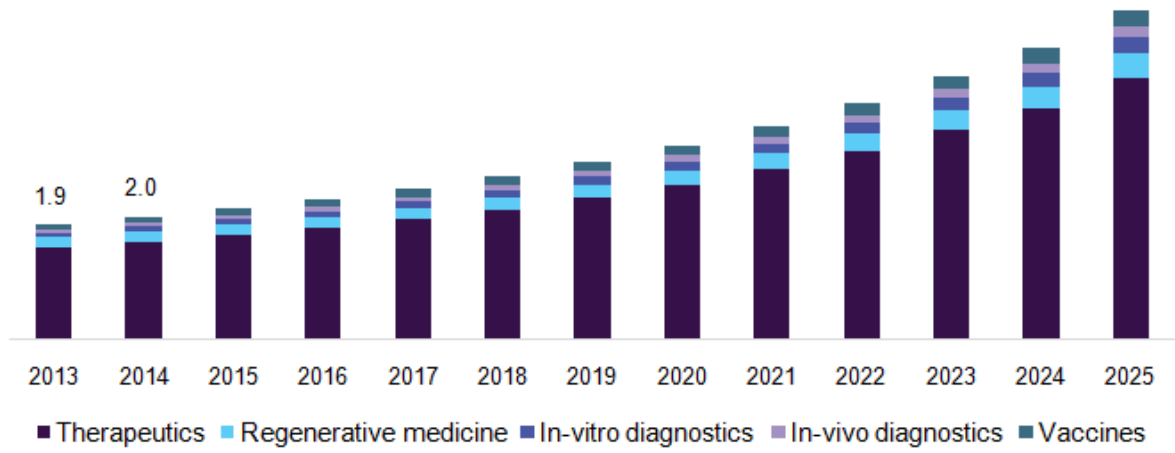


Figure 1.1: *Forecast of nano-medicine market growth*

[1]

The development of nano-medicines requires an interplay of physics at the nanoscale, chemistry, and biology to form successful therapies. Nanomaterial-based medicine comprises various materials including liposomes, micelles, polymeric nanoparticles, nanocrystals, dendrimers, and even metallic or composite nanoparticles. The treatment modality can be inherent to the nanomaterial as is: for example, enhancing MRI contrast or treatment [2], delivering selective hyperthermia known as photothermal therapy (PTT) [3]; or the nanomaterial may work in tandem with existing pharmacokinetic systems by repackaging existing drugs within a functionalized nanoparticle surface. The latter enhances selectivity and uptake, which lowers general toxicity [4] [5].

Within the umbrella of nanomedicine, this thesis work centers on coupling of electromagnetic radiation to biomolecules towards therapeutic aims. The specific focus is the coupling of light with existing biological organisms or bio-compatible materials, toward selective dissociation of the targeted species.

It is necessary to first survey the existing landscape electromagnetic radiation in medicine. Ionizing-radiation based therapies dominate current medical treatments, and the advantages and downsides to this will be defined and explored in later sections. This work explores potential treatments that aim to damage biomolecules directly and selectively with non-ionizing radiation through nonlinear effects. First, a theoretical work is highlighted which demonstrates how non-ionizing radiation could lend itself to label-free selective dissociation of biomolecules [6]. While theoretically compelling, there are serious limits to the practicality of this approach. Experimental challenges to this method which will be discussed explored further. After considering biomolecule-based targeting of non-ionizing radiation from a theoretical framework, we turn to an exploration of a biocompatible nanoparticle, melanin, and how it can be utilized in conjunction with a non-ionizing ra-

diation therapy in an experimental demonstration of selective thermal damage to cancer cells [7].

1.1.2 Electromagnetic Radiation Spectrum

Electromagnetic radiation exists on an energy-dependent spectrum from lower energy longer wavelengths to higher energy shorter wavelengths. This spectrum is shown in Figure 1.2 in terms of frequency and wavelength, as well as common classifications for different ranges (ie, “visible light”).

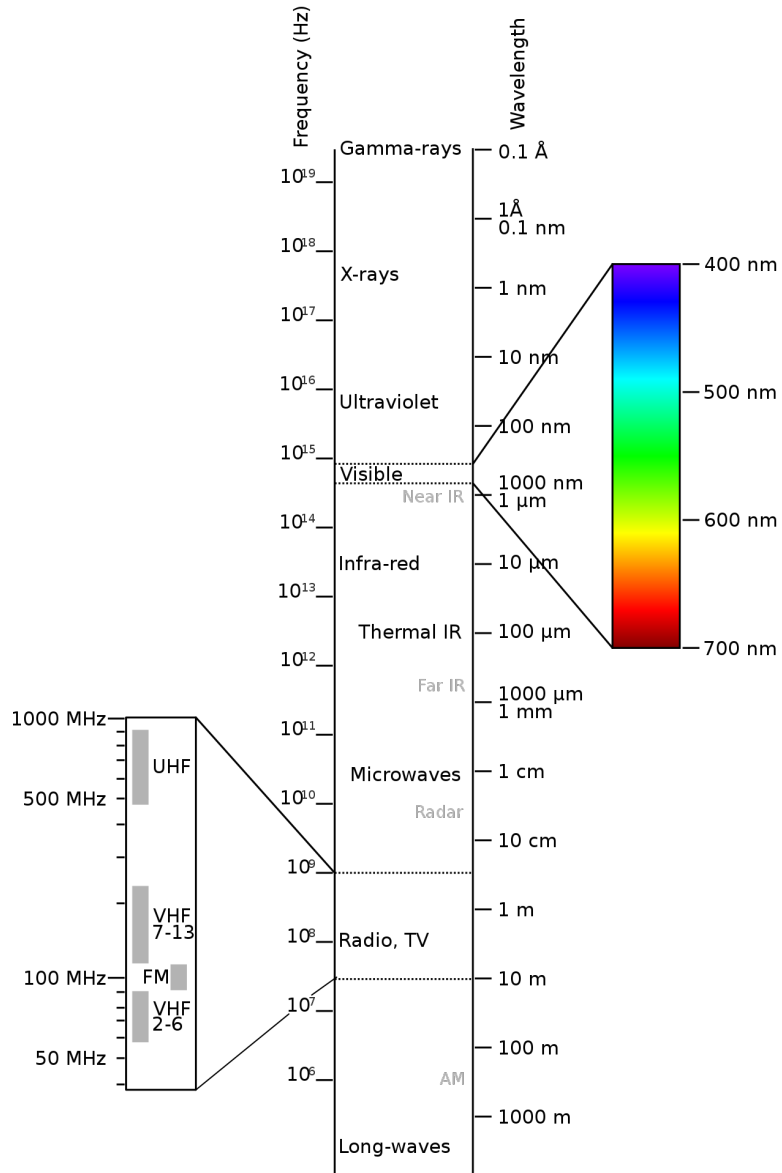


Figure 1.2: *The Electromagnetic Spectrum*

[8]

Ionizing radiation is electromagnetic radiation that has sufficiently high energy to ionize molecules, while radiation whose energy is below this threshold is non-ionizing. In Figure 1.2 ionizing radiation corresponds to high energy radiation from Gamma rays to ultraviolet (UV). The transition from ionizing to non-ionizing radiation is within UV, though precise energy required to ionize specific molecules is material dependent. When applied to biological systems, ionizing radiation can be lethal to living organisms [9]. While ionizing radiation has many uses in medicine [10] [11], this thesis focuses on the study of molecular and/or cellular dissociation of bio-molecules via non-ionizing radiation.

1.2 Electromagnetic Dissociation of Biospecies

It is well established that molecules can be driven to dissociation via ionizing radiation. However, such methods have little spectral resolution. In medical contexts, human cells, cancerous and healthy alike, experience damage when exposed to ionizing radiation therapies [12]. Most attempts at selectivity come from geometric lensing of the ionizing radiation: for example, focusing a high energy beam to terminate within a tumor. During this process, skin and other healthy tissues that the radiation passes through will necessarily also be damaged [9] [12] [13]. The primary difference between thermalizing damage induced by non-ionizing radiation, and the indiscriminate breakage of chemical bonds from ionizing radiation is that the intensity and power density of non-ionizing radiation can be finely controlled to prevent toxic effects. Radiation therapy is part of the current standard of care for effective cancer treatments, but it is necessary to consider non-ionizing radiation for additional specificity if a truly non-invasive, non-toxic and selective dissociation method is desired. Localized increases in temperature can, in principle, be an additional avenue of therapeutic damage via non-ionizing radiation. If

the temperature increase from the induced thermal field is 1) sufficient to cause permanent denaturation of proteins or induce similarly irreparable damage in cells 2) highly localized such that nearby cells and tissues are undamaged then this is a further avenue for non-ionizing radiation based selectivity.

Within the category of non-ionizing radiation, there are distinct energy ranges which each have their own advantages and disadvantages to consider for driving selective dissociation. The upper energy limit for non-ionizing radiation is the optical range of light, indicated by color in Figure 1.2. Various naturally occurring biospecies absorb light in this range. In the body, these are typically polymeric macromolecules called chromophores. Under some conditions, chromophores can couple to visible radiation in such a way to induce rapid thermalization, which would have a dissociating effect on molecules that make up cells in its microenvironment. However, optical light does not penetrate deeply into human tissue. Near-infrared radiation (NIR) (800 nm - 2.5 μm) overcomes this limitation due to its relative transparency to skin and water, the external components of the human body. Below a certain power density, NIR is also non-toxic. NIR in medical contexts is applied to selective dissociation of tumors, though this current method often requires enhancement via the presence of an absorbent particle [14]. Near-infrared radiation can also induce dissociation of biological cells in a micro-targeted way via an optical tweezers set-up [15]. However, the dissociation effect here is due to the mechanical stress on the cell from the optical tweezers trap, and without this geometric lensing, NIR remains transparent to the organism. To find radiation that couples to biomolecules in a tunable and frequency selective way, it becomes necessary to look further along the spectrum.

The ‘fingerprint region’ ($\sim 6.6\text{-}25 \mu\text{m}$) is the energy range where vibrational modes from carbon-based life forms are activated, and their unique signatures, or ‘fingerprints,’ are

used to identify chemical components. In this window we find that biological components, such as individual proteins, become selective absorbers themselves, rather than larger aggregates such as macromolecules [16]. In contrast to NIR transparency, many biological organisms are naturally self-sensitized by mid infrared radiation (MIR).

Though there is sufficient coupling of vibrational modes of biomolecules to MIR, the difficulty of MIR based treatments is the significant overlap of biomolecular building blocks, even across different species. Finally, we must consider role of water in this range, which is highly damping in this range, and serves to act as a non-selective reservoir of heat when absorbing MIR.

The impact of even longer wavelength radiation, such as far infra-red (FIR) and THz ranges is a final approach to consider. There is currently rich discussion within the scientific community regarding the impact of THz radiation on complex biological organisms [17]. This requires a highly specialized approach, where selectivity comes in demonstrating fine resolution between dissociation and linear resonances. One experimental application of this has been toward biomolecule DNA, where radiation in the THz regime resulted in non-thermally induced changes in gene expression [18]. This dissociation is driven by molecular resonances, which has the potential for high selectivity, though it is experimentally challenging.

1.3 Direct Selective Damage of Biospecies via Non-Ionizing Electromagnetic Radiation

Radiation along the ranges outlined in the previous sections has some established uses in medicine. Non-ionizing radiation is utilized medicine for both electrical stimulation [19]

[10] [20] as well as ablation therapies, where the primary mechanism for dissociation is rapid thermalization [21].

Chapter 3 of this work demonstrates via simulations that a selective dissociation of biomolecules is tenable with electromagnetic radiation driving non-linear molecular resonances in the THz regime. Specifically, we do not address the details of the chaotic dynamics that develops near the dissociation domain boundary in the THz regime applied to a biomolecular simulation, but instead focus on the universality of dissociation conditions. This includes the fact that the trace of a resonance in the stable domain of the amplitude frequency space connects to the minimum of the corresponding dissociation domain boundary, which implies high spectral resolution of the dissociation near this minimum, a fact of potential importance for applications.

1.4 Selective Damage of the Nanoparticle Sensitized Target Biospecies via Non-Ionizing Electromagnetic Radiation

A purely spectral selectivity of molecular dissociation would be highly desirable in future therapies, but it is experimentally intractable due to the spectral overlap of distinct biomolecular components. The building blocks that make up viruses, cancer cells, and human cells have overlapping spectral resonances in the mid and far infrared, and are distinguished only by amplitude variations. Figure 1.3 demonstrates the problem.

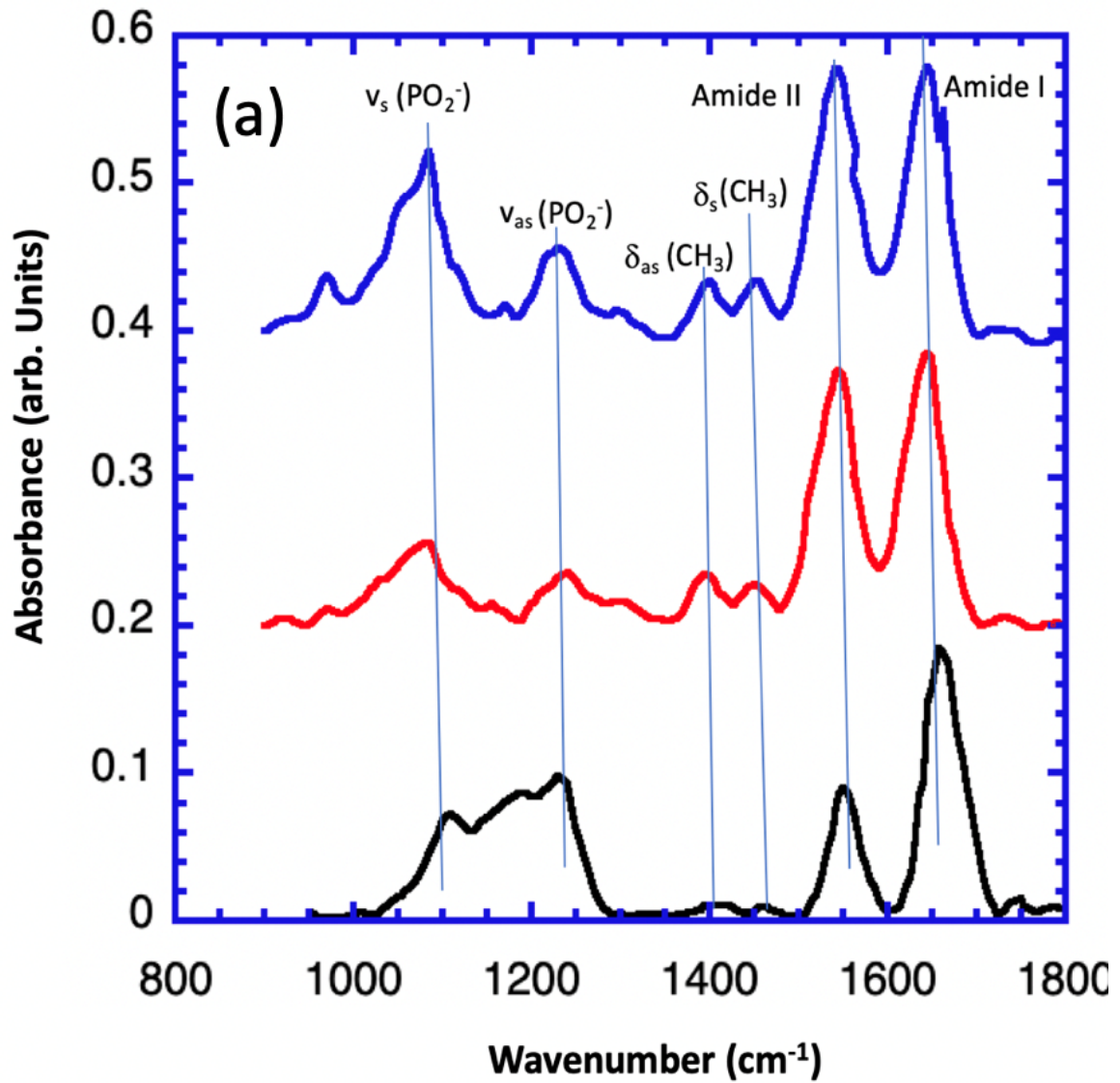


Figure 1.3: *FIR absorbance spectra of influenza virus, normal human lung, and human cancerous lung cells NCI-H358*: Influenza virus shown as bottom black curve, extracted from [22], and normal human lung bronchial epithelial cells (middle red curve), and human cancerous lung cells NCI-H358 (top blue curve), both extracted from [23] and offset for convenience.

[22] [23]

Figure 1.3 shows where in the infrared absorption spectra of human and non-human viral cells overlap due to resonances of their molecular building blocks. The bottom (black) curve is the absorbance spectrum of an influenza virus taken from [22], and the middle (red) and top (blue) curve are the spectra of normal and cancerous lung cells, respectively, taken from [23]. Each spectra is normalized to the amide I peak, and offset for clarity. Frequency locations of the dominant spectral peaks are essentially the same for all spectra, even though distinct species are involved. Even within the same species (healthy and cancerous lung cells), there are clear relative magnitude differences at the common peaks which nonetheless could be exploited in therapeutic strategies. Because the differences are small, a simultaneous agitation at multiple spectral locations might be required to achieve sufficient cumulative, target molecule excitation. Such a scenario would require high power, spectral-shaped (with multiple monochromatic channels), highly controllable radiation sources, possibly in the wide electromagnetic spectrum range from visible to microwave.

Many radiation therapies must first pass through skin to reach internal organs, so penetration depth through this organ must be considered. We see in Figure 1.4 that the biopolymer and naturally occurring chromophore melanin is broadly absorbing across the optical spectrum, an observation that will be discussed further in chapter 4. Melanocytes in the human epidermis produce melanin, and these cells also contribute to the diversity of human skin phototypes—where concentration of melanin and activity of melanocytes have a major influence on light penetration depth and absorption [24]. Blood is another significant absorber of radiation, and the spectrum of oxygenated blood is shown in Figure 1.4 as the red line labeled Oxyhemoglobin. We see that oxyhemoglobin is highly reflective in the range of red light, and highly absorbing in shorter wavelengths, and

continues to absorb through the mid infrared. Water, which plays a prominent role in human tissue, is optically transparent but begins to absorb beyond 800 nm, becoming more highly absorbing the further along in infrared.

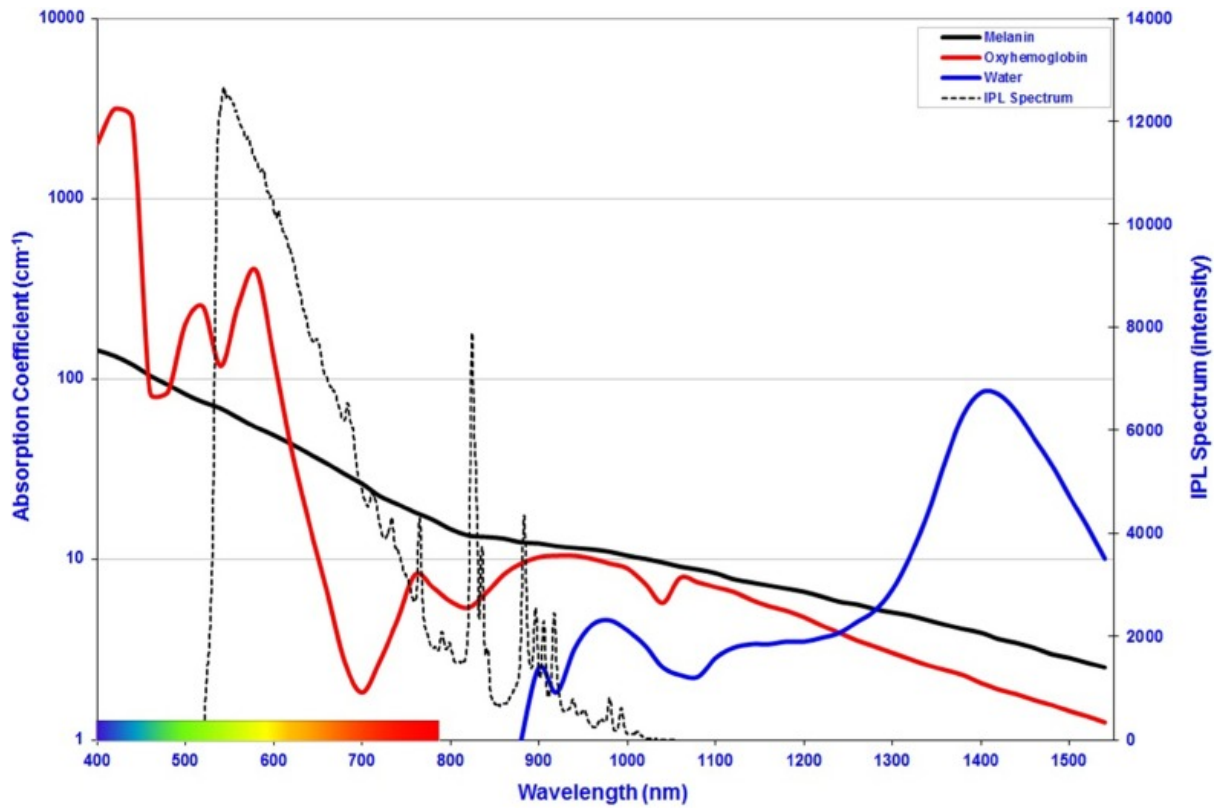


Figure 1.4: *Absorption Spectra of Oxyhemoglobin, Melanin (unspecified), and water compared with the IPL Spectrum*: The optical absorption spectra of prominent naturally occurring chromophores: oxyhemoglobin and melanin compared with water. These are common naturally occurring chromophores in skin tissue, and they are compared with the intense pulsed light (IPL) spectrum. IPL is a broad spectrum between 400-1200 nm, which targets desired chromophores in the skin for cosmetic and therapeutic purposes.

[19]

The absorption of selected chromophores in skin is shown in Figure 1.4, while a cartoon of penetration depth shown in Figure 1.5 compares optical and near infrared radiation through the epidermis.

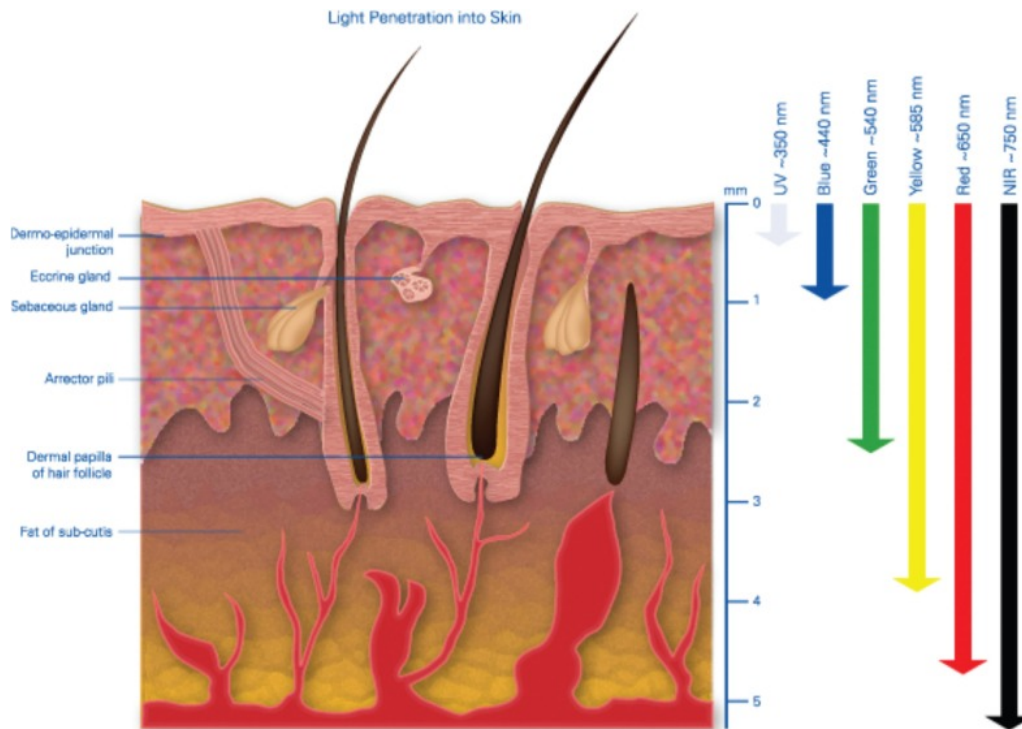


Figure 1.5: *Cartoon of light penetration into human skin:* This figure illustrates experimentally determined penetration depth of different wavelengths of light on a subset of human skin known as Fitzpatrick Type II [19]. The Fitzpatrick scale is a subjective classification based on the reaction of skin to sunlight, influenced both by ethnicity and sun exposure, but may not be safe for treatments due to inconsistency [24]. Historically, it has been used as dermatological measure for which skin color is graded, ranging from 1 -6 going from light to dark. The data that this cartoon is based on is qualitatively useful only to demonstrate that NIR radiation penetrates more effectively than optical radiation. It is important to note that this data is limited to a subjective assessment of fairer skin, and the penetration depth in darker skin types was not included or studied [25].

[19] [24] [25]

The challenge of low absorption could be avoided by radiation tuned to resonance frequencies of proper nanoparticles embedded in into target cells. Firstly, the nanoparticle absorption could be maximized in the spectral window, and thus could take the full advantage of the large radiation penetration. Secondly, the large absorption of the nanoparticle would minimize the required radiation power to achieve target cell dissociation without damage to healthy cells. The second part of the thesis is devoted to such a “Trojan horse” strategy. Experimentally we demonstrate [7] that visible light at moderate power levels kills metastatic cancer cells, filled with melanin nanoparticles. We show theoretically and experimentally, that cell death occurs in this case via hyperthermia-induced lysis, and we found this process to be target-selective, as nonmalignant cancer cells studied here that could not ingest the melanin nanoparticles remain unaffected, despite receiving identical optical energy levels and doses. This technique could enhance a future cancer metastasis preventing therapy.

1.5 Outline of this Document

The structure of the thesis is as follows: Methodology and all equipment used is outlined in chapter two. Chapter three explores a physical model of the DNA molecule and it’s unique and selective response to non-ionizing radiation, specifically in the THz regime. Chapter four discusses light coupled with biocompatible nanomaterials in mammalian cells. Specifically, the fourth chapter explores melanin as a highly efficient photothermal therapy for tumor cells. The final chapter concludes this work and proposes further potential experiments based on protocols outlined here, and how they may be adapted to biological systems for tuning of macrophage phenotype.

Chapter 2

Equipment and Methods

2.1 Equipment and Methods

2.2 Cell culture

Cells in suspension were obtained from the Seyfried lab (Boston College). The cells were on passage 22 and transferred to a 100 mm Petri dish containing Dulbecco's Modified Eagle medium (DMEM, Sigma, St. Louis, MO) with high glucose (25 mM) supplemented with 10% fetal bovine serum (FBS, Sigma) and 50 $\mu\text{g}/\text{ml}$ penicillin-streptomycin (Sigma). The cells were cultured in a CO₂ incubator with a humidified atmosphere containing 95% air and 5% CO₂ at 37°C.

For photothermal experiments, cells are removed from the dish using a cell scraper in the case of VM-M3, or using Trypsinisation in the case of VM-NM1, and re-seeded in a custom cell holder.

2.3 Cytotoxicity Assays

Toxicity assays were used to determine the health of cells after various treatments using chemical and microscopic analysis.

2.3.1 Bioluminescent Imaging

For *in vitro* growth analysis of cells in response to nanoparticle cytotoxicity, approximately 50,000 cells were seeded in a 24-well plate and cultured as described above. Cells were analyzed 24hours after seeding using the Xenogen IVIS system (Caliper LS, Hopkington, MA). The IVIS Lumina cooled CCD camera system was used for light acquisition.

Data acquisition and analysis was performed with Living Image® software (Caliper LS). For imaging, 20µl of a 300 µl/ml D-luciferin (Caliper LS) solution was added to each well in PBS and the plates were imaged for 3 minutes. Following imaging, the media was changed in the well and fresh DMEM was added, or the cells were discarded if this was an endpoint measurement.

2.3.2 Fluorescent Assay

To evaluate nanoparticle cytotoxicity, nanoparticles were prepared as follows. Particles were first suspended in DI water and subsequently autoclaved for sterilization for 30 minutes (wet cycle). Steralized nanoparticle solutions was suspended in DMEM at the following concentrations, dependent on the volume of the 96 well plate.

To determine cytotoxicity, the Live/Dead Cell Staining Kit II (PromoKine: PK-CA707-30002) was employed according to manufacturer's instructions. Briefly, live cells take up Calcién-AM in the cytoplasm, which is excited by ~495 nm and emits in the ~515 nm

range. Dead cells are labeled with EthD-III, a nucleic acid stain that is not permeabilized in healthy cells, which is excited around ~530 nm and emits ~635nm. Their relative absorbance were collected by Spetromax M5 plate reader (SpetraMax, M5; Molecular Devices, CA), and cells were visually inspected via EVOS fluorescent microscope. An initial concentration of VM-M3 cells were suspended in DMEM and seeded to a 96 well plate at a concentration of 10,000 cells/well for 24 hour investigation; 5000 cells/well for 48 hour investigation; and, finally 2500 cells/well for 96 hour investigation.

2.4 Imaging and Nanoparticle Characterization

2.4.1 EVOS Fluorescent Imaging

In addition to spectrophotometer readings, live cells were also imaged with fluorescent dye. Cells were grown either in on coverslip or in a plate.

Live/Dead Cell Staining Kit II (PromoKine: PK-CA707-30002) was employed according to manufacturer's instructions. Briefly, cells were washed 3x with PBS. Calciin-AM and EthD-III were added to PBS of sufficient volume to cover cells, at a concentration in accordance with manufacturers instructions for imaging, and vortexed before adding to the plate. Cells were incubated for 15 minutes to take up dye, and then brought to the EVOS fluorescent microscope. Live cells take up Calciin-AM in the cytoplasm, which is excited by ~495 nm and emits in the ~515 nm range. Cells were first imaged using white light and a phase contrast objective. The setting was then changed on the EVOS to the 'GFP' channel, which excites the sample via blue diode. The emitted light is then filtered to collect green signal, and this image was saved separately. Dead cells are labeled with EthD-III, a nucleic acid stain that is not permeabilized in healthy cells, which is

excited around ~530 nm and emits ~635nm. To collect signal from dead cells, the EVOS was manually changed to the ‘Texas Red’ setting, where the sample was excited via a green diode, and the emitted signal was filtered to collect red light. For photothermal experiments, the grid was captured at 4x magnification, and intensity was kept constant across different imaging channels. Visual overlay of the white, green, and red channel signal was accomplished via ImageJ software post-processing, though it is also possible to generate a fluorescent image overlay directly with the EVOS software.

2.4.2 Fixation

The following protocol was used to fix cells to coverslips prior to imaging:

- Mix at a ratio of 4% paraformaldehyde with filtered, sterilized PBS, store in fridge or cold room
- Remove cells from incubator and wash 3x with PBS if in serum containing media.
- Aspirate cells in PBS and replace with chilled solvent containing 4% EM grade paraformaldehyde in PBS. This will cross-link proteins within cells, maintaining approximate morphology.
- Leave cells immersed in formaldehyde-PBS mixture in the dark at room temperature for 20 minutes.
- Then aspirate PBS-paraformaldehyde mixture and replace with PBS. Store plate in fridge or cold room in the dark.

2.4.3 Z-stack Imaging

Coverslips were cleaned using 70% w/v ethanol in DI water. They were then coated with Type I Rat Collagen (Sigma-Aldrich, C3867) according to manufacturers protocol, and

sterilized under UV light for ~30 minutes under a cell culture hood.

Cells were seeded in a 6-well plate. After growth to approximately 60% confluence, existing media was aspirated and replaced with media containing melanin nanoparticle solution. Nanoparticles were mixed with DMEM at the concentration matching laser experiments and each well was given 3 mL of solution. Cells were incubated with melanin particles 24 hours, and then removed from the plate via scraping.

Cells were centrifuged, washed, and re-seeded in a fresh 6-well plate that containing collagen-coated coverslips at the bottom of the plate. Cells were fed fresh media and left to adhere to the coverslip overnight.

After 24 hours, coverslips containing cells were removed from the 6 well plate and washed 3x with PBS. Cells were then fixed onto coverslips using 4% para-formaldehyde.

After fixation, all liquid was aspirated, and the coverslip was irreversibly fixed to a cleaned microscope slide using prolong gold solution.

Cells were imaged with Axioimager Z2 confocal fluorescent microscope, complete with automated piezoelectric stage to allow for precise imaging control in X- Y- and Z- directions. Images were recorded in 'z-stack' via Zeiss ZEN software and analyzed in ImageJ. Z-stack arrays were obtained by programming in the software two focus points, and a step size to interpolate between. The bottom and top of selected cells were focused on, and then an automated array of images between the top and bottom points was recorded via Zeiss software. Slices of the upper, mid, and lower sections of the cell were used to evaluate particle uptake and location within the cell.

2.4.4 Electron Beam Imaging

For electron beam imaging, either Scanning Electron Microscope (SEM) or Focused Ion Beam (FIB), the preparation is as follows:

- Grow cells on desired substrate (Si chip, Au-coated Si Chip, Glass coverslip) in a plate
- Remove cells from incubator, and aspirate any serum-containing media. Serum has additional components that will leave a residue on the image, so they need to be removed. Replace serum media with phosphate buffered saline (PBS). Repeat PBS wash 3x.
- Cells were fixed with 4% EM grade paraformaldehyde
- For better contrast, staining with polymer-binding electron imaging contrast agents, such as Uranyl acetate, OsO_4 or others (not done in this investigation)
- Perform a dehydration series with a solvent: prepare a solvent at a ratio of 10:90 PBS:Ethanol. Aspirate existing PBS and replace with solvent containing ethanol. Let sit at room temperature for 10 minutes. Repeat at a ratio of 20:80, 30:70... until a ratio of 100:0 is achieved (fixed cells are fully submerged in ethanol). This slowly replaces the water in the cells with alcohol.
- Dry: Allowing evaporation from surface would produce artefacts at the sample surface due to the surface tension of the evaporating ethanol with the specimen. To prevent this, dry using a critical point dryer (cleanroom).
 - Alternatively, drying can be achieved with HMDS (not tried in this investigation)
- Once dried, cells are ready to image. If substrate is highly insulating, an optional step is to coat substrate with a thin layer of Au (3-5 nm) using a benchtop plasma

sputter system.

2.5 Custom Cell Holder Preparation

Cells were isolated using either micro-patterned or macro-patterned Polydimethylsiloxane (PDMS) partitions (Dow Sylgard-184 Silicone Elastomer Kit, NC9285739, Fisher Scientific)

2.5.1 Micro-Patterned PDMS Devices

- Mix the curing agent with the silicone

In a clean space or dust free environment, measure the length, height and width of the microfluidic device mold and multiply to yield its volume. Width of a standard Si wafer is assumed to be 0.6 cm. Determine the amount in grams of PDMS needed to fill the mold by multiplying volume by density - the density of PDMS is $0.97g/cm^3$. Mix the silicone and curing agent at a 1:10 ratio.

- Degas the mixture

Pour the mixture into a mold, and then degass any bubbles in the mixed PDMS using a desiccator connected to a vacuum pump, periodically pumping down the system and bringing to atmosphere to pop any bubbles that come to the surface.

- Cure the PDMS to the mold

Transport the covered mold to a hotplate heated to 100 C and heat for 35 minutes. Then, allow to cool in fume hood for at least 5 minutes.

- Attach to glass device

Sterilize and clean of debris a microscope slide or coverslip prior to PDMS adhesion. Once PDMS has cooled and is hardened to the wafer, use a scalpel to cut a rectangle with the pattern on it out of the mold. The area of the rectangle should be smaller than the desired adhesion surface. Be careful not to interrupt any of the channels in the pattern when cutting.

If micro-channels require it, punch any holes through the device. Clean the tip of the 1mm hole punch with isopropyl alcohol (IPA), then rinse with water. Blow pressurized air on the hole punch to get rid of moisture. Place the rectangle of PDMS on a cutting mat, pattern side up. Pierce holes into the PDMS rectangle using a 1mm diameter hole puncher where it is indicated on the pattern. Clean PDMS with IPA or ETOH. Blow pressurized air at an angle to dry device.

Functionalize the surface of the PDMS and coverslip via 30 seconds in a microwave plasma chamber. Immediately place the micropatterned PDMS in order to adhere it to the glass. To avoid air bubbles in the PDMS pattern, take the PDMS rectangle and slowly roll it onto the glass slide. Let sit for 2-3 minutes, applying some pressure to promote even adhesion.

- Sterilize

Sterilization can occur by flowing 70% ethanol through the device, and flushing with PBS prior to use. Alternatively, 30 minutes of UV sterilization can be used, but this may negatively impact adhesion

2.5.2 Macro-Patterned PDMS Gaskets

For PDMS gaskets, it is necessary to prepare a thin layer of PDMS.

- Prepare Si Wafer with Sacrificial Layer

First, clean a standard Si wafer. Spin a layer of positive photoresist and softbake to cure the photoresist, according to manufacturers instructions.

- Prepare PDMS for spin coating

Mix curing agent at a 10:1 ratio as described in the previous section. Degas mixed PDMS in a desiccator, for not more than 20 minutes.

- Spin coat PDMS according to desired thickness, in this experiment approximately $50\mu\text{m}$ was achieved by spinning at 1,200 rpm for 5 minutes.

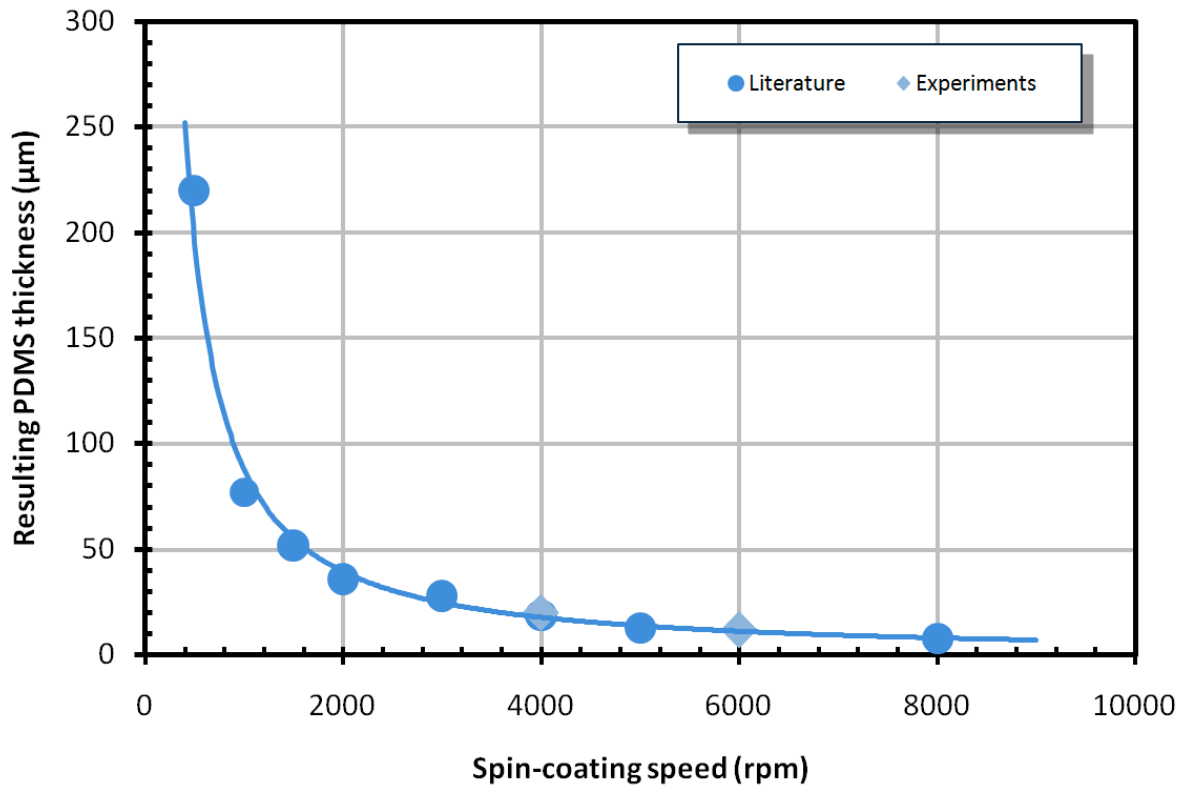


Figure 2.1: *PDMS Spin Curve from Eveflow Technical Note*

[26]

Cure PDMS membrane until it is cohesive. To release the PDMS membrane submerge the wafer in acetone until the sacrificial photoresist dissolves and the membrane floats to the surface. Transfer the membrane to IPA and cut to desired size. Punch a 1 cm hole in membrane and lay membrane over gridded coverslip, making sure to center the grid in the hole-punched area. Flatten the membrane onto the coverslip using gentle pressure and IPA. Place in plasma etch chamber to promote adhesion, as in the previous section, and then bake for at least 4 hours at 90° C. The chips are now ready for sterilization and collagen coating.

2.6 Leica DMRE Microscope Set-Up with Laser Coupling

The experimental set-up consists of a Leica DMRE confocal florescent microscope. There are various iterations of this set-up, and they shall be discussed in order that they were arranged. A 532 nm solid state laser was coupled to the back aperture of the microscope objective lens. The following schematic, adapted from [27] conveys the light path of the laser.

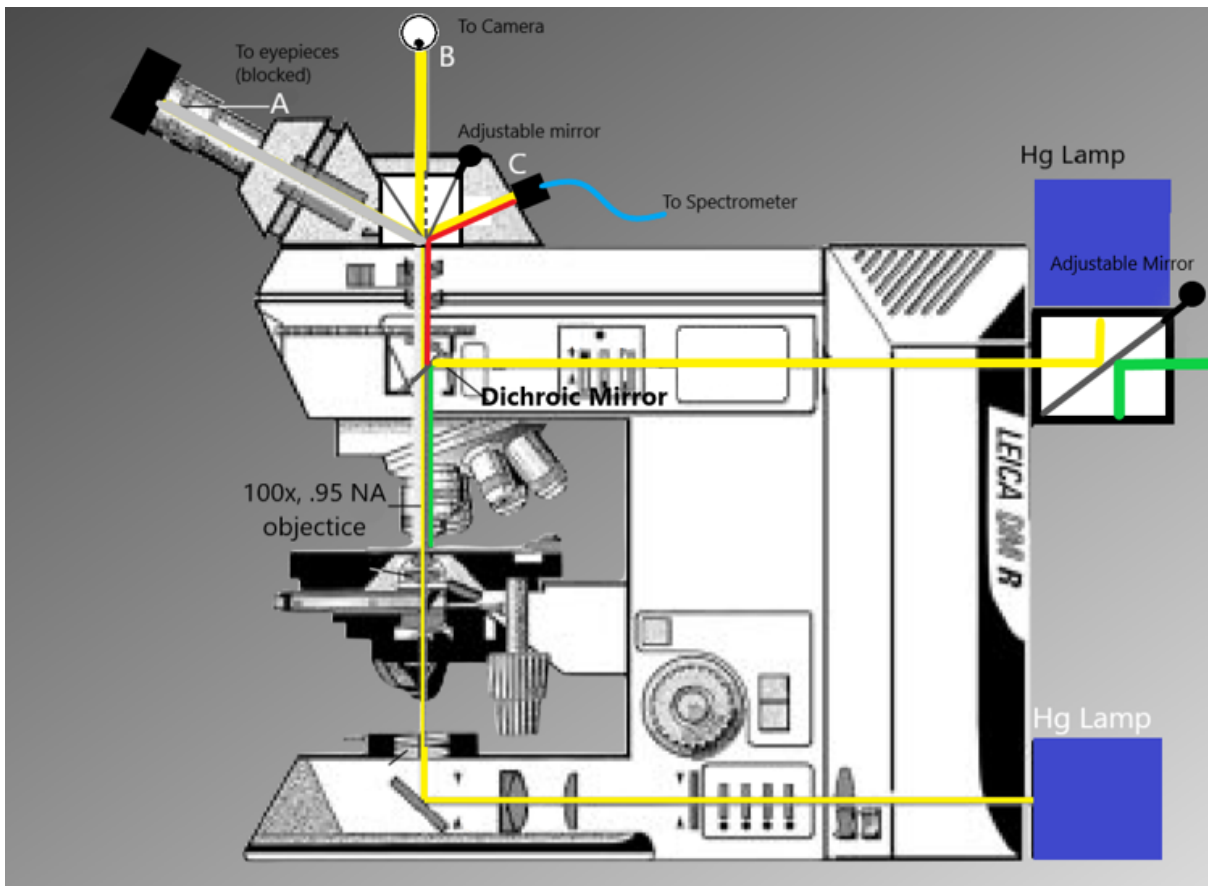


Figure 2.2: *Schematic of LEICA DMRE confocal microscope with custom modifications adjustments made for laser light-coupling*

[27]

2.6.1 Discussion of Köhler Illumination

The principle of Köhler illumination is to set-up separate conjugate focal planes for both the specimen being illuminated and the image of the filament. This ensures that the image of the lamp filament is not present or overlaid on the image of the specimen. This ensures bright and even illumination, and it is how many modern microscopes are configured.

One example schematic of conjugate focal planes in Köhler illumination is given below in Figure 2.3, adapted from Zeiss website [28]:

Conjugate Focal Planes in the Microscope for Köhler Illumination

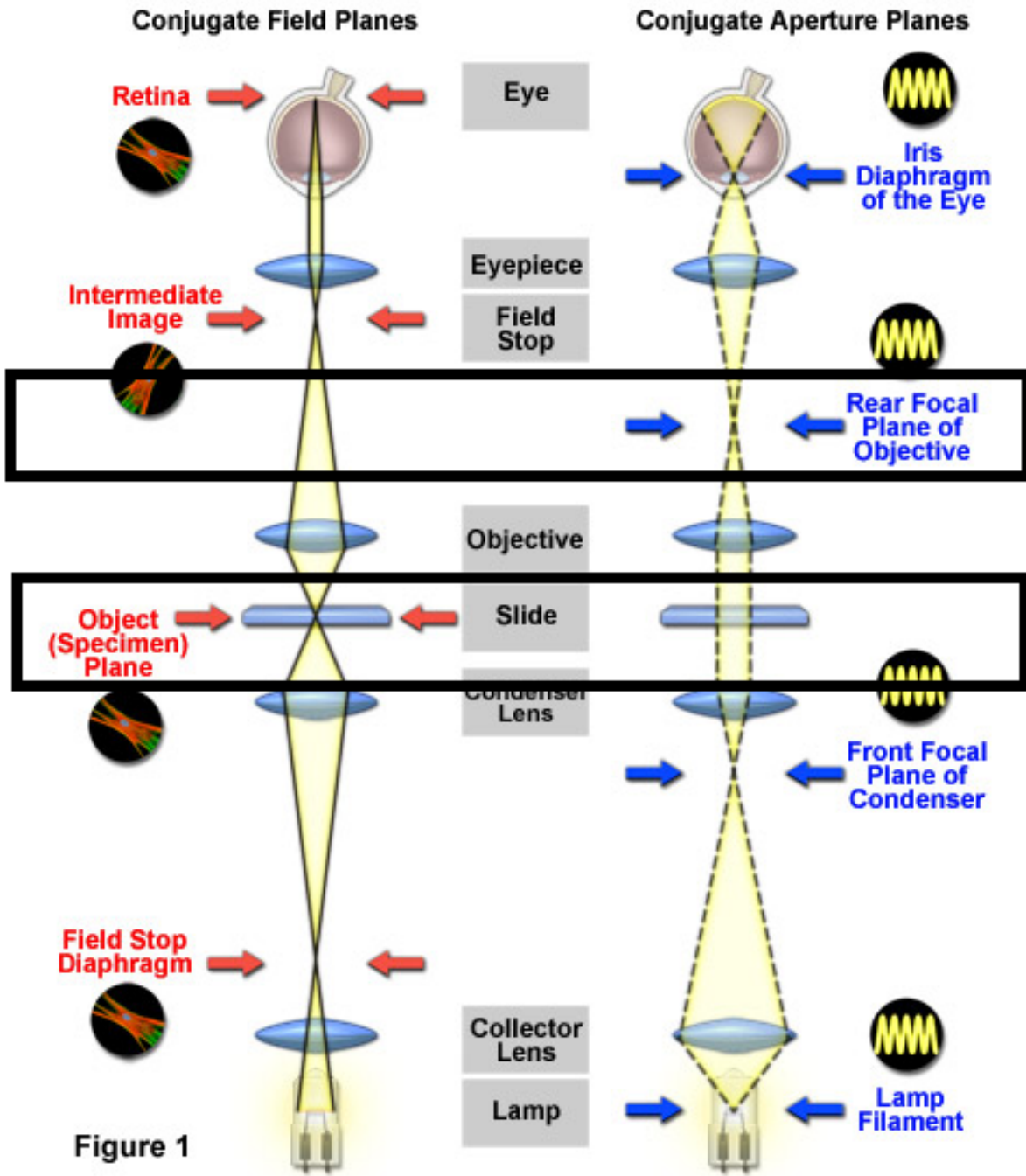


Figure 2.3: *Schematic of conjugate focal planes required for Kohler illumination*

[28]

This design consists of one transmitted light illumination set-up, but is divided in two in order to show the conjugate focal planes. On the right hand side we see that the image of the lamp filament is collected via the collector lens and focused to an intermediate point between the front focal plan of the condenser. The condenser expands this image and we see collimated light passing through the specimen plane. Collimated light entering the specimen plane is focused through the objective onto the back aperture of the objective. This passes through another lens and the filament is focused again onto the iris diaphragm, which controls the intensity of light to the eyepieces or camera. Focusing at this point allows the beam to diverge when it passes through the eyepieces and the diaphragm of the eyepieces are not imaged on the camera.

Meanwhile, the outer rays from the bulb, traced on the right hand side of the figure, are focused at a closer intermediate point and then expand until they reach the condenser lens. The condenser focuses these rays onto the sample. The focused spot reaches the objective and emerges filling the back aperture of the objective. An intermediate image is formed at the field stop and focused onto the eyepieces.

2.6.2 Adjustments for Laser Coupling to Microscope in an Optical Tweezers-Like Set-Up

The following discussions will focus on reflected light imaging mode. Though the geometry of the set-up is different than transmitted light, the principle of Köhler illumination still applies. To create an optical tweezers-like set-up with a laser incident on a cell, it is necessary that the beam is focused to a tight spot on the sample. We employ an optical tweezers-like focused beam spot for dose consistency, ease of measurement, as well as maximal energy density. It is clear from the image that light focused to a tight spot on

the back aperture of an objective results in collimated illumination, while a beam that fills the back aperture of an objective is focused tightly.

For optical tweezers set-ups, beam expanders are usually employed to expand the collimated beam, such that a larger diameter of collimated light is incident on the objective in order to fill the back aperture of the objective. This is necessary because the force from the optical tweezers comes from the sum of the y-components of light out of the objective, and this force generally increased with higher NA. For our purposes, having light focused to a tight spot to ensure controlled dose is sufficient, the force of the radiation is irrelevant, so beam expanders were not employed. Instead, the two tube lenses meant for proper Köhler illumination by focusing collimated light to the back aperture of the objective were removed. Because laser light is already collimated, it was only necessary to align the beam in such a way that the already-collimated laser light was incident and centered on the back aperture of the objective.

The optics designed for a fluorescent microscope lamp illumination are generally exceed the size of a 532nm laser beam, so this alignment was non-trivial. The microscope was set on a vibration-isolated optics bench, with holes drilled at regular intervals for additional optics components. The microscope was secured to the table using a custom-made holder, with special care that the fan was not blocked. Four mirrors were set on kinematic mounts at identical heights in the z-direction, connected by a cage system to assist with alignment. One iris was set in between the first two mirrors in order to ensure that the beam was not at an angle relative to the mirror's centers along it's path. The mirrors were placed in the center of the microscope system. One additional mirror was set directly above the other using cage plates, at approximately the height of the center of the fluorescent epi-illumination microscope port.

Mirrors were arranged in 45° kinematic mounts, and aligned in the z-direction with a cage system. This series of mirrors on kinematic mounts allowed for micro-adjustments of the beam center. The beam was walked from its position on the optics table into the epi-illumination port of the microscope. It was approximately centered on the dichroic mirror until the beam was noted to emerge visibly from the 10x objective lens. To check that the beam was roughly centered, the stage was moved along the z direction to insure that the beam did not move laterally (if the beam did move laterally, then the beam was clearly incident at an angle. Adjustments were made with the kinematic mounts until the x-y position of the beam did not appear to move on the card when the stage was moved up and down in the z-direction). This was iterated until the beam appeared to be visually centered on the 100x objective. As a final check, a power meter was placed immediately after objective, small adjustments were made until the reading was maximized.

2.6.3 Knife Edge Measurement Method

Once the beam was successfully coupled to the back aperture, it became necessary to characterize the spot size. This can be estimated based on the wavelength of the beam and the NA of the objective, this is called the diffraction limit. The ideal resolution limit of collimated light through a microscope objective is given by $d = \frac{\lambda}{NA}$ where λ is the wavelength of light, NA is the numerical aperture of the objective, and d is the diameter of the spot size, which we take to be the cross section of a Gaussian beam, having an approximately circular center with intensity decreasing as you move out radially from the center. The diffraction limit gives the lower bound for an ideal spot, it assumes that the Gaussian waist completely fills the back aperture of the objective, but can also be an under-estimate due to imperfections in the alignment, the optical components, index

mismatch, or other experimental factors. We expect the actual spot size to be larger than the predicted spot size, so, for our experimental set up, a knife edge measurement gives most accurate picture of beam size.

The procedure for knife edge measurement is as follows:

- a blade is placed in between the objective and a power meter
- the blade gradually obscures more of the power meter through mechanical increments
- the power is recorded as a function of position of the blade and fit to an error function (the integral of a Gaussian, due to the Gaussian nature of the beam)
- a series of these measurements are taken up and down the z-direction, which fits to a hyperbola. The minimum of the hyperbola taken to be is the beam waist at the focus.

To relate the bright spot that we see post objective from the laser, we can characterize the measured diameter of the spot using metrics such as $1/e$ or $1/e^2$ for a Gaussian distribution.

2.7 Photothermal Experiment Protocol

2.7.1 Laser Experiment Initialization

- The laser was powered on according to manufacturers instructions.
- The laser alignment was quickly checked, and minor adjustments were made if need be for best alignment in the 100x objective.
- The laser power from 100x objective was measured and recorded immediately prior

to each experiment

- The laser was physically blocked by an interlock shutter based system coupled to the door of the optics room while the biological samples were obtained.
- Immediately after being removed from the incubation, cells within the grid were photographed using a 20x objective in the standard cell culture room. These photographs were used to estimate an initial population of cells, though there was no differentiation between live-dead cells.

2.7.2 Cell Irradiation Measurement

- Cells that had been previously seeded onto grided coverslips were removed from an incubator, and a stopwatch was started to prevent cells to remain out of the incubator longer than 25 minutes.
- Control cells were handled in the identical fashion to laser-experiment treated cells, including loading into the experimental set-up and viewing them optically, but no laser irradiation was incident on them.
- Non-control cells were loaded into the microscope set up and a portion of the grid was selected to be the candidate for irradiation.
- The microscope was switched to the 100x objective.
- The laser shutter was opened and a hand-timer was used to maintain laser irradiation over individual cells for the desired experiment time
- Cells were removed from the experimental set up, coverslip removed and discarded, and cells were placed in a new plate with fresh media and allowed to settle for a set period of time. Periods of 6, 12 and 24 hours were investigated during assay development, and twelve hours was set on as the desired viewing time to allow for

cells to settle while balancing out drift of cells in media and across the device.

- Cells were stained using live/dead fluorescent kit, and response was recorded from images of different fluorescent channels on EVOS life sciences microscope

Chapter 3

Radiation Induced DNA Damage

3.1 Defining the DNA Model

While the general model and potential behavior discussed here can be applied to a class of molecules, this section focuses in particular on double-stranded DNA. A basic introduction to the molecule is as follows:

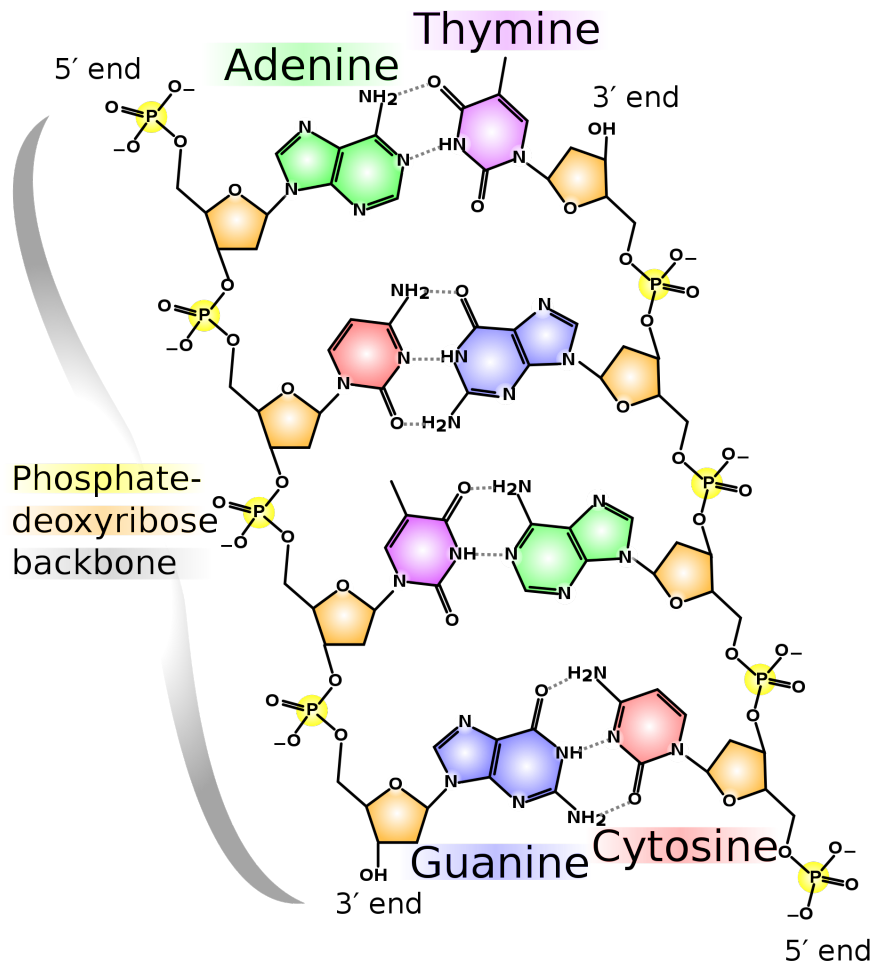


Figure 3.1: *Molecular Structure of the DNA Molecule:* The DNA molecule consists of two charged sugar backbones that are stabilized by covalent bonds. Dangling from this backbone are base pairs that make up the rungs of the DNA ladder structure. The base pairs are molecules consisting of either adenine (A), which pairs with thymine (T) via hydrogen bonds or guanine (G), which pairs with Cytosine (C) via hydrogen bonds. When the molecule is hydrated, the bonds between along with base-pairs that are connected by hydrogen bonds are stabilized by an intra-base pair stacking that forms a pi-bond, and this stack forms the DNA double helix shape.

[29]

To damage DNA, thermal radiation or chemical denaturation can break the hydrogen bonds between base pairs, fling the rungs of the DNA ladder open in a process known as DNA unzipping. This DNA unzipping, or melting, can be reversible. In addition to unzipping, DNA can be damaged irreversibly through damage to the structure of the backbone. The photon energy in the range of ionizing radiation is sufficient to damage this backbone. Non ionizing radiation requires pumping of the system resonances after an accumulation of incident photons in order to break the molecule. Long term damage DNA damage occurs when the effort to repair ruptured bonds is unsuccessful [30].

At sufficient field intensity, non-ionizing radiation can cause dissociation through non-linear effects with micro-geometrical resolution. Non ionizing radiation can produce bio-molecule dissociation through reactive ion species by encouraging a chain chemical reaction that releases (ROS) or reactive nitrogen species (RNS) [10]. For this study, we specifically focus on the THz range of non-ionizing radiation. A definition of THz radiation is as follows: The range from 1-10 THz corresponds to wavelengths of $30\mu\text{m}$ - 3 mm. The scale of this wavelength is generally larger than many biomolecules in question, as is the case for this study. The photon energy in this range varies from 0.04-0.004 eV, lower than the ionizing energy of molecules, but on the same order of the hydrogen bonds and Van-der-Waals molecular interactions. Water is highly absorbing in this range, and spectral sensitivity is exhibited by molecular crystals, something that will be taken advantage of here [17]. In opaque and finely dispersed media, nanoporous and microporous systems, as well as biological tissues, THz radiation exhibits Rayleigh scattering, as opposed to Mie scatterings, which means that the radiation interactions in this media can be described in terms of effective medium theory as a dielectric response [17]. This is utilized for the construction of the DNA model.

3.2 Equation of Motion for DNA Model

The physical model of DNA employed here is called the Peyrard-Bishop-Dauxois (PBD) model. This is a family of phenomenological models that have been refined over time in conjunction with experimental data. The version of the model that we select is the Tapia-Rojo model [31]. The PBD model is a physical model which represents n DNA base-pairs arranged in a ladder like geometry. The model is parameterized by the coordinate y_n , which is the separation between the nucleotide of the n th base pair. The separation is normalized to the equilibrium separation at $T=0$ K in the center of mass frame of the base pair (BP).

The equation of motion for the PBD DNA molecule in this model is Newtons Equations, with a driving term:

$$m\ddot{y}_n = -U'(y_n) - W'(y_n, y_{n+1}) - W'(y_n, y_{n-1}) - m\gamma\dot{y}_n - \eta(t) - F(t) \quad (1)$$

- Dotted superscripts signify partial derivatives in time, and primed terms are partial spatial derivatives by the parameterized coordinate.
- $\eta(t)$ represents the Langevin force term. The definition of this term is a random force drawn from a thermal Gaussian distribution with variance $2m\gamma k_B T$ [31]

The potential term $U'(y_n)$ is defined by the interaction between base pairs is determined by a modified Morse potential :

$$U(y_n) = D_n[e^{-\alpha_n y_n} - 1]^2 + G_n e^{-(y_n - d_n)^2/b_n} \quad (2)$$

This is compared in this study with the classical Morse potential, which is identical to the equation above with the term $G_n = 0$. Morse potentials are utilized to model DNA denaturation, but the potential can be applied to the behavior of bonds within other biomolecules, polymers, and soft matter systems as well [32] [33] [34] [35]. These potentials show different behavior for large stretching of the DNA base pairs, as shown in Figure 3.2. Both the modified and unmodified ($G_n = 0$) Morse potentials are explored in this study, and belong to the same universality class, as will be detailed in later sections.

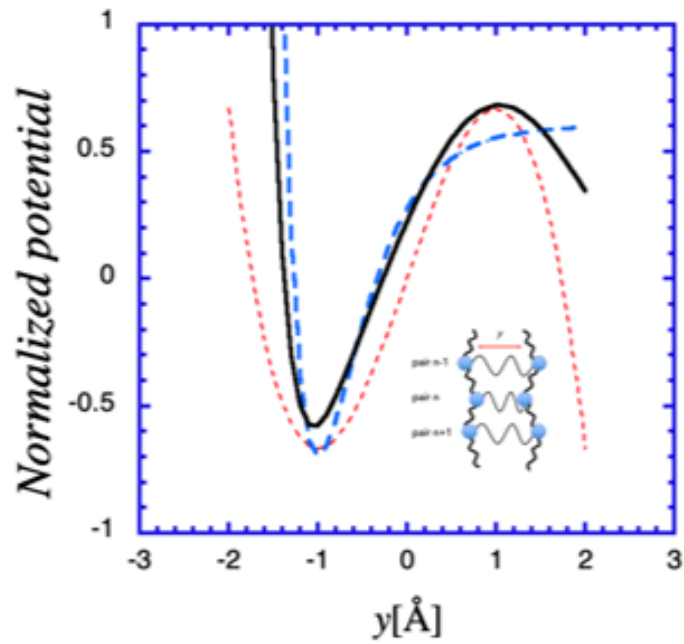


Figure 3.2: *Normalized total equilibrium potentials vs y* : The red dotted line display's the potential of the fold universality class. The modified morse potential is shown in the black solid line, and the unmodified Morse potential is shown in the blue dashed line.

The shape of the morse potential plateaus after a large separation (in the normalized graph this is shown as $y > 1$, but the exact units of the separation are BP dependent), while the modified Morse potential exhibits an exponential drop off. Both potentials, when applied to a harmonic oscillator, are representative of the *fold* universality class [36].

The pi-bonds between separate rungs of the DNA ladder make up the stacking potential. Each pair is stabilized by it's nearest neighbors:

$$W(y_n, y_{n\pm 1}) = \frac{k}{2}[1 + \rho e^{-\delta(y_n + y_{n\pm 1})}(y_n - y_{n\pm 1})^2] \quad (3)$$

The following terms are base-pair specific parameters that are phenomenologically determined from experimental results [31] : D_n, α_n, G_n, d_n and b_n

The model exhibits a well defined minimum of the single dissociation domain boundary, as is indicative of the universality class amplitude-frequency space (AFS) plotted in Figure 3.3. Potentials in this class will show a sharp minimum, which is the basis for positing that molecules described by this model will exhibit spectral differentiation.

3.2.1 Nonlinear Driving Term

To exploit this nonlinear effect, it is important to define the ranges that maintain sufficient field intensity to drive nonlinear effects. Such a possibility is suggested already in the simplest harmonic model of a radiation-driven molecule (or its segment), considered as a mass m oscillating due to the action of a spring (of stiffness k) representing the molecular bond, with y representing the bond length. In this textbook model [37], the dynamics of the oscillatory motion are readily obtained using the standard analysis of a

damped oscillator, driven by force $F(t) = F' \sin(\omega t)$, with frequency ω and time t . The dissociation of the molecule in this case can be defined as a state with amplitude of oscillations \bar{y} exceeding a critical amplitude y_{max} for the molecular breakup (dissociation). The cut-off force-amplitude derivation is sketched in Equations 4a-c.

The Equation of Motion of a damped harmonic oscillator driven by an external electric field is given by [38]:

$$m\ddot{y} + m\gamma\dot{y} + m\omega_0^2 y = -eE \quad (4a)$$

Let $E = E_0 e^{-i\omega t}$ and solve for displacements of the form $y = y_0 e^{i\omega t}$:

$$y = \frac{-eE/m}{(\omega_0^2 - \omega^2) - i\gamma\omega} \quad (4b)$$

Normalize equation 4b and solve the result for y_{max} , the required force amplitude for this to occur is given by:

$$F_0 = \beta \left[\left(\frac{\Delta\omega}{\omega_0} \right)^2 + \left(\frac{\gamma}{\omega_0} \right)^2 \right]^{1/2} \quad (4c)$$

Where:

- $\gamma \ll \omega_0$ damping index
- $\Delta\omega = \omega - \omega_0$
- $|\Delta\omega| \ll \omega_0$ where $\omega_0 = \sqrt{\frac{k}{m}}$
- $\beta = 2y_{max} m \omega_0^2$

This model in amplitude-frequency space has stable and disassociative regimes, as shown

in Figure 3.3.

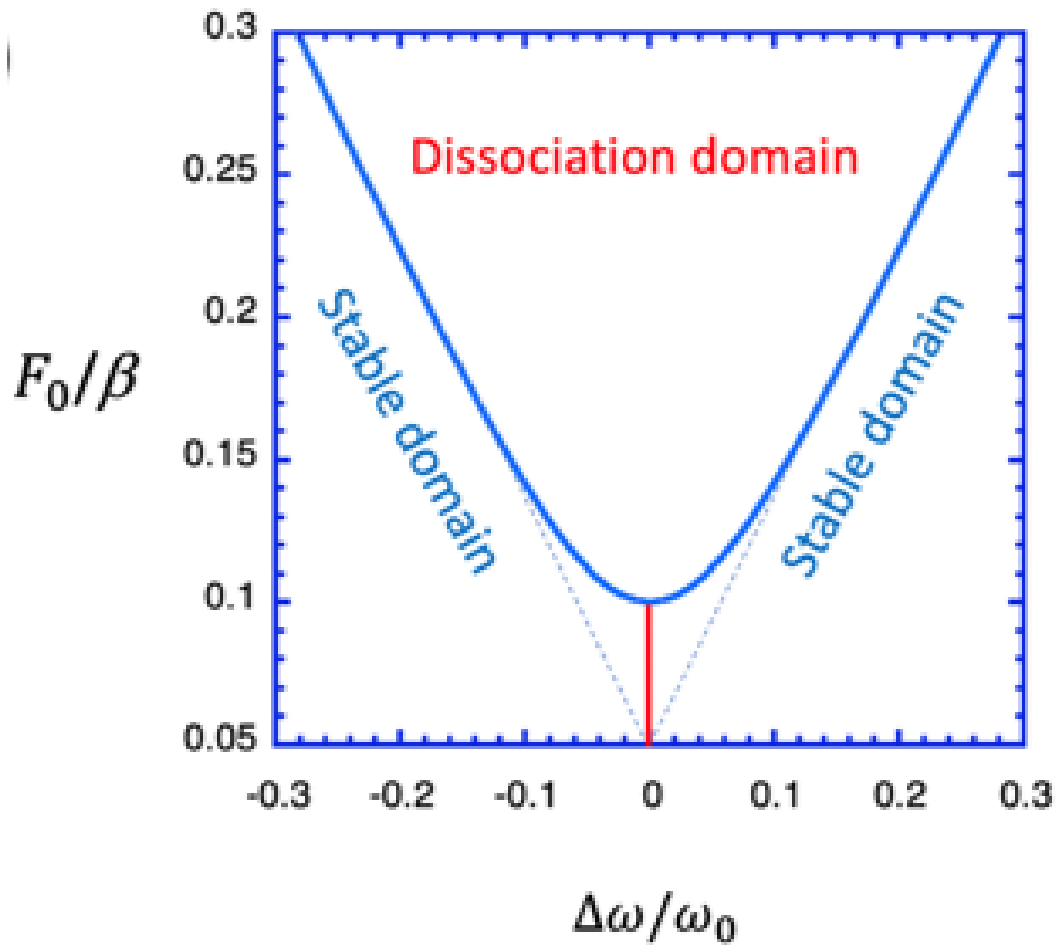


Figure 3.3: *Amplitude-frequency space (AFS) for simple harmonic model SHM: depending on the driving force and resulting response of the system in AFS, the system can transition from stable to an unstable domain*

We assume that there exists some low frequency/amplitude range where the system responds linearly. As the system evolves from linear response, we predict a sharp minimum in amplitude-frequency space and a clear boundary marking dissociation will emerge as a consequence of the universality class. For instance, consider when $\frac{F_0}{\beta} = \frac{\gamma}{\omega_0}$. In the model, this gives $(\frac{\Delta\omega}{\omega_0})^2 = 0$ which is stable except for $\omega = \omega_0$, which marks where the system disassociates. Within the stable domain of amplitude-frequency space, the average separation parameter \bar{y} is maximized at resonance. This corresponds to ω_0 in this simple model for all driving amplitudes. Therefore, we find the trace of maxima in this domain as simply a vertical line at $\omega = \omega_0$ terminating at the bottom of the dissociation domain. We argue that there is a connection between the disassociation dynamics of this model and the behavior of non-linear larger molecules. Understanding the universality of these dissociation conditions connects the behavior of disassociation in the harmonic model with real-world models.

3.2.2 Initializing the Model

The model treats time discretely. We step through time towards a calculation of average base pair separation using a Verlet-type algorithm. The system is first equilibrated at a set temperature (either T=290K or T=1 K) without a driving term $F(t) = 0$. The output is checked against literature, and found to be consistent [39]. Notably, a measured separation of base-pairings, also known in physiological DNA as “bubbles” or “breathing modes,” emerge as the system approaches the melting temperature of T=314 K. It was confirmed against literature that above the physiological DNA melting temperature, we see a full disassociation of the molecule in the model.

3.2.3 Introducing a Driving Force

To simulate the coupling of the molecular bonds to incident electromagnetic radiation, we introduce a sinusoidally varying driving force. The driving force term is applied after the system is initialized, and the response of the system is recorded over time. The results are plotted below in Figure 3.4 as a 3D map of AFS of a system of resultant y_n for a homogeneous AT strand initialized at $T = 1K$ and driven at the displayed frequencies and amplitudes. Two versions of the model are compared in Figure 3.4, that of a system whose base pair separation is modeled by the morse potential, as well as that of a system modeled by the modified morse potential.

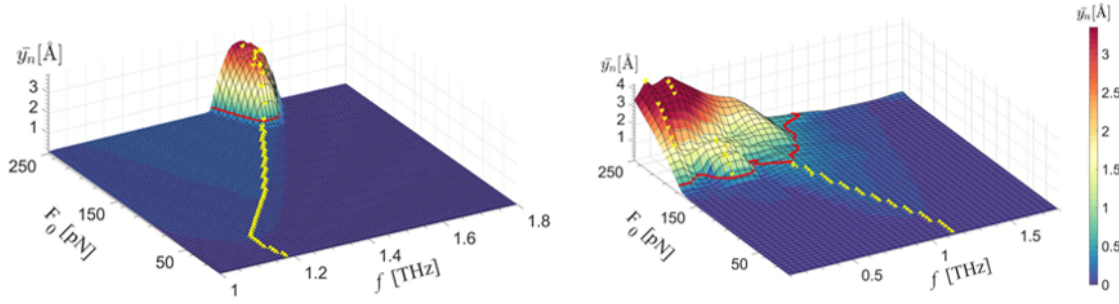


Figure 3.4: *Amplitude-frequency space (AFS) response of molecule to external driving:* This 3D color plot represents the AFS response of the DNA molecule under different Morse potentials. The y axis displays the applied driving force in pN, while the x and z axis map out the AFS response of the system. Frequency is given on the x axis in units of THz, and Amplitude is shown on the z axis in terms of normalized base pair separation. The panel on the left represents the response of poly-AT base pairs at T=1K using the modified Morse potential, while the right hand side represents the same base pair response under the unmodified morse potential.

Regardless of which form the Morse potential takes, the AFS in Figure 3.4 shows a sharp dissociation boundary for a minimum cutoff frequency. The color map is the scale of the average separation of BP in Angstroms. The yellow dots mark the maximum separation for each amplitude, and as predicted, at $T=1K$ these dots form a trace which emerges from the linear resonance ω_0 through the dissociation domain. Once the system has crossed into dissociation, as measured by the system increasing the average BP separation threshold, a red data point is indicated on the graph. These red data points ultimately result in a line that maps out the dissociation domain. Predictably, the modified Morse potential appears to have a superficially similar appearance to the universality class dissociation domain plotted in Figure 3.3, in that the maximum points labeled by red dots form a parabolic domain boundary. The unmodified Morse potential does not exhibit as cleanly parabolic of a domain boundary. The unmodified Morse potential in the range of dissociation plateaus instead of creating a barrier. This plateau is a weaker energy barrier to overcome, meaning base pair breaking is more easily reversed. When this is aggregated across the system, it results in the average separation of the strand broadening and also forming multiple local minimums. This broadening is in fact in good agreement with the chaotic behavior of the model [40]. Just as we can define a frequency-amplitude minimum for the onset of the dissociation regime for the universality class, we find that each potential has a unique frequency minimum: for the modified Morse potential, the trace is blue-shifted until it reaches the simulation-derived minimum $f_{min} = 1.52$ THz, while the modified potential is red-shifted reaching the dissociation onset at $f_{min} = 0.8$ THz.

3.3 Amplitude-Frequency Dissociation of DNA Model

In this section we will discuss the robustness of this model to thermal fluctuations, and explore the evolution of linear resonances from the stable to the unstable regimes.

3.3.1 Temperature Effects on the Trace of the System

We define the trace as the maximal separation of the DNA strand across investigated frequencies for a given amplitude. The trace can be visualized graphically by the point in the linear regime that shows the largest separation, in Figure 3.4 it is labeled as yellow points. Mathematically, the trace is related to the resonant frequency of the system (the frequency of the maximum separation at zero driving). Beginning with the simple harmonic model by taking a Taylor expansion of the system at the bottom of the potential well, the resonant frequency for the previously investigated AT stand can be calculated from $f_{eff} = \frac{\omega_{eff}}{2\pi} = \frac{1}{2\pi} \sqrt{\frac{k}{m}} \approx 1.55$ THz. The simulated minimal value for the trace approaches this at low amplitude driving, as marked in Figure 3.4 as beginning at $f_{min} = 1.52$ THz. The evolution of the trace to the dissociation domain, and the robustness of this trace for all models in this universality class is the key finding of this investigation. Specifically, the behavior of the trace beginning at the resonance of an undriven oscillator (simple harmonic motion) and leading to the dissociation domain, remains unchanged. This is robust even with modifications to the potential.

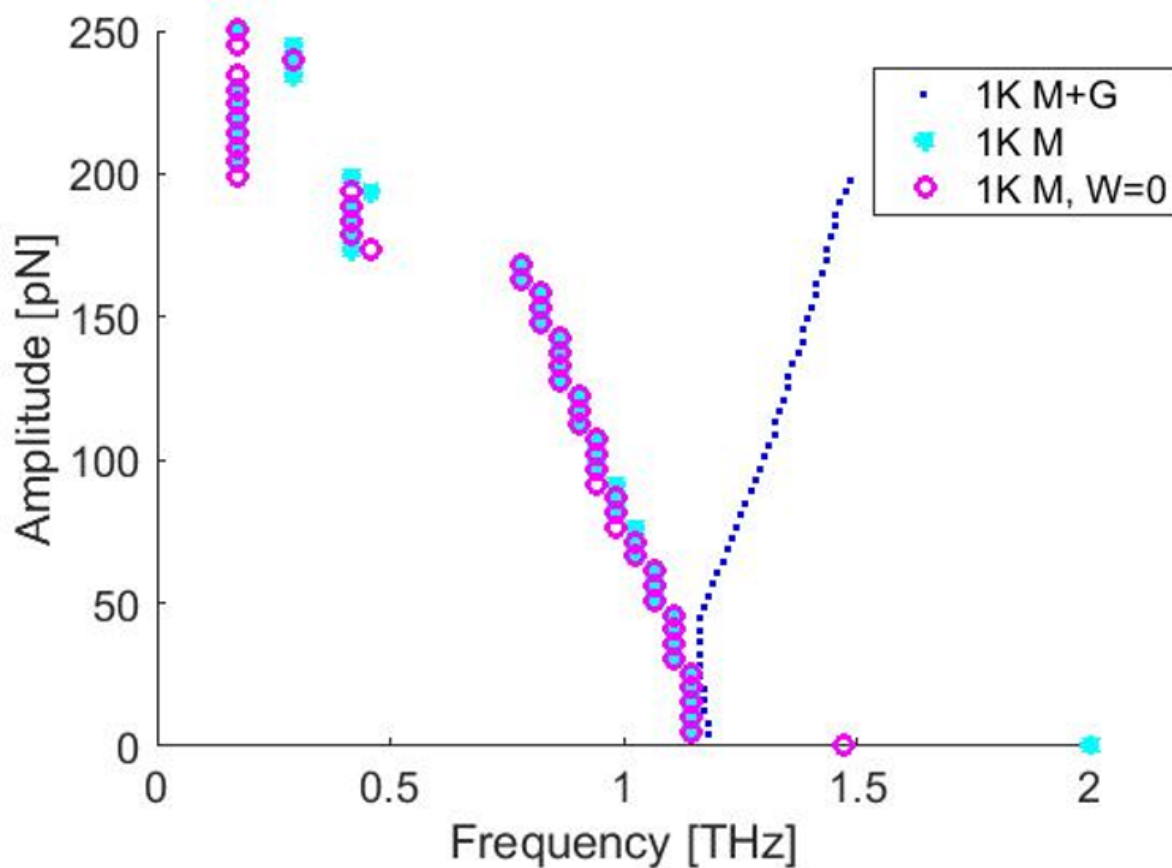


Figure 3.5: *Trace Under Different Potentials*: The trace at different variations on the Morse potential and stacking potential is compared in frequency space for an AT strand at $T=1\text{K}$. The blue squares (M+G) represent the response of the modified morse potential (morse potential + gaussian barrier) at 1K. The light blue circles are the response of the system of the unmodified Morse Potential when the system is thermalized at 1K. The purple hollow circles display the morse potential when the stacking term W is set to zero. The modified and unmodified morse potential closely match for lower regions of frequency-amplitude space.

For regions of low-frequency amplitude space plotted in Figure 3.5, the trace of the unmodified morse potential behaves in an identical manner with or without the stacking potential, and a trace can be determined as expected from the universality class. The long frequency sinusoidal driving force is the key to preserving this universality class. For small amplitude simulations near resonance, the maximum average separation occurs when each base pair moves constructively. Because the scale of incident THz radiation is large compared with the molecule segments that are investigated, the base pair motion is uniformly affected in the stable regime in the absence of thermal effects. In other words $y_1 = y_2 = \dots = y_n$ in this regime. It follows that, under these conditions, because the stacking potential W is directly proportional to $(y_n - y_{n-1})^2$, if each when nearest neighbors have identical separations ($y_n = y_{n+1}$) then $W = 0$ under these conditions.

This was confirmed by simulating the evolution of the system when the stacking potential is removed $W(y_n, y_{n+1}) = 0$, as shown in Figure 3.5. The trace when the molecule is coupled constructively to the incident radiation can be explained by examining the local confining potential of a single base pairing. Locally, the confining potential can be approximated as a parabolic function: $U(y_n) \approx \frac{k}{2}(y_n - \alpha)^2$ which is why the trace behaves harmonically in the range of long wavelength driving terms and lower amplitude oscillations. This potential implies that a given base pair experiences a force: $F_n = -\frac{\partial U(y_n)}{\partial y_n} = ky_n - k\alpha$ which contains the purely harmonic part, and describes the lack of nonlinear effects along this path. This hold for both the modified and unmodified morse potentials. As is shown in Figure 3.2, the various functions that approximate the morse potential mainly effect the behavior of the molecule after a given separation, or breakaway point. Before the breakaway: either there is an additional potential well or a plateau. However, before this breakaway point both the unmodified and modified morse

potentials are governed by parabolic behavior [41] [42] [43]. The term α in the expansion of the potential accounts for the asymmetry of the potential well. This implies that a simple averaging procedure of base pair separation y_n will always produce a non-zero result, except very close to the potential minimum. This is shown throughout the range of the trace, where $\bar{y}_n = \sqrt{\langle y_n^2 \rangle} \approx B \langle y_n \rangle$ where $B > 0$ is a scaling constant. In conclusion, these phenomenologically derived DNA models will exhibit a trace that follows from the harmonic resonance to the dissociation domain.

3.3.2 Model Robustness Under Thermal Fluctuations

We investigate the behavior of the trace and how it is modified by increasing the bath temperature of the system.

Focusing on an AT strand, we replot Figure 3.4 which compared the effect of modified vs unmodified morse potential at $T= 1K$ and include the result of the modified morse potential at a initialization temperature of $T= 290K$.

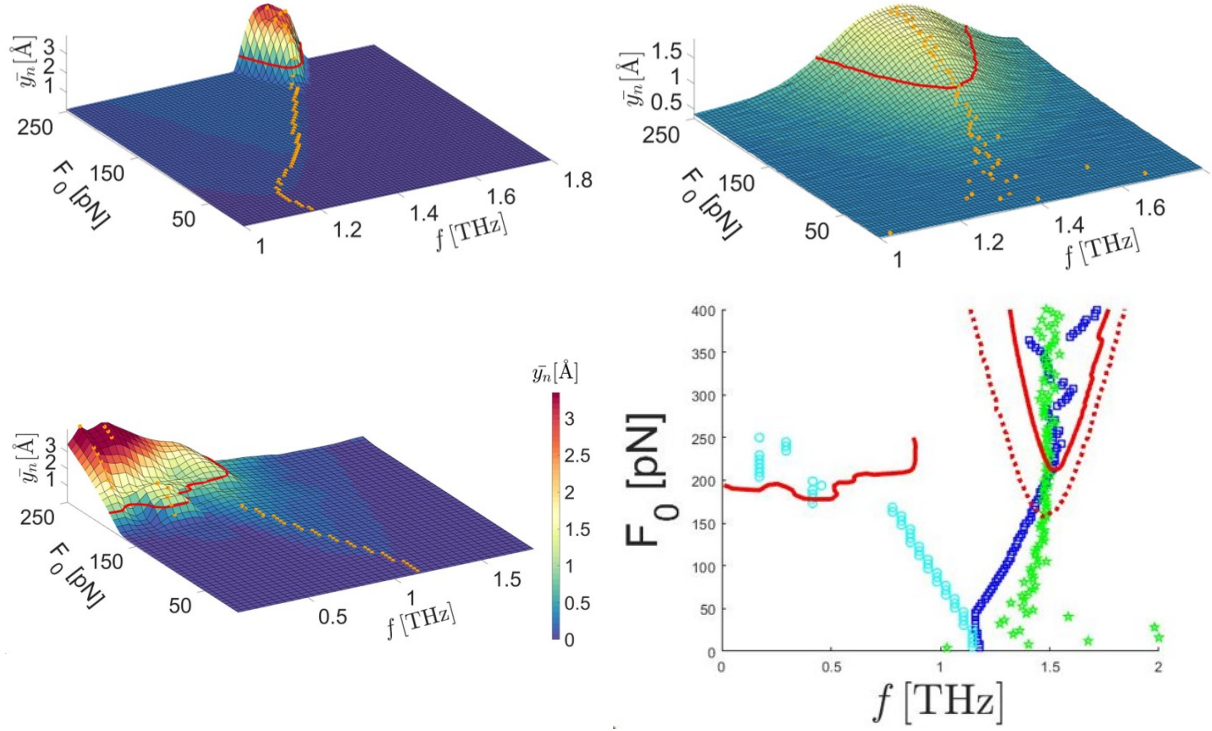


Figure 3.6: *Comparison of Trace for different potentials and temperatures:* Color maps of the DNA dynamics, where the x-axis shows the driving frequency, the y axis the amplitude of the driving force, and the color map showing the response of the system, calculated as an average (color encoded) separation y_n of BPs. Panel a) describes the response of a pure AT strand at 1K, panel b) shows the same strand under the modified morse potential when the system is initialized at T=290K. Panel c) shows the response at T=1K if the un-modified morse potential is used. Orange dots in panels a)-c) indicate the resonance maxima locations accounting for thermal fluctuations. These respective points are overlaid on panel d) to compare the evolution of the trace under the specified temperature and potentials. In panel d) blue hollow circles represent the trace from the unmodified morse potential at T=1K leading to the red line that is the domain boundary for that system. Blue hollow squares show the trace of the modified morse potential at T=1K leading to the solid red line which is an overlay of the domain boundary for that system. Green stars leading to the red dotted line show the trace of the modified morse potential at T=290 K, and the red dotted line shows the domain boundary for that system.

Temperature induces randomness in the system, which blurs the trace. The trace becomes more clearly defined at higher amplitudes, overlapping around $A = 200$ pN for this system when comparing the response at $T=1$ K and $T=290$ K. Increasing temperature shifts the dissociation domain onset to lower amplitudes, and the minimum frequency is red shifted as well. The general minimum—which ensures spectral selectivity for a range of amplitudes—is preserved at physiological temperatures.

Temperature induced broadening effects of the trace, displayed in Figure 3.6, also holds for GC strands, as well as mixed strands. A 2D projection of the AFS is compared between AT and GC strands in Figure 3.7. While thermal fluctuations create randomness for the trace at lower frequencies, the dissociation domains remain distinct at higher frequencies, showing that the domain onset is distinct for different types of bonds.

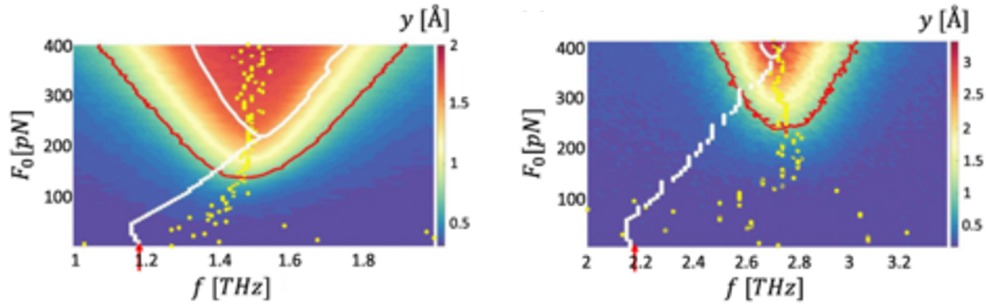


Figure 3.7: *Amplitude-frequency space (AFS) response of AT and GC strands to external driving*: Color maps of the DNA dynamics, where the x-axis shows the driving frequency, the y axis the amplitude of the driving force, and the color map showing the response of the system, calculated as an average (color encoded) separation y_n of BPs. The left graph, figure a) describes the response of a pure AT strand and the right b) describes a pure GT strand. The red arrows along the x-axis point to the linear resonance frequencies of the system $f_0 = 1.26$ THz for AT and $f_0 = 2.21$ THz for GC base pairings. The red line in each figure represents the corresponding boundary dissociation curve. Yellow dots indicate the resonance maxima locations accounting for thermal fluctuations, when the system is thermalized at $T=290$ K, while white dots represent the trace of the resonance maxima locations at $T=1$ K.

In Figure 3.7, we can compare the behavior of the trace at $T=1\text{K}$ (white/light dots) versus $T=290\text{ K}$ (yellow/darker dots). The yellow dots no longer form a clear trace due to the randomness introduced from thermal fluctuations, while at lower temperatures the white dots are not subject to scattering. The yellow dots lead us to the red dissociation domain minimum, because this boundary was calculated at $T=290\text{ K}$. The white dots and white line are superimposed over this graph to compare the behavior of the trace, and the white domain separation when the system is at $T = 1\text{K}$ is overlaid on this diagram. In both cases, the trace connects us to the dissociation domain minimum, though thermal fluctuations do induce some randomness. The domains of dissociation are driven by a range of distinct frequencies, ensuring spectral selectivity between AT and GC strands, and this holds up through the investigated amplitudes. Eventually, if amplitude-frequency space is increased, the domains will continue to broaden, and spectral selectivity will not be maintained.

Comparing the trace at 1K vs 290K in Figure 3.7 and Figure 3.6, it becomes clear that low temperatures are necessary to clearly demarcate a path from linear resonance to dissociation. In other words, the trace can be clearly observed at low temperatures when the randomness due to thermal effects is negligible. We plot the maximum separation of each curve along with the trace in the low frequency, linear regime.

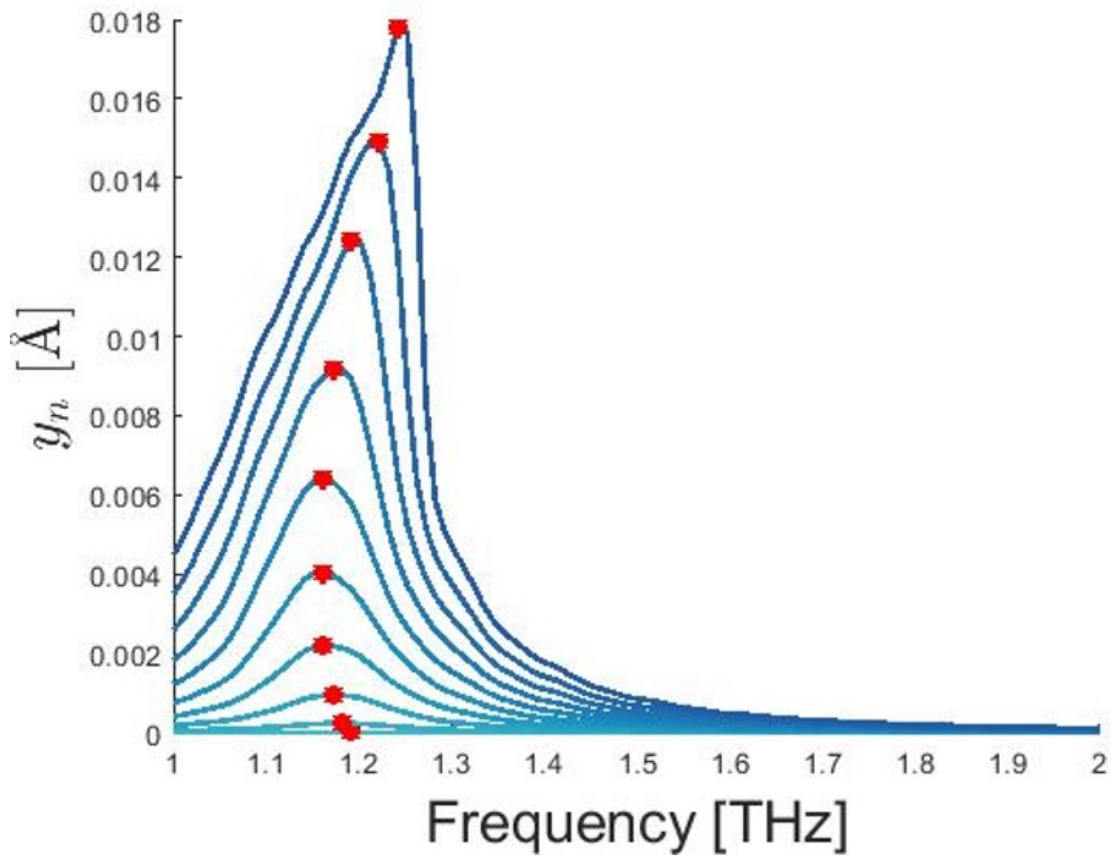


Figure 3.8: *Plot of Average Separation vs Frequency for low temperature, low frequency regime:* We study the average separation of base pairs as a function of frequency for an AT strand thermalized at 1K. Each curve in blue is calculated by driving the system at increasing amplitude. The trace, calculated from the maximum separation for a given curve, is marked by the red dots.

When thermal effects are reduced, the evolution of the trace in the linear regime apparent. This is clear in Figure 3.8 by the evolution from linear resonance as the driving amplitude increases. We compare the evolution of this trace to the resonance at higher amplitudes. In Figure 3.9 the response for increasing driving amplitudes is plotted, while Figure 3.8 is included as an insert, without red dots to guide the eye marking the trace evolution.

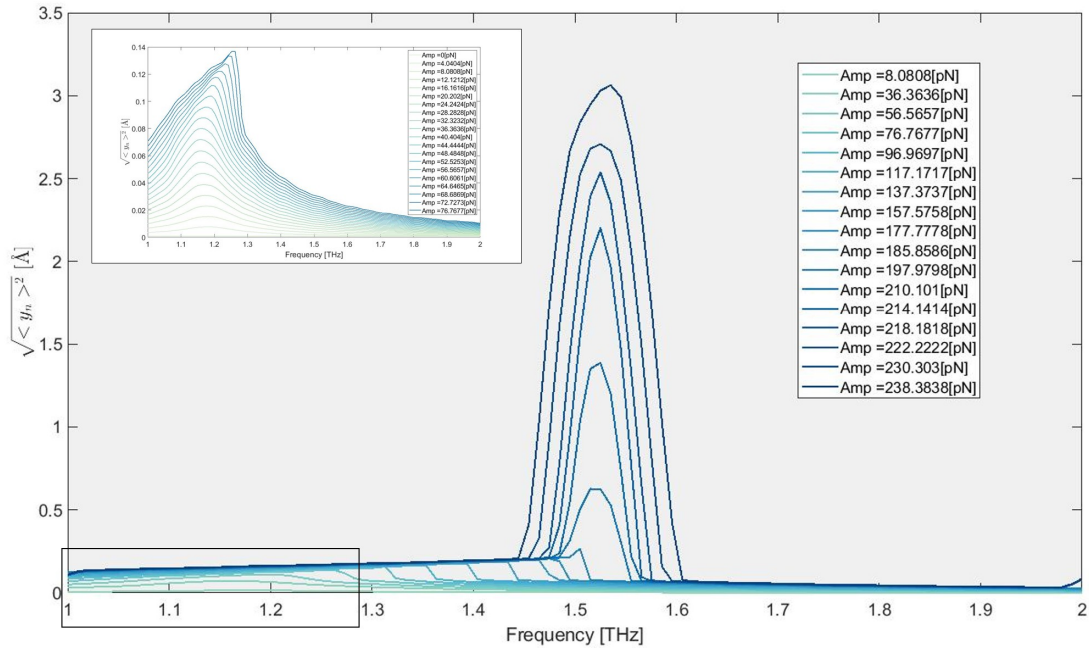


Figure 3.9: *Plot of Average Separation vs Frequency for low temperature, low to high amplitude regime:* Shown here is the average separation of base pairs as a function of frequency for an AT strand thermalized at 1K. Each curve in blue is calculated by driving the system at increasing amplitude, and amplitudes are specified in the key. The low amplitude oscillations evolve into higher amplitude oscillations that signify the dissociation domain

It is clear from Figure 3.8 and Figure 3.9 that a clear path exists from the linear to non-linear regimes, as predicted by models described by this universality class.

3.4 Selectivity of Dissociation Domains

The behavior of these dissociation domains having spectral sensitivity and a sharp minimum that is robust even in the presence of thermal fluctuations, as shown in Figure 3.7 could allow for selective dissociation of specific segments of DNA. For example, if we model a strand of DNA that is primarily GC, but contains one AT base pair, driving the system at $F_0 = 150$ pN and $f = \frac{\omega}{2\pi} = 1.45$ THz dissociates only the AT BP, leaving the GC BP unaffected. Conversely, driving a primarily AT strand containing one GC BP at $F_0 = 400$ pN and $f = \frac{\omega}{2\pi} = 1.5$ THz.

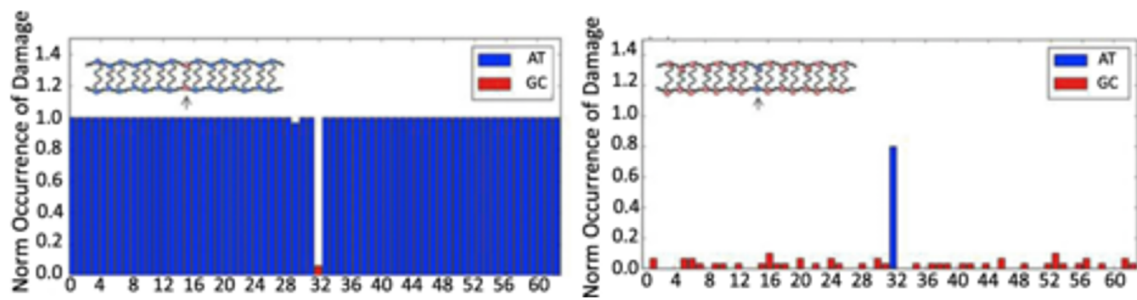


Figure 3.10: *Histograms of the normalized incidents of damage:* In over 30 independent trials a model system was run as shown in the DNA cartoon insert above. Red open circles represent GC base pairings while blue closed circles represent AT base pairings. They are numbered according to their position along the strand. For the left hand histogram, at position 32 of an otherwise AT strand, a GC pair was inserted. On the righthand histogram, at position 32, in an otherwise GC strand, an AT pair was inserted.

This is documented in Figure 3.10, where a histogram represents the incidents of damage when the system is driven within the AFS of the AT dissociation domain. The AT bonds are selectively damaged, while the GC strands are undamaged, regardless of whether the AT is inserted in a GC system or if a GC is inserted in an AT system. The result applies for other configurations of AT and GC strands.

3.5 Discussion

We have shown that the dynamics of the PBD model of DNA behave within the universality class of the *fold catastrophe*, and within this class display the transition from linear behavior at low amplitudes to dissociation at large amplitudes, with a trace that connects these regimes. By focusing on universality of the transition from the linear behavior at low amplitudes, to dissociation at sufficiently large amplitudes we show that for the wide range of models which encompass this class—from simple harmonic oscillator (PBD) type models of DNA—the amplitude-frequency space of the driving force has the same topology: dissociation domains with local, dissociation domain boundary minima. By following the progression of a linear resonance maximum, while increasing gradually intensity of the radiation, the system must necessarily arrive at one of these minima. In other words, we demonstrate that there is necessarily a point where high spectral selectivity is retained. This implies that for such molecules, including DNA, a high spectral sensitivity near the onset of the denaturation processes can be expected in this regime. The universality of the basic topological structure of the AFS domains implies high spectral and dynamical resolution of the large amplitude dynamics of the structures, including dissociation, potential applications of which are discussed in the concluding chapter.

Chapter 4

Biocompatible Melanin

Nanoparticles for Photothermal

Therapies

4.1 Melanin Nanoparticle Photothermal Therapy

This chapter focuses on applications of synthetic melanin nanoparticles to photothermal therapy, and studies the impact of these nanoparticles in *in vitro* tumor cell lines.

Photothermal efficacy in this experimental system is demonstrated.

4.2 Overview of Nanoparticles in Medicine Toward Photodynamic Therapies

4.2.1 Brief Overview of Nanomaterials

Nanomaterials have increasing and widespread use in medicine toward fields such as *in vivo* diagnosis, multi-modal imaging, chemotherapy, phototherapy, gene therapy and immunotherapy, theranostics [44]. Targeted nanomedicine can enhance therapeutic uses of radiation therapies by increasing penetration, specificity, drug uptake and release [5] [4]. Nanomaterials come in many forms, including organic and polymer based materials, inorganic metals, and combinations of the two [45]. Nanoparticles are a subset of nanomaterials, classified as such if their 50% or more of the constituent particles have one or more external dimensions within 1-100 nm; alternatively, if the ratio of surface area to volume exceeds $60m^2/cm^3$ [46]. The external nano-scale dimensions lead to distinct physical, electronic, optical, and magnetic properties than bulk materials [47]. Here, surface properties play a prominent role compared with bulk materials, including surface atoms and surface energy, which results in generally reduced lattice constants and lower melting points [47].

The size of the nanoparticle can be defined by the physical dimensions based on atomic structure, the effective size of a particle within a matrix—based on diffusion or sedimentation behavior—including adsorption on the nanoparticle surface, or the effective size based on mass or electronic distribution [47]. The shape of a nanoparticle can be determined by high resolution microscopy techniques, such as scanning electron microscopy (SEM), transmission electron microscopy (TEM), and scanning probe methods such as Atomic Force Microscopy (AFM) [47].

Nanoparticles can be functionalized, a process where the particle is coated with a specific antibody, protein, sugar, or other biological substance, which leads to selective delivery of drugs to target without damaging other tissues [44]. Targeted nanoparticles can be particularly advantageous for converting otherwise biologically inert non-ionizing radiation to heat as a subset of photo-dynamic therapy [48] [49] [50].

4.2.2 Brief Overview of Photodynamic Therapy

Photodynamic therapy towards cancer an alternative tumor-ablative and function-sparing intervention. It involves three components: 1) A nanoparticle which acts as a target-specific photosensitizer (PS) followed by 2) local illumination of the target with light of a specific wavelength to activate the PS and 3) energy transfer from the excited PS to the system. This energy transfer can be in the form of localized heat, drug release, or formation of chemical reactions such as reactive oxygen species (ROS) [51] [50]. When the energy transfer is specifically aimed at converting light to heat, the process is referred to as photothermal therapy, which is a subset of photodynamic therapy.

Within the landscape of existing nanoparticles used for photodynamic cancer therapies, some examples include:

- Organic materials such as porphyrinoid compounds comprising of porphyrin or porphyrin-based macrocyclic structures, as well as nonporphyrinoid compounds like anthraquinones, phenothiazines, xanthenes, cyanines, and curcuminoids which act as ROS inducing 2nd generation photosensitizers [51]
- Inorganic materials such as doped nanoparticles ($\text{LaF}_3:\text{Ce}^{3+}$, $\text{LuF}_3:\text{Ce}^{3+}$, $\text{CaF}_2:\text{Mn}^{2+}$, $\text{CaF}_2:\text{Eu}^{2+}$, $\text{BaFBr}:\text{Eu}^{2+}$, $\text{BaFBr}:\text{Mn}^{2+}$, and $\text{CaPO}_4:\text{Mn}^{2+}$) and semiconductor nanoparticles (CdS , ZnO , ZnS , and TiO_2) for X-ray mediation [52].

- Gold nanoparticles, known for biocompatibility, efficient photothermal conversion, as well as drug loading [53] [54] [55].
- Carbon-based particles for ROS and photothermal applications, including (but not limited to) carbon nanotubes [56], graphene-based materials including graphene quantum dots (GQDs), and carbon dots (CDs) [57].
- Melanin and melanin-derived nanoparticles, which will be the focus of this chapter [45] [7] [58]

PDT synthesizes components (light, inert nanoparticles) that alone not have toxic effects on the body. When nanoparticles are sensitized to deliver a therapy upon activation by non-ionizing radiation, selected cells that are sensitized with nanoparticles may be destroyed by the chain reaction resulting from the nanoparticle and non-ionizing radiation, while unsensitized cells—that is, cells that do not contain nanoparticles—are left undamaged [51]. PDT is therefore unlike chemotherapy drugs that induce systemic toxicity, or ionizing light of radiation therapy that damages normal tissues [51].

In the case of radiation that is only weakly absorbed by biological cells, nanoparticles that absorb in the selected range will amplify existing absorption capacity. For non ionizing radiation the signal may not be damaging on it's own, but can cause cell death when paired with nanoparticles due to efficient conversion of signal to thermal radiation, as this chapter will focus on.

4.3 Motivation: The Melanin Chromophore as a Photothermal Sensitizer

Cutaneous melanoma is an aggressive cancer because of its propensity for quick metastasis, causing widespread disease progression and leading to approximately 60,000 deaths each year worldwide [59]. Limited progress has been toward melanoma therapies, with recent focus on genetic mutations which accounts for only 50% of noted melanoma subtypes [59].

Melanoma develops in melanocytes, which are cells in the skin that produce melanin. Melanin production in cancerous melanocytes becomes highly dysregulated, either due to, or in concert with genetic mutations [59]. Unlike their healthy counterparts, melanoma cells do not excrete melanin; instead they remain heavily pigmented compared with normal cells [60]. As a result of both dysregulated melanin production and melanin excretion processes, cutaneous melanoma tumors are more heavily pigmented than normal cells [61].

The natural buildup of this pigment within the cell creates novel avenues for selective medical targeting of melanoma cells, such as the detection of melanoma circulating tumor cells (CTCs). Circulating tumor cells are a hallmark of metastatic cancer. CTCs are defined as cancerous cells that break off from the existing tumor and travel throughout the bloodstream where they either are removed, or nucleate additional cancer sites throughout the body. CTCs are usually challenging to identify in the blood stream due to their small volume relative to other blood components. For melanoma CTCs in particular, the abnormal buildup of melanin granules in melanoma CTCs aids in the detection when used as a contrast agent [62]. As a chromophore, melanin has a distinct absorption from prominent blood components, as shown in Figure 4.1.

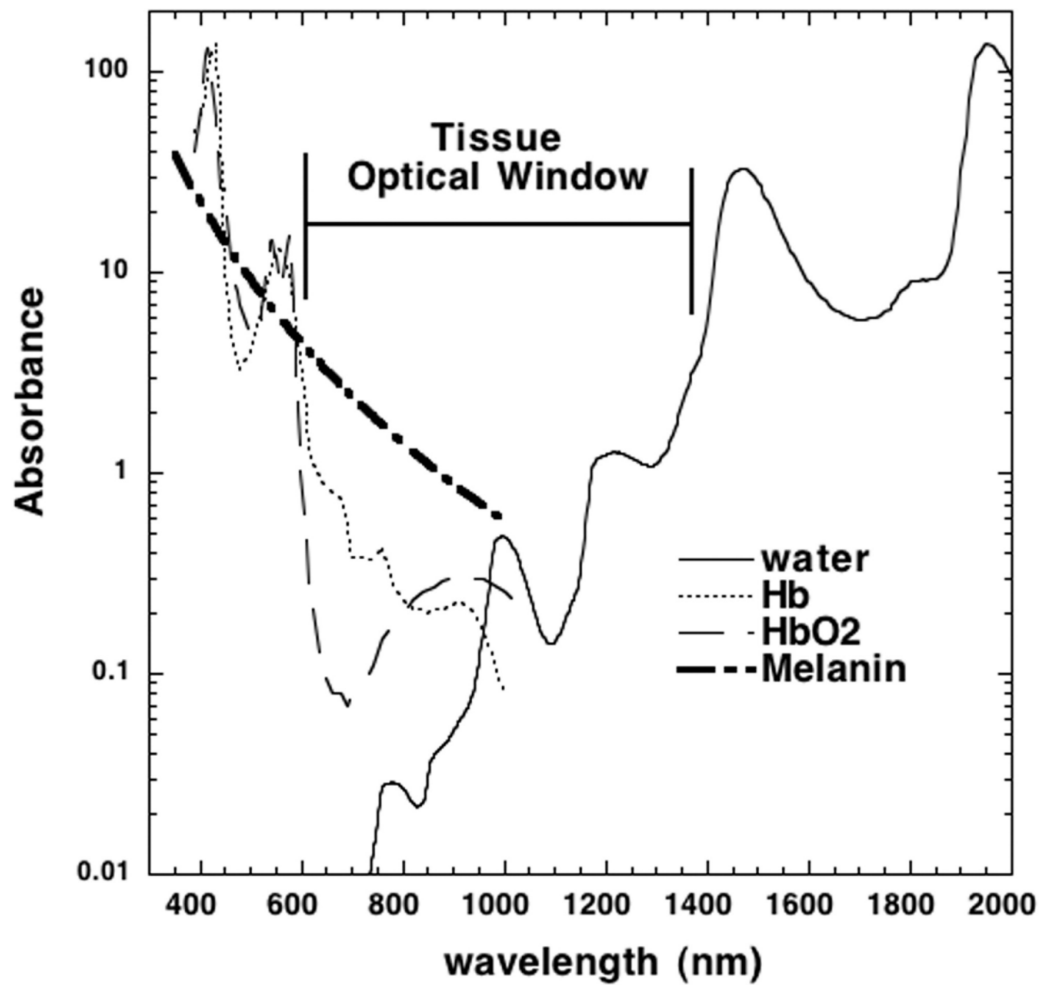


Figure 4.1: *Absorption Spectra of Hemoglobin (Hb), oxyhemoglobin (HbO₂), Melanin (unspecified) compared with water:* The optical absorption spectra of these chromophores are featured because they are prominent naturally occurring chromophores in human tissue.

[63]

Additionally, melanin nanoparticles are characterized by their broad spectrum absorption, and their ability to efficiently convert light to heat [64] [58] [45] [65]. Due to the properties of melanin as a biocompatible photothermal material, melanoma tumors and CTCs are excellent candidates for photothermal therapies [45] [65] [66].

4.4 Material Characterization of Melanin

4.5 Melanin as a Biocompatible Selective Photothermal Agent

Human melanin is a biocompatible polymer which is heterogeneous in nature [45]. In humans, melanin is eumelanin and pheomelanin [67]. Both are naturally occurring pigments, and they provide color to organs such as skin, hair, and eyes. Visually, eumelanin appears darker while pheomelanin appears yellow or red, though the spectrum of each can differ. Natural melanin is synthesized derived from a tyrosine precursor, and this process and chemical structure is shown in Figure 4.2. In synthetic melanin, the optical properties can be tuned by controlling the pH of the reaction during synthesis [68].

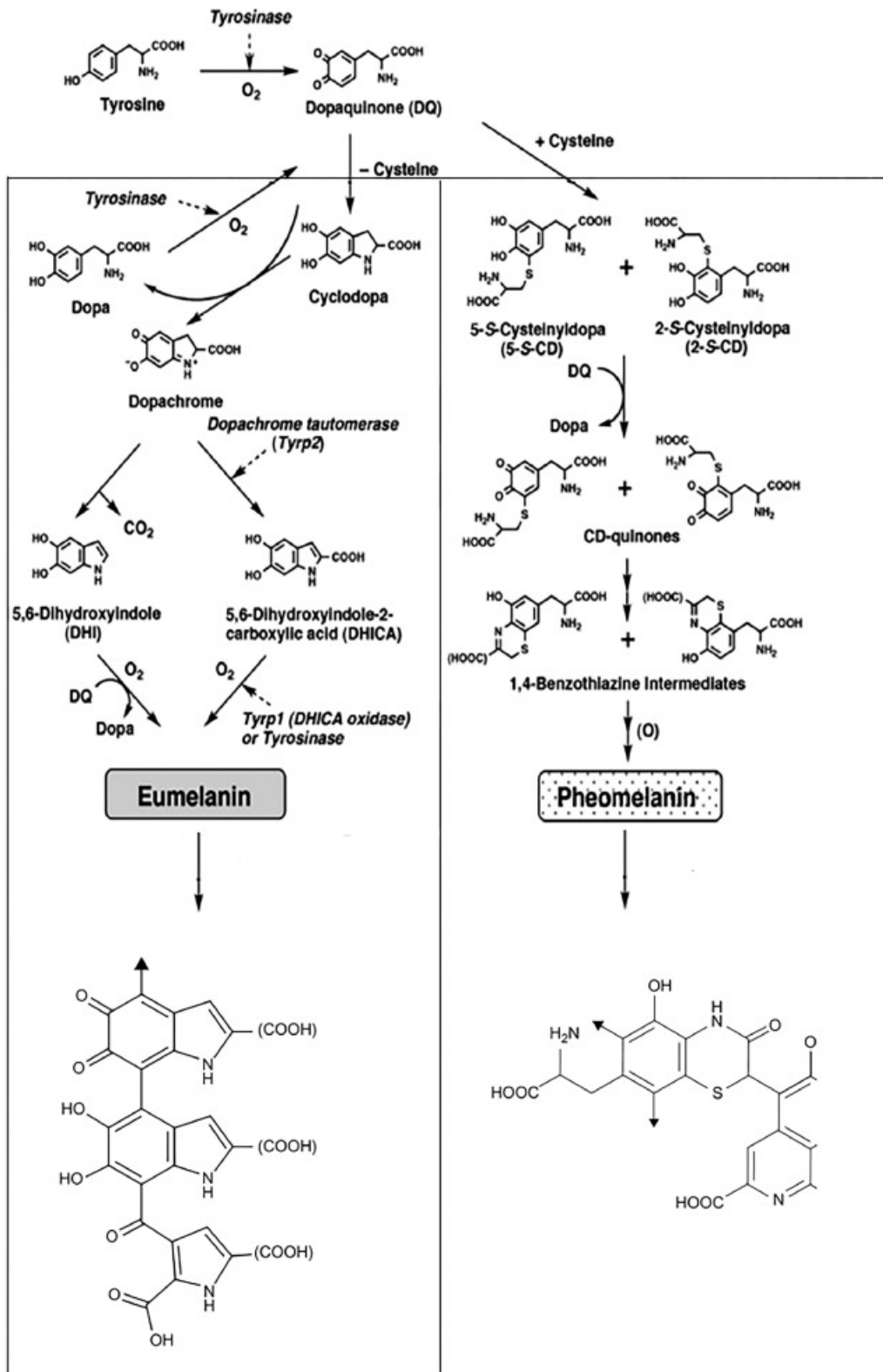


Figure 4.2: *Melanin Synthesis Pathways*: From literature, chemical reactions that synthesize melanin

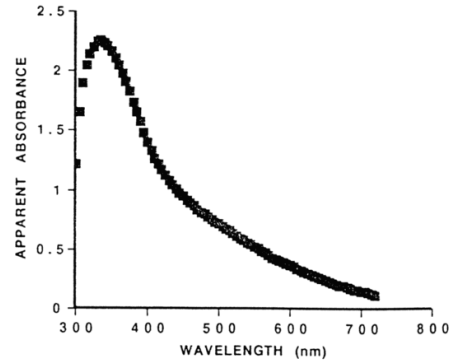
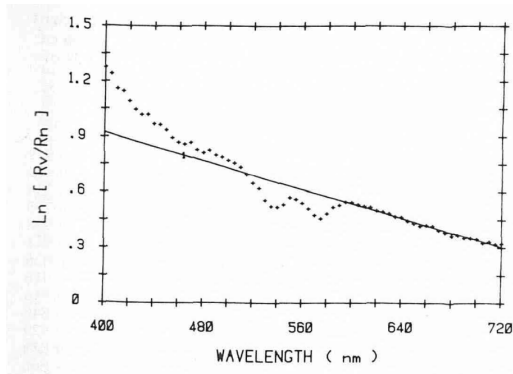
[68]

Both forms of melanin function to contribute to human pigment, and both forms absorb UV radiation, and production of melanin in the skin is adjusted for epidermal homeostasis in different environments. Eumelanin is primarily photo-stable under UV radiation, which is protective to the body, while pheomelanin is photounstable which may contribute to carcinogenesis [67]. The structure showed in Figure 4.2 represents how pheomelanin is distinguished from eumelanin by the presence of a sulfur group [45] [69]. Eumelanin is a heterogeneous macromolecule of 5,6-dihydroxyindole (DHI) and its 2-carboxylated form 5,6-dihydroxyindole-2-carboxylic acid (DHICA) [70]. There are currently many models that point towards the potential secondary structure of eumelanins, but there is not currently a consensus [70] [71]. Instead, there are potential likely secondary structures of the polymer, which have been studied through molecular dynamics simulations [71].

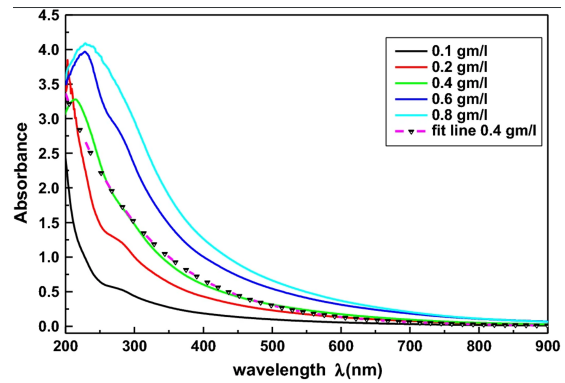
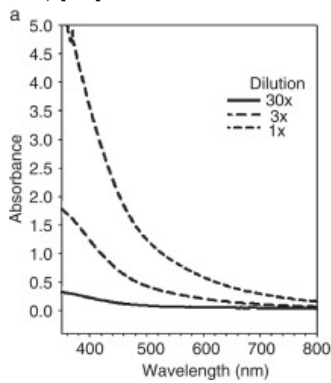
Functionally, it is necessary for the pigment to be broadly absorbing in order for the skin to protect against penetration across natural light radiation, without producing any gaps [71]. While monomers of eumelanin suspensions can absorb physical light, there is normally a frequency dependence of monomer absorption spectrum which is broadened when melanin polymers form their secondary structures [71]. When discussing the secondary structure of the polymer, it is important to note that this is also dependent on environment: Melanin protein structure responds to changes in pH from the external environment due to the presence of carboxylic groups which are repelled in neutral or alkaline solutions, but maintain a network when they are protonated in acidic solutions, and subsequent discussions of dynamics consider melanin polymers in the hydrated states [45]. This pH and hydration sensitivity is utilized for drug camouflaging by melanin, with drug release activated in desired target organs by pH [72]. The nature of melanin's absorption is thought to be produced by disorder in the melanin secondary structure, where melanin-

protomolecules which stack together to form secondary structures of varying sizes with a high degree of rotational disorder and slip along molecular planes within individual secondary structures [71]. These stacked layers are relatively close together, allowing for significant and random excitonic couplings [71]. The majority of photon energy (99%) is dissipated non-radiatively through extremely efficient excited-state vibronic coupling that has been measured on the scale of picoseconds [73]. These are considered to be key ingredients to the spectroscopic features of eumelanin, resulting in melanin's broad absorption, and facilitates melanin's function as a heat sink in skin [74].

The absorbance of melanin has been measured both *in situ* in human skin, as well as dissolved in water, for both synthetic and naturally occurring melanin types. Some highlights of melanin absorbance spectra from various sources in literature are discussed here.



(a) Natural Melanin Absorption (dotted) and a fit to longer wavelength absorption (solid line)[75] (b) Absorption Spectra of Human Melanin Pigmentation [76]



(c) Absorption of synthetic melanin diluted in water[77] (d) Absorption of natural melanin in pH controlled media[78]

Figure 4.3: Absorption spectra of eumelanin pigments, both synthetic and naturally derived: Absorption peaks in the UV, around 350 nm in panel b) to 250 nm or shorter in panel d), and peaks not fully shown in panels a) and c). Spectra that peak in the UV display a broad absorption across the visible spectrum, and the peak intensity and location can be shifted by pH as shown in d).

[75] [76] [77] [78]

We expect our melanin polymers to absorb similarly to the literature shown in Figure 4.3. When dissolved in water at different concentrations, we find that animal-derived Sepia melanin particles display a sharp peak centered in the UV-range that broadly decays, as shown in Figure 4.4.

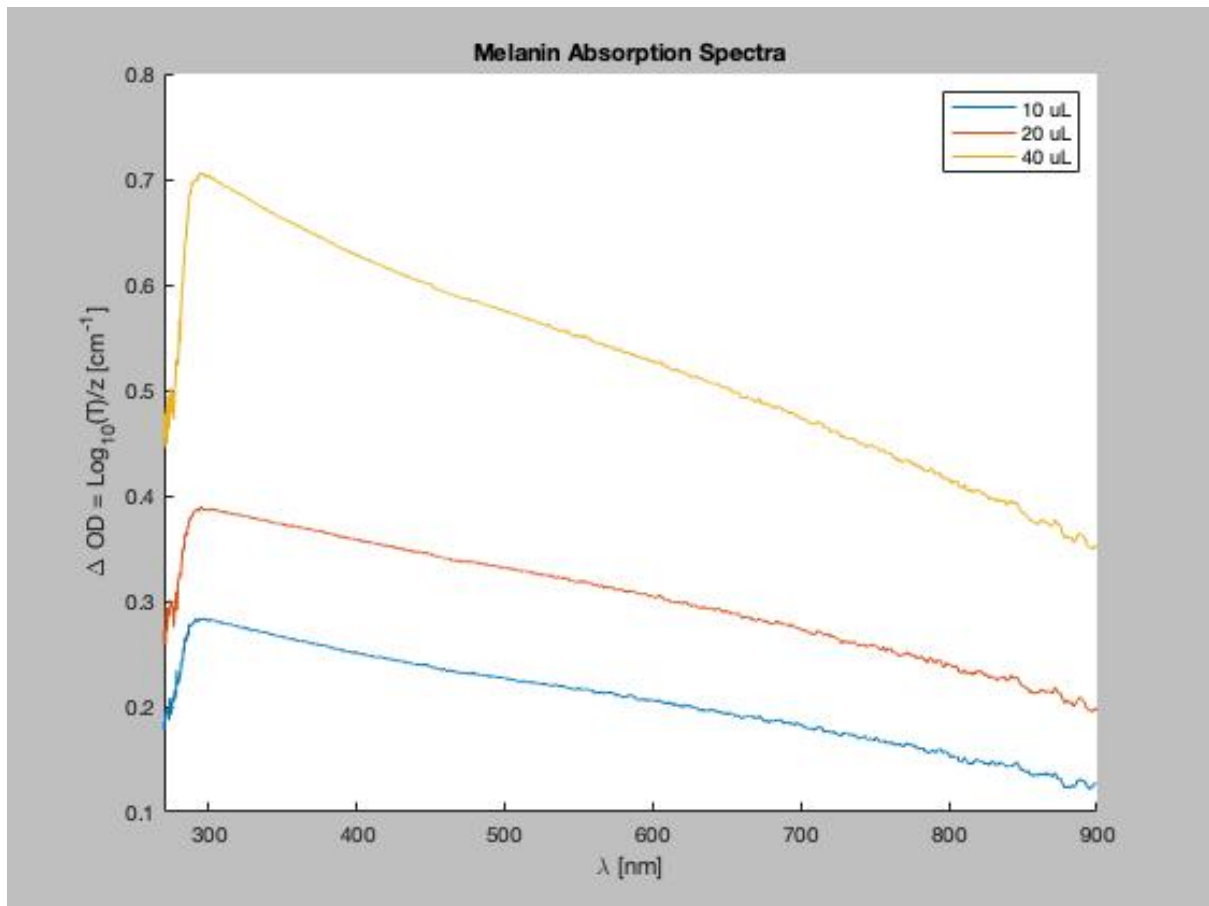


Figure 4.4: *Concentration Dependent Optical Absorbance of Sepia Melanin*: Concentration of melanin dissolved in 1 mL of De-ionized Water. Taken via plastic cuvette using OceanOptics Maya spectrometer, white light source, fiber couple and cuvette accessory.

We see from Figure 4.4 that naturally occurring melanin dissolved in water is consistent with existing data that suggests that melanin is strongly absorbing in UV, but continues to be broadly absorbing approximately 600 nm - 700 nm depending on the concentration.

Melanin granules that are synthesized from poly-dopamine were studied in comparison to the naturally occurring material. Eumelanin synthesized from poly-dopamine is preferred over naturally occurring melanin because it is reliably monodisperse-as shown via SEM images in Figure 4.5 because nanoparticle diameter that is controllable from the pH of the reaction [65].

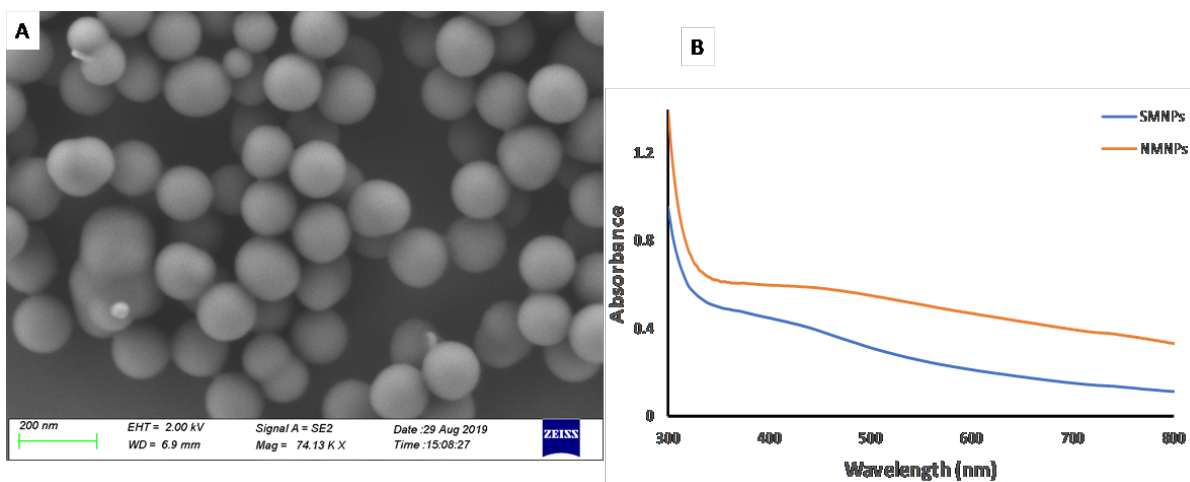


Figure 4.5: *Characterization of Synthesized Melanin Nanoparticles*: Scanning Electron Microscope SEM image of synthesized melanin particles (A) Natural MNPs and (B) Uv-vis of Natural and synthetic MNPs synthesized by collaborator Nwaji Njemuwa

For each curve shown in Figure 4.5, the OD is reduced by 20% between a peak taken to be 290 nm and the measured OD at 530 nm. While the UV absorbance peak does shift depending on the type of melanin-synthetic vs naturally derived-the size of the melanin particle, and the coating, all forms of melanin investigated display the same trend of broad absorbance across the optical and NIR range. For our investigations, 532 nm was chosen as an initial wavelength to irradiate synthetic melanin photosensitizers because it is sufficiently short to take advantage of stronger absorbance of shorter wavelengths by melanin nanoparticles without being ionizing to biological cells.

4.5.1 Governing Equations For Photothermal Study

Photothermal therapy is the process by which light is converted to heat in targeted cells in order to induce apoptosis (cell death) in undesirable objects such as tumors. When applied to cancers, photothermal therapy takes advantage of the relative sensitivity to heat that cancer cells have compared to non-cancerous ones [79] [80]. Cancer cells can be damaged by both acute and prolonged thermal radiation: for example, it has been demonstrated that maintaining cancer cells at 42° C for 15–60 min or above 50° C for 4–6 min is sufficient to kill them [81]. This discussion focuses on how we understand the physical changes brought on by the cell when this light absorption will is converted to heat. For our system, we make the assumption that any material response to laser radiation our system is due to elevated temperatures. We understand these elevated temperatures from the heat equation, which models the evolution of flow of heat inside a material over time and space. The theoretical underpinning of the heat equation comes from conservation of energy and Fourier’s law of heat conduction, but a further derivation is outside the scope of this work.

A photothermal response occurs when the rate of laser-induced electronic excitation is low in comparison to the rate of laser thermalization in a material. In this case, we consider the absorbed energy in the sample as being directly transformed into heat. In the opposite case, when the laser induced excitation rate is high compared with the thermalization rate, excitation can compound and these energy can be sufficient to break chemical bonds in the material. Processes of that nature are known as photo-chemical or photo-catalytic [82]. A photo-physical response is a combination of the above two.

We start by assuming that the primary mechanism for our material is photothermal in the range of wavelengths that we investigate, namely 532 nm and longer. Shorter wavelengths induce a photo-chemical response in melanin, but this is not discussed here. To understand how heat may be transferred to a cell, we start with the generalized equation for heat flow:

$$\rho(\vec{x}, T)c_{\rho}(\vec{x}, T)\frac{\partial T(\vec{x}, T)}{\partial t} - [\kappa(\vec{x}, T) T(\vec{x}, T)] + \rho(\vec{x}, T)c_{\rho}(\vec{x}, T)\vec{v}_s T(\vec{x}, T) = Q(\vec{x}, T) \quad (5)$$

Where: * ρ = density of the sample * c_{ρ} = specific heat at constant pressure * κ = thermal conductivity of the sample * \vec{v}_s = velocity of substrate relative to heat source

If we focus on approximating the heating of one cell due to an aggregate of melanin particles, we assume that the laser beam and sample are stationary for the duration of the radiation. Therefore $\vec{v}_s = 0$ and our equation simplifies to

$$\rho(\vec{x}, T)c_{\rho}(\vec{x}, T)\frac{\partial T(\vec{x}, T)}{\partial t} - [\kappa(\vec{x}, T) T(\vec{x}, T)] = Q(\vec{x}, T) \quad (6)$$

For simplicity, we assume that the thermal conductivity of our cells and our nanoparticles do not change in space or time, giving:

$$\rho(\vec{x}, T)c_\rho(\vec{x}, T)\frac{\partial T(\vec{x}, T)}{\partial t} - \kappa^2 T(\vec{x}, T) = Q(\vec{x}, T) \quad (7)$$

The right-hand side of the equation corresponds to a volumetric heating term $Q(\vec{x}, T)$ as well as the boundary conditions.

In the case of shallow surface absorption of a laser beam, which occurs in our case because, the contribution from the beam can be separated into spatial shape in the planar direction and attenuation term in the normal direction [82]:

$$Q(\vec{x}, T) = g(x, y)f(z)q(t) \quad (8)$$

Where phase changes and chemical heating is ignored, and $q(t)$ refers to a temporal shape. Because we are employing a continuous wave laser, this is taken as a constant.

4.5.1.1 Approximations on the Heat Equation

- Not concerned with the temperature distribution across the particles, we are looking at the exchange of heat between the cell and the medium
- It is assumed that the cell is chocked full of particle aggregates

The first term comes from the volumetric heat exchange of the cell over time

$$\rho(\vec{x}, T)c_\rho(\vec{x}, T)\frac{\partial T(\vec{x}, T)}{\partial t} = \frac{4}{3}\pi r_c^3 m_c c_\rho \frac{\partial T(\vec{x}, T)}{\partial t} \quad (9)$$

Where $r_c =$ the radius of the cell, $m_c =$ the mass of the cell

On the RHS, the heatflow into the cell, taken up by the Absorption $Q(\vec{x}, T)$ is balanced by the diffusion of heat out of the cell, which is mediated by the diffusion constant. Radiation absorbed is mediated by the area of the particles the light is incident on, the number of particles, and the intensity of the light. This assumes that the particles are perfectly absorbing:

$$Q(\vec{x}, T) = IN\pi r_m^2 \quad (10)$$

Finally, there is an exchange of heat between the cell and the surrounding area, this is controlled by the diffusion of heat outside of the cell, as well as the temperature difference radially exiting the cell, and finally the surface area of the cell. Assuming a constant heat capacity, that does not change with space or time:

$$\kappa^2 T(\vec{x}, T) \rightarrow \frac{k_w \Delta T}{r_c} 4\pi r_c^2 \quad (11)$$

Combining terms gives:

$$\frac{4}{3}\pi r_c^3 m_c c_\rho \frac{\partial T(\vec{x}, T)}{\partial t} = IN\pi r_m^2 - \frac{k_w}{r_c} \Delta T 4\pi r_c^2 \quad (12)$$

This simplifies to:

$$\frac{4}{3}r_c m_c c_\rho \frac{\partial T(\vec{x}, T)}{\partial t} = IN \frac{r_m^2}{r_c^2} - 4 \frac{k_w}{r_c} \Delta T \quad (13 \text{ a})$$

Gathering terms of Eq 13a gives:

$$\alpha \frac{\partial \Delta T_c}{\partial t} \approx \mathcal{O} - \beta \Delta T_c \quad (13b)$$

where $\alpha = \frac{4}{3}\rho_w c_w$, $\beta = 4k_w/r_c$ and \mathcal{O} is the radiation power density absorbed in all MNPs. Writing in this way demonstrates the relation between the heat intake, and scale of nanoparticles relative to the cell is dominated by the term $(\frac{r_m}{r_c})^2$, under the assumptions that the mNPs absorb the radiation perfectly and the radius of the laser beam in our experiment is roughly r_c . It follows from this scaling that the order of radiation absorbed \mathcal{O} is directly proportional to the nanoparticle density: $\mathcal{O} = \mathcal{O}_{inc} N(\frac{r_m}{r_c})^2$. The solution to Eq 13b is:

$$\Delta T_c = (\mathcal{O}/\beta)[1 - \exp(-\frac{\beta}{\alpha}t)] \quad (13c)$$

The condition for maximum temperature increase is $\frac{\beta}{\alpha}t \gg 1$, or for $t \gg \frac{\alpha}{\beta} = \frac{r_c^2 \rho_w c_w}{3k_w} = t_c$, such that $\Delta T_{cmax} = \mathcal{O}/\beta = \mathcal{O}r_c/4k_w$. Choosing a value of $N = 1000$, which corresponds to a low MNP load, and a power density as applied in this work, $\mathcal{O}_{inc} \approx 10^9 \text{ Wm}^{-2}$, we estimate $\mathcal{O} \approx 4 \times 10^{10} \text{ Wm}^{-2}$. With $\beta = 0.5 \times 10^6 \text{ WKm}^{-2}$. Equation (13c) gives $\Delta T_{cmax} \approx 1000 \text{ K}$. This is the order of heating that causes rapid boiling of the cell interior, and can lead to the cell lysis observed in our experiment, as discussed later. The time to achieve such a level of heating is of the order of $t_{max} \gg t_c \approx 10^{-4} \text{ s}$. It is important to note that this power density has no effect on the cells not having MNPs and immersed in water, since the penetration length in water at this frequency is very large, $\eta \approx 10\text{m}$. Thus, a negligible fraction of the incoming radiation, of order

$\mathcal{D} \approx \mathcal{D}_{inc} \frac{2r_c}{\eta} \approx \mathcal{D}_{inc} 10^{-6} = 10^3 \text{ Wm}^{-2}$ is absorbed in a cell, in general agreement with experimental results outlined in later sections. It is also in good agreement with laser tweezer experiments [15] in which cells, free of any nanoparticles, were subjected to NIR radiation with power density $\mathcal{D} = 3.8 \times 10^{10} \text{ Wm}^{-2}$ for 15 min. It was shown in that experiment that this much larger power density and dose as compared with our current estimate causes no delay in cell growth or increased mortality. This simple estimate thus well explains the basic physics of our experiments with radiation.

4.6 Melanin Nanoparticle Uptake

4.6.1 Cell Lines and Culture Conditions

To study the photothermal applications of melanin nanoparticles towards individual cells, we investigate a mammalian cancer cell line VM-M3, which was selected for its known highly metastatic potential [83], and VM-NM1 which selected as a non-metastatic control. We hypothesized that non-melanin containing cancerous cells that display macrophage-like behavior would engulf sensitizing particles, even if they do not produce melanin themselves. It had been shown previously that this line of macrophage-like cells engulf micron-sized particles, and this behavior was enhanced when incubated with low glucose, low glutamine media. Sepia melanin (Sigma Aldrich: CAS Number 8049-97-6) was obtained to study if cells would take up the sensitizer particle. Both cell lines were originally derived from VM mouse brain tumors, where in the Seyfried lab they were isolated and passaged for *in vitro* work as previously described [84].

4.6.1.1 VM-M3 and VM-NM1 Cell Lines

Cell lines in this study are from the VM tumor model, which is a model of invasive metastatic cancer in the VM mouse line, developed in the Seyfried lab [83]. The VM-M3 cell line was isolated from an *in vivo* aggressive metastatic cancer that originates from a tumor in the brain of the inbred VM mouse strain. This mouse strain is named according to the rules of the International Committee on Standardized Genetic Nomenclature for Mice, and further information on the history of this strain can be found in ref [85]. The VM murine tumor model is comprised of VM-M3, VM-M2, and VM-NM1. The cell lines VM-M2 and VM-M3 are derived from tumors that were highly invasive and metastasized (M) to multiple organs, while VM-NM1 was isolated from a tumor that does not metastasize (NM). From this murine model model, VM-M3 tumors are one of few cell lines which reliably metastasize to the brain [86].

When cultured *in vitro* they display On the other hand, the VM-NM1 cell line *in vivo* creates a more homogeneous tumor with a clear tumor boundary, and does not propagate to other areas of the brain [87]. When these cell lines were isolated from tumor and passaged *in vitro*, it was demonstrated via fluorescent bead assay that VM-M3 exhibit phagocytosis for micron-sized latex beads, while VM-NM1 cells do not phagocytose cells [83]. This was attributed to macrophage characteristics of the cells, which were studied by genetic expression and *in vitro* behavior of VM-M3 and VM-NM1 were compared against the RAW 264.7 macrophage cell line [87]. In particular, CD68 is a valuable marker which identifies macrophages and monocytes, but does not specify macrophage differentiation [88]. In general, tumor-assisted macrophages will exhibit M2 phenotype, but these markers were not studied here, and are considered instead metastatic cancer cells with macrophage properties [89]. We exploit this macrophage-like behavior for

nanoparticle uptake.

4.6.2 Melanin Nanoparticle Uptake

Initial nanoparticle uptake analysis was performed by adding nanoparticle-containing solution to the standard growth medium, incubating the cell lines, and studying the growth. Both VM-NM1 and VM-M3 cell lines were incubated with three candidate nanoparticles: uncoated melanin nanoparticles (MNP), glucose-coated melanin nanoparticles (MNP@GC), and glutamine-coated nanoparticles (MNP@GA). Biocompatibility of uncoated melanin nanoparticles has been demonstrated by previous studies, but in many cases uptake is low [58] [90], or un-quantified. We hypothesized that by adding coatings that certain tumor cells preferentially metabolize, we could increase nanoparticle uptake efficiency in the cell lines that display macrophage characteristics. This assumes that cells would behave similarly to metastatic melanoma in that they would not release particles after taking them up [61]. We found that VM-M3 cells preferentially took up both glucose-coated, glutamine coated, and uncoated melanin, compared with VM-NM1, which did not take up melanin.

Ultimately, glucose-coated particles were selected in accordance with both experimental finding that uptake efficiency is faster, as well as an initial aim at selectivity due to the Warburg Effect of aerobic glycolysis. Briefly, the Warburg effect demonstrates that unlike healthy tissue, and unlike normally proliferating embryonic tissue, tumor cells are shown to use glycolysis even when oxygen is abundant [91]. The molecular basis for this effect, first discovered over a century ago, is still being investigated today [91]. The widespread propensity for cancer cells to increase glucose consumption in accordance with the Warburg effect is the basis for [^{18}F]fluoro-2-deoxyglucose (FDG) (a radio-opaque

sugar) in Positron Emission Topography (PET) for imaging and evaluation of certain kinds of tumors and cancer progression in the human body [92] .

4.6.2.1 Nanoparticle Cytotoxicity Study

An in-situ fluorescent assay was employed to determine cell viability, as described in Materials and Methods. This is first applied to assess cytotoxicity in the presence of melanin particles in media. The highly absorbing eumelanin used for these studies is established as a biocompatible polymer, but has not yet been studied in this type of cell line [64] [69]. For VM-M3 cell lines preferentially upatake particles coated with sugar, so glucose melanin nanoparticles were utilized [87]. To avoid the over-consumption of melanin-induced apoptosis, a range of concentrations was added to cell media in order to assess long-term viability and biocompatibility. The results are shown in Figure 4.6.

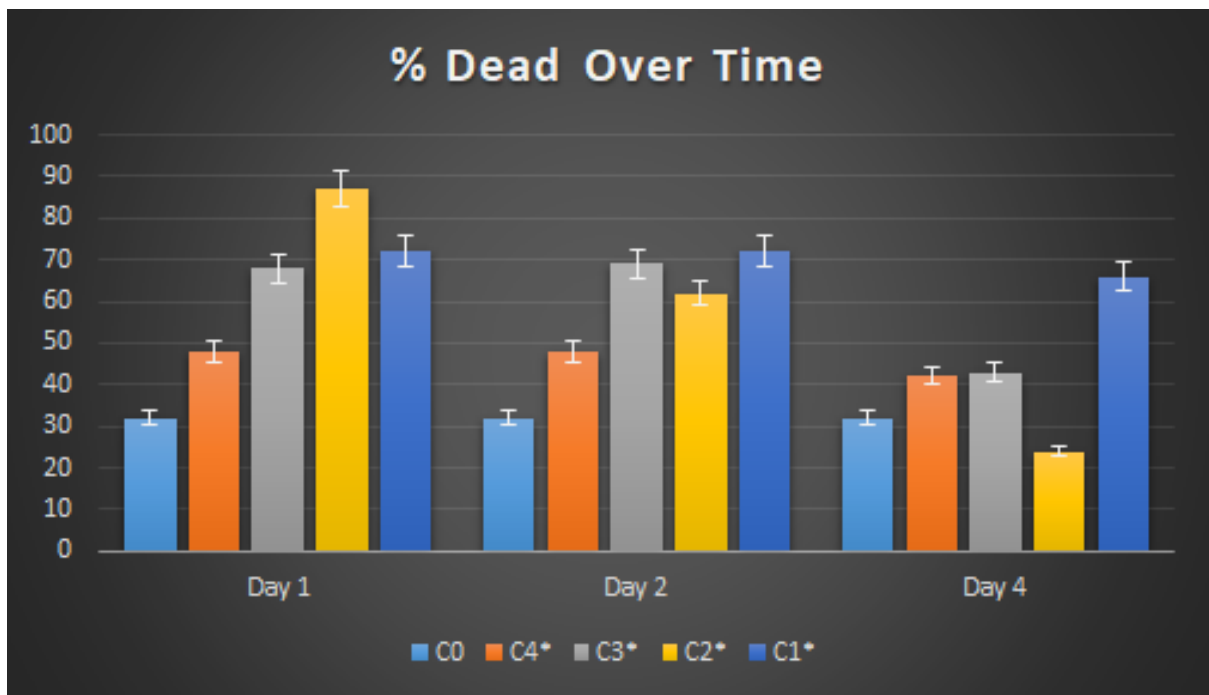


Figure 4.6: *Cell viability over four days when incubated with different concentrations of synthetic, sugar coated melanin granules:*

The data is plotted from decreasing concentration to increasing concentration of M@G particles, where C0 is the control sample containing no M@G. The percentage of dead cells is calculated according to the assay manual, briefly:

$$\text{percent Dead Cells} = (A - D) \div (C - D) \quad (14)$$

Where:

- A: Fluorescence at 645 nm in experimental sample, labeled with Calciem-AM and EthD
- C: Fluorescence at 645 nm in sample where all cells are dead, labeled with EthD only
- D: Fluorescence at 645 nm in a sample where all cells are dead, labeled with Calciem-AM only

It is clear from Figure 4.6 that above a certain threshold, higher concentrations of melanin have a negative effect on growth as soon as 24 hours after introducing melanin nanoparticles. However, as each well receives the same initial concentration of melanin, and as all wells are normalized to a ‘mostly alive’ and ‘mostly dead’ control, the confounding effects of melanin should be minimized. We can look at the absolute fluorescent intensity of the samples as normalized by the control sample, over time. This is based on the changing intensity of the longer wavelength (530 nm) fluorescence excitation compared with a population curve, due to the confounding effect of melanin particles in shorter wavelength regions:

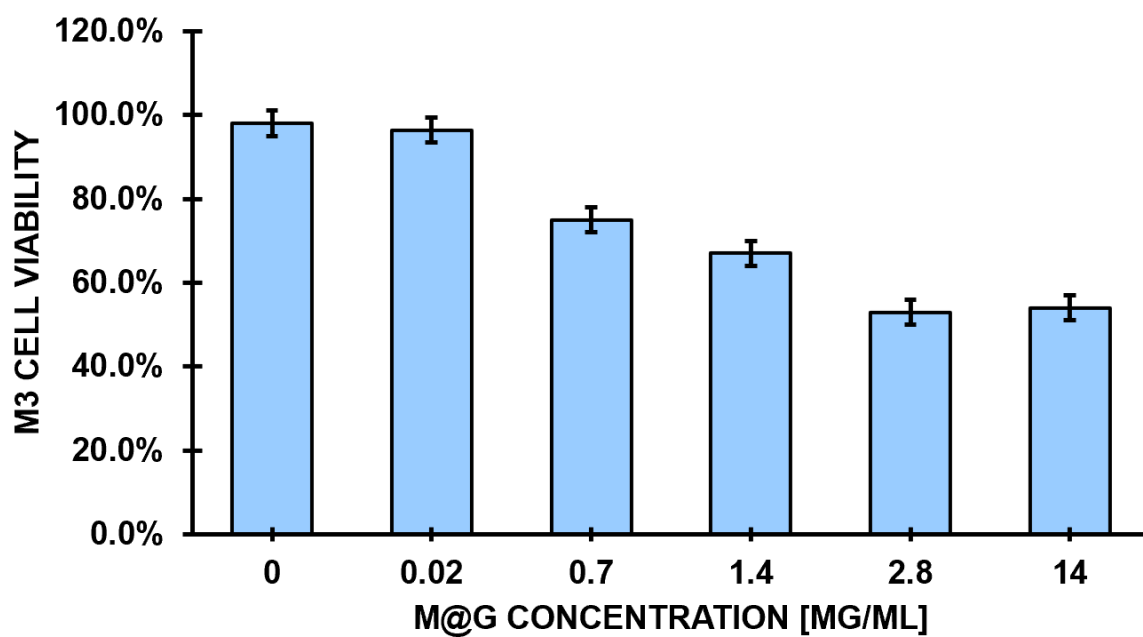


Figure 4.7: Nanoparticle Concentration Dependent Cell Viability after 24 hours

We see that after 24 hours, viability of samples fed M@G has decreased compared with control for cells fed above a threshold of 0.02 mg/mL. This concentration can also be represented in the context of the 96 well plate as 1.5 L M@G/well. When we consider cells seeded at a density of 10,000 cells/well, this concentration can be estimated as $0.5 \times 10^4 \mu\text{g}/10^6$ cells. is taken as the ‘upper limit’ dose, meaning this is used as the non-toxic dose for subsequent laser experiments.

Optical microscopy separately demonstrated that very high concentrations of M@G resulted in lack of cell proliferation over a period of four days:

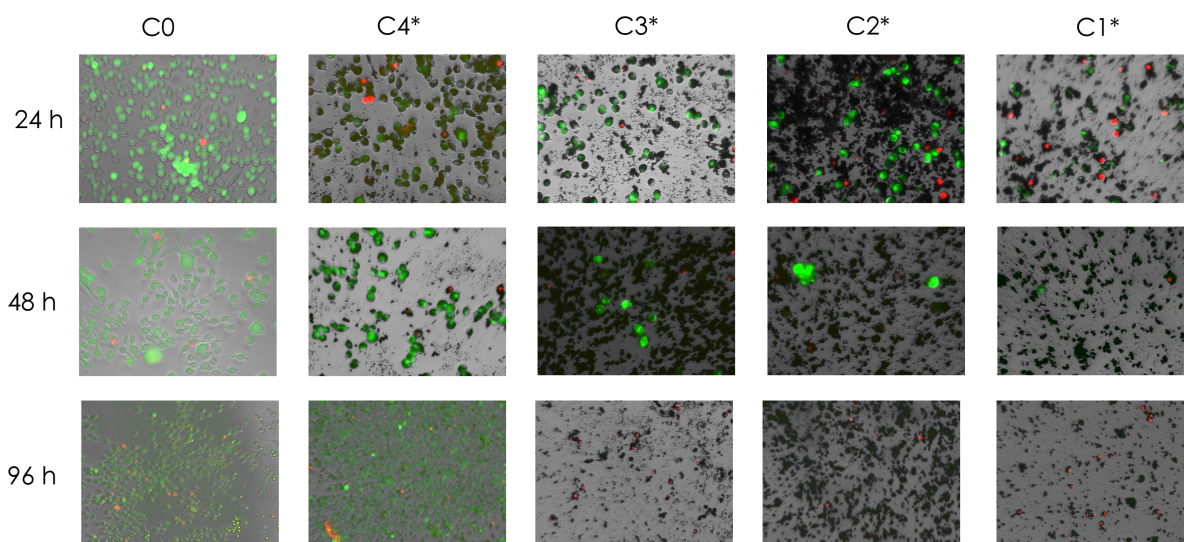


Figure 4.8: *EVOS fluorescent microscopy data taken at 10x magnification*: images as an orthogonal measure to Spectrophotometer data. One important observation is that cells below a certain threshold of melanin proliferate, and become over-confluent compared with the control cells. Focusing on C4* versus C0, we see that after 24 hours cells have developed processes, and are beginning to elongate in both the control and the M@G well with the lowest concentration of melanin. Cells that have higher concentrations are still alive 24h post treatment, as shown by the green fluorescence. However, these cells are more circular and display minimal processes. After 48 hours, populations with high concentrations (C1* and C2* are reduced to scattered cells, but they are not becoming confluent. By day 4 (96 h) the cells are largely dead. On the contrary, cells that took up C4 amounts of particles are confluent. Additionally, while M@G particles are relatively consistent in sizing when synthesized, their behavior in DMEM media is to begin to aggregate. The macrophages themselves appear to take up M@G in the cytoplasm (see discussion of VM-M3 uptake comparison with VM-NM), and when these cells are no longer viable, as in C2*, the general outline of the macrophages is sometimes clear. C1* appears to not have grown to this point.

Based on fluorescent assay data as well as qualitative visualization over time, a safe threshold of 0.02 mg/mL added M@G particles was determined for VM-M3 cells. This concentration was used in subsequent experiments.

4.6.3 VM-M3 Nanoparticle Uptake Quantification and Comparison with VM-NM1

The melanin uptake of VM-M3 cells was then compared with a related cancer cell line, VM-NM1 cells, which are a metastatic tumor cell line that differ from VM-M3 cells in that they do not exhibit macrophage behavior [87]. We incubated VM-NM1 cells with identical concentrations of M@G particles, and prepared them for z-stack imaging, in order to visually compare the inner structure of the cells and check for nanoparticle accumulation. See methods for fixation protocol.

4.6.3.1 Nanoparticle Uptake Quantification Analysis:

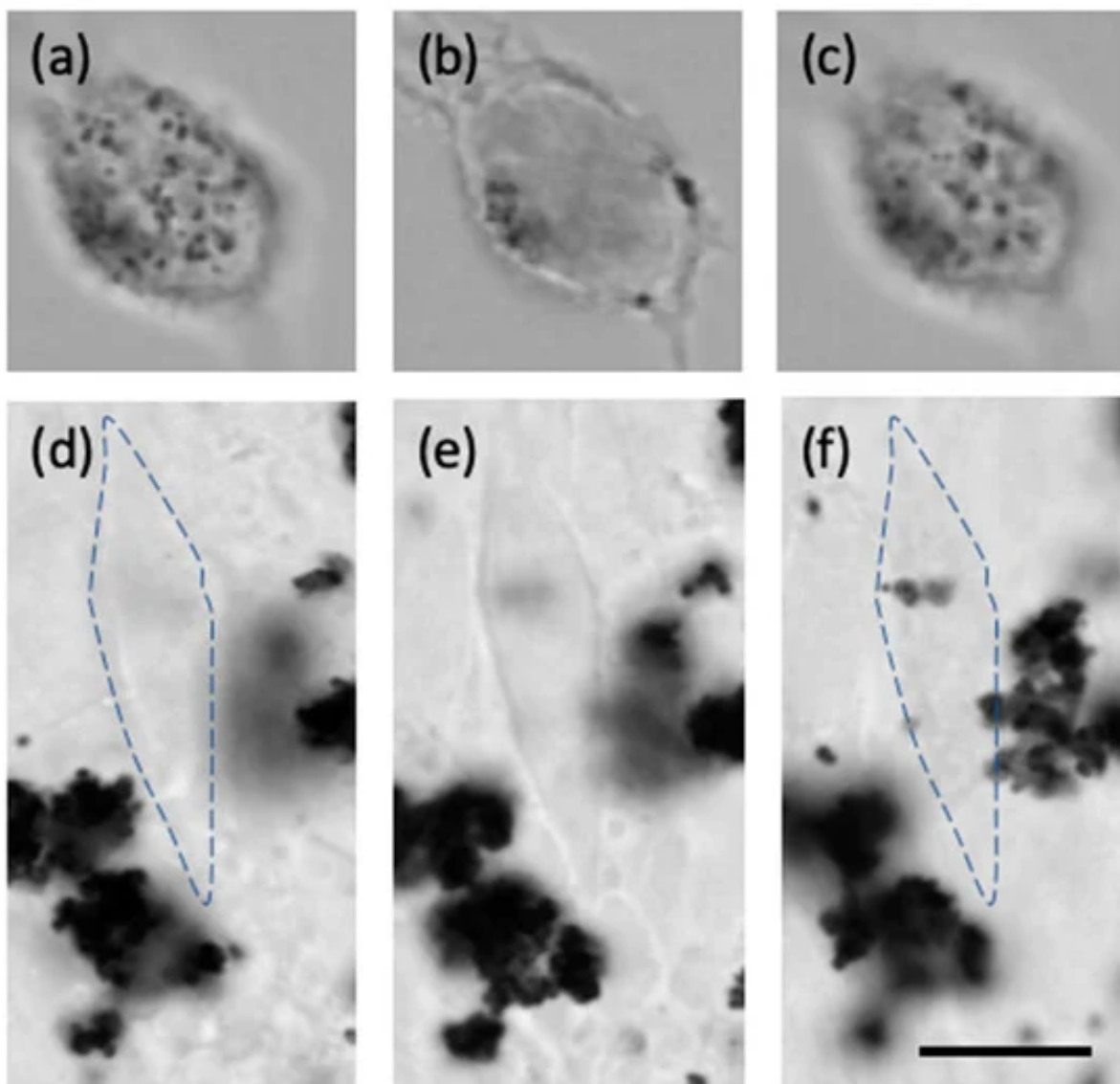


Figure 4.9: *Selected slices from a Z-stack image of cells.*: Sub-figures (a) (b) and (c) represent different height slices of a single VM-M3 cell. Black dots show the accumulation of melanin within the cell cytoplasm clearly in image (a) and (c), while figure (b) shows the attachment of large particles to the membrane of the cell, and smaller particles being absorbed. Sub-figures (d), (e), and (f) show a VM-NM cell incubated under identical conditions. For clarity, the membrane of the VM-NM cell is outlined in dark blue. Melanin aggregates from the media clump in vicinity of the cell, and are shown in dark black aggregates. Two smaller aggregates appear at the top of the cell membrane, but no pieces of melanin are observed within the cell. Scale bar $10\ \mu\text{m}$.

VM-M3 and VM-NM1 cells were compared against each other visually, and against control cells that were not incubated with melanin. Only the VM-M3 cell was demonstrated to consistently have dark particle accumulations consistent with melanin phagocytosis.

The exact quantification of nanoparticle uptake varied greatly among cells. This could be due to differences in cycle and phase of cells, as well as inhomogeneity of melanin dispersed throughout cell media over time. Furthermore, in looking at cells undergoing mitosis, it appeared that the nanoparticles thought to be located in the cytoplasm would randomly distribute between the dividing cells. Further study is required to capture the dynamics of accumulated melanin granules during cell division.

4.6.3.2 Particle Uptake Analysis via ImageJ:

To estimate the nanoparticle uptake within VM-M3 cells, a custom script was written in ImageJ to preform the analysis.

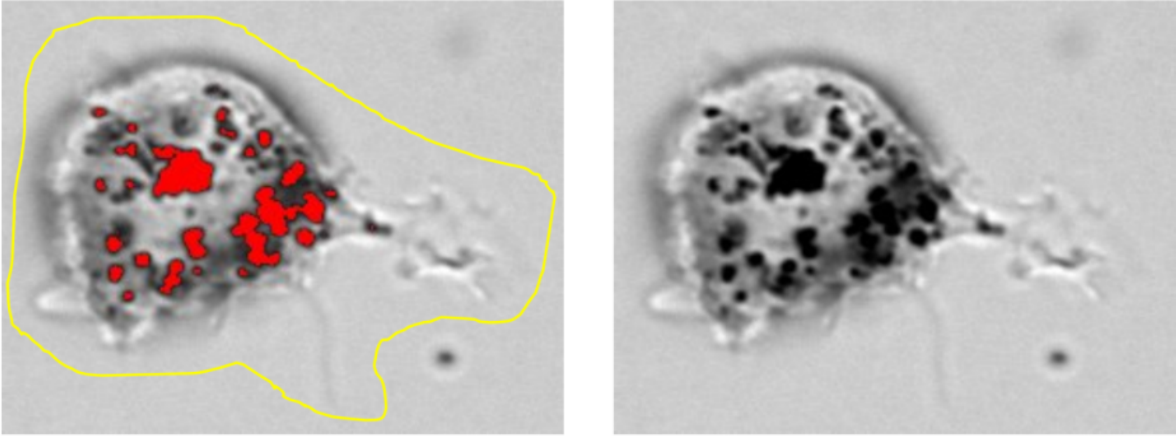
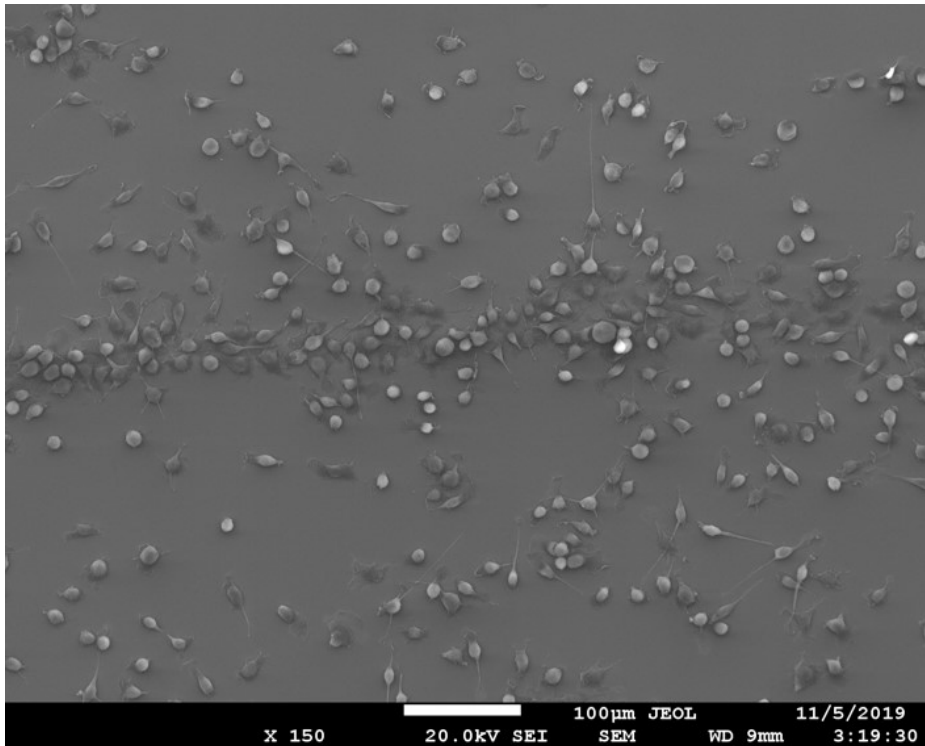


Figure 4.10: *Image Thresholding Algorithm*: In this example where the right-hand figure is a single slice from a z-stack array, and the left-hand figure is the ImageJ algorithm's determination of pixels corresponding to melanin nanoparticles (red). The yellow represents the region of interest, so pixels outside of this region are ignored by the algorithm.

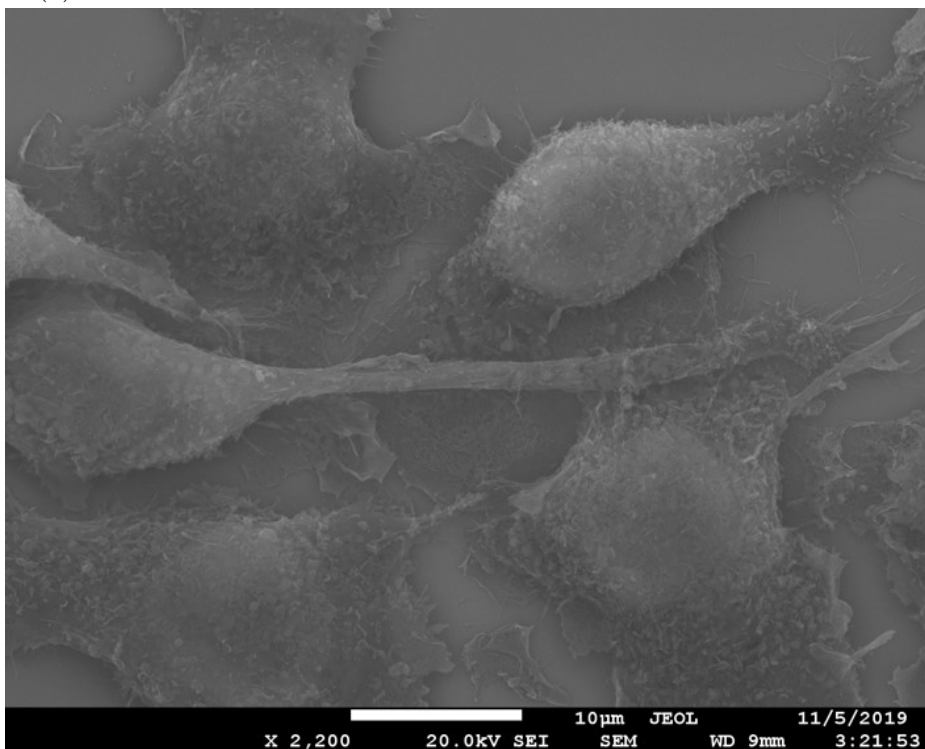
The cell is isolated in each image within a hand-drawn Region of Interest (ROI), outlined in yellow in Fig. 10, to exclude melanin aggregates from nearby media. A threshold value for melanin nanoparticle presence is set based on pixel grayscale value. Pixels that meet or are above the set threshold are identified by ImageJ and displayed in red in Fig. 10. The scaled area of these pixels was calculated to measure the area of the melanin particles for each image slice. To integrate these images across the height of the cell, each area of melanin particles per image was multiplied by the stack height, as specified by Zeiss software. For the specified figure, the distance between slices is $0.28\mu\text{m}$. This volume of calculated black dots for this image was calculated to be $4701\mu\text{m}^3$, which is approximately 10% of the cell when the cell volume is calculated using the same methods, but editing the threshold analysis to include the entire cell. If we take the average particle diameter to be 165nm , then we estimate a total of 1.99×10^6 particles within this cell.

4.6.3.3 Orthogonal Measure of Particle Uptake with Electron Microscopy

VM-M3 cells were fed melanin nanoparticles in the same manner as the z-stack analysis, but grown on a Si wafer substrate and fixed according to the electromagnetic microscopy fixation protocol described in methods. Melanin nanoparticles were not distinguished on the surface of VM-M3 cells under electron microscope investigation. The morphology of cells under electron microscope, shown in Figure 4.11 mimics closely the structure seen by live cells in the plate, but the surface of cells do not display conclusive markers of melanin particles. This likely due to either lack of contrast between polymeric melanin and the cell surface under electron microscopy, or due to the tendency of cells to internalize particles rather than attaching particles to the cell surface.



(a) SEM at 150x



(b) SEM at 2,200x

Figure 4.11: Scanning Electron Microscope images of VM-M3 cells fed with nanoparticles: various magnifications of VM-M3 cells.

4.6.3.4 Particle Uptake Discussion

An additional heuristic for nanoparticle uptake can be obtained when observing the concentration. For these experiments, the concentration of melanin added to media, as specified previously, was given to be $1.6 * 10^4 \mu\text{g}/10^6$ cells. If we take the density of melanin to be $1.6\text{g}/\text{cm}^3$, then the volume of available melanin per cell would average to $10,000\mu\text{m}^3$.

This uptake efficiency on the order of 50% *in vitro* is in agreement with melanin-based nanoparticle uptake efficiency across different studies, and is in fact somewhat superior to what is found in other melanin-nanoparticle methods, perhaps owing to the sugar coating. For example, Poinard et al found an uptake efficiency of 35.7% in bladder cancer cells *in vitro* when loading drugs coated with poly-dopamine derived melanin-like polymer [4]. This was a significant enhancement from 4.3% free form drug loading.

By preparing M@GC nanoparticles, we have demonstrated high-accumulation of particles within VM-M3 cells. This high accumulation is essential for effective photothermal efficiency. However, such a high accumulation can also disrupt cell function, which was not quantified via gene expression, but was demonstrated at a population level via fluorescence assay. Furthermore, due to melanin's opaque nature and auto fluorescence, determining an ideal dose required rigorous independent verification via combination of fluorescence-based, dye-based, and chemical-based assays.

4.7 Photothermal Experiment

To investigate the photothermal efficacy of cells containing melanin nanoparticles, it was important for an experimental set-up to have reliability and precision in radiation dose

dose. In this section we characterize the dose of radiation incident on the specimen is characterized by energy density, or energy per unit area. Some studies also use power density, or power per unit area. To accurately report energy per unit area, the measured power of the laser light where it is incident on cells, spot size, and length of radiation are necessary to characterize dose. Laser fluency from irradiation at 665 nm is reported by Poinard et al in recent photothermal investigation [4] .

4.7.1 Radiation Dose Characterization: Knife Edge Measurement

Please see Equipment and Methods for a discussion and schematic of the customized laser irradiation set-up. For an accurate understanding of the dose of radiation incident on a cell, a knife edge measurement was used to characterize the beam waist from the objective lens. Data from a knife-edge scan for our laser system is shown in Fig. 13.

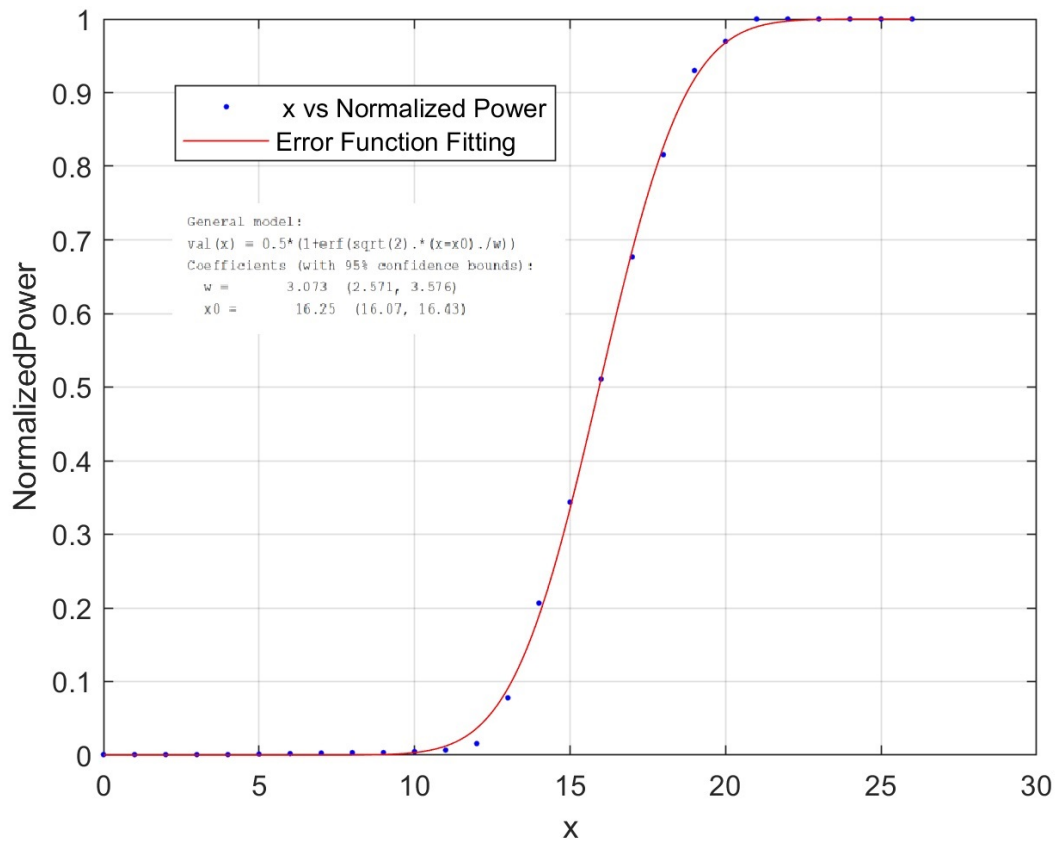


Figure 4.12: *Knife Edge Measurement*: Plot of power measured, in Watts (normalized from 0 to 1) vs x position in microns. Closed blue circles represent raw collected data, and the red line is the Error Function which is fit to the data according to the printed General Model. This measurement was done in triplicate, and then for varying heights. W is the calculated beam waist. It was found that the tightest spot corresponded to a beam waist of approximately $3.07 \pm 0.5 \mu\text{m}$

We measure the beam waist to be approximately $3\mu m \pm 0.5\mu m$, meaning that the highest intensity portion of the beam has a diameter of $6\mu m \pm 1\mu m$. It is important to note that a small beam diameter $6\mu m \pm 1\mu m$ focused with a high NA objective (NA = 1.25) is sufficient to create an optical tweezers set up when components are properly aligned. This implies that this set-up, in addition to heating components of a cell, has the potential to produce external forces on a biological cell. In our case, we are using a high power level CW laser, which heats cells on a relatively fast time scale, which is on the order of seconds. The forces on the cell are minuscule compared with the heat. This is demonstrated by the control cells being unaffected by laser irradiation. Due to set up limitations, experiments are not done in an incubated atmosphere, this causes stress on cells. It is necessary to limit the time cells spend outside of the incubator.

4.7.2 Photothermal Experiment Results

Melanin-containing VM-M3 cells were the first candidate for irradiation at 532 nm. Melanin-fed VM-M3 irradiation results were compared alongside an unfed control. Qualitative initial viability was tested with trypan blue exclusion. With the system described above, and melanin-containing cells underwent structural damage, documented with both trypan-blue exclusion. VM-M3 cells were irradiated at a power level of 121 mW for 30 seconds. After sufficiently long ($t > 45$ s), both control and non-pigmented cells underwent structural damage. However, melanin-containing underwent more severe structural damage, including exploding, at lower time ($t < 30$ s) and power thresholds.

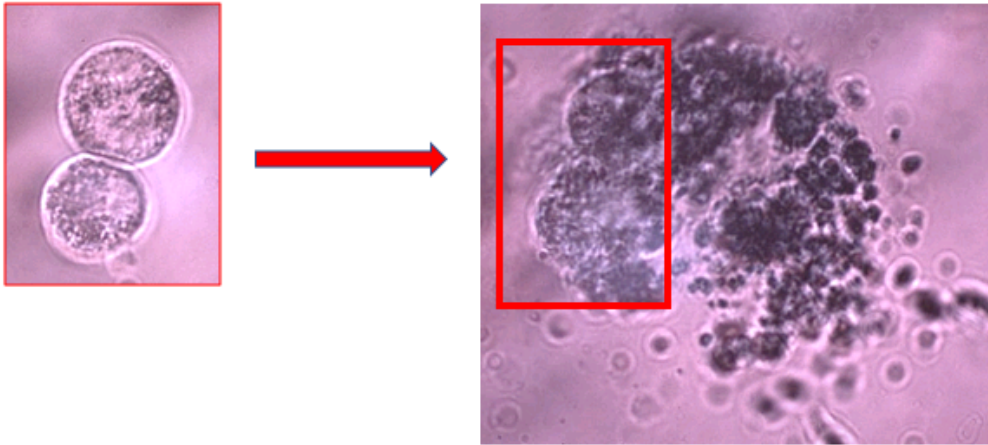


Figure 4.13: *Melanin-Containing VM-M3 cells before and 30 seconds after irradiation with a 532 nm laser at a power level of 121 mW* Cells were observed to explode and spill melanin along with other contents.

The proposed mechanism of damage is primarily thermal due to the engulfed melanin nanoparticle converting light energy to heat. Interestingly, some cells were observed to initially shrink, as if in hypertonic solutions, and then swell and explode, as if in a hypotonic solution, though the growth medium was consistent among all experiments. We define structural damage as both exploding and shrinking of cell membranes as a result of laser irradiation, similar to the effect of osmotic solutions that are not balanced within the inside of cells. One contributing factor accounting for these different responses could be phase of life in the cell cycle.

4.8 Study on Population of Cells

4.8.1 Device Fabrication

To track clusters of cells over time, it was necessary to fabricate custom devices for the purposes of cell transport to the microscope set-up, and tracking beyond laser experiments [93] [94] [95]. Initially, cells were divided into microfluidic chambers to allow for cell tracking. Each chamber was meant to house a population of cells, which would be prevented from signaling to cells in different chambers via a physical barrier of PDMS. PDMS chambers on a glass coverslip are shown in Figure 4.14

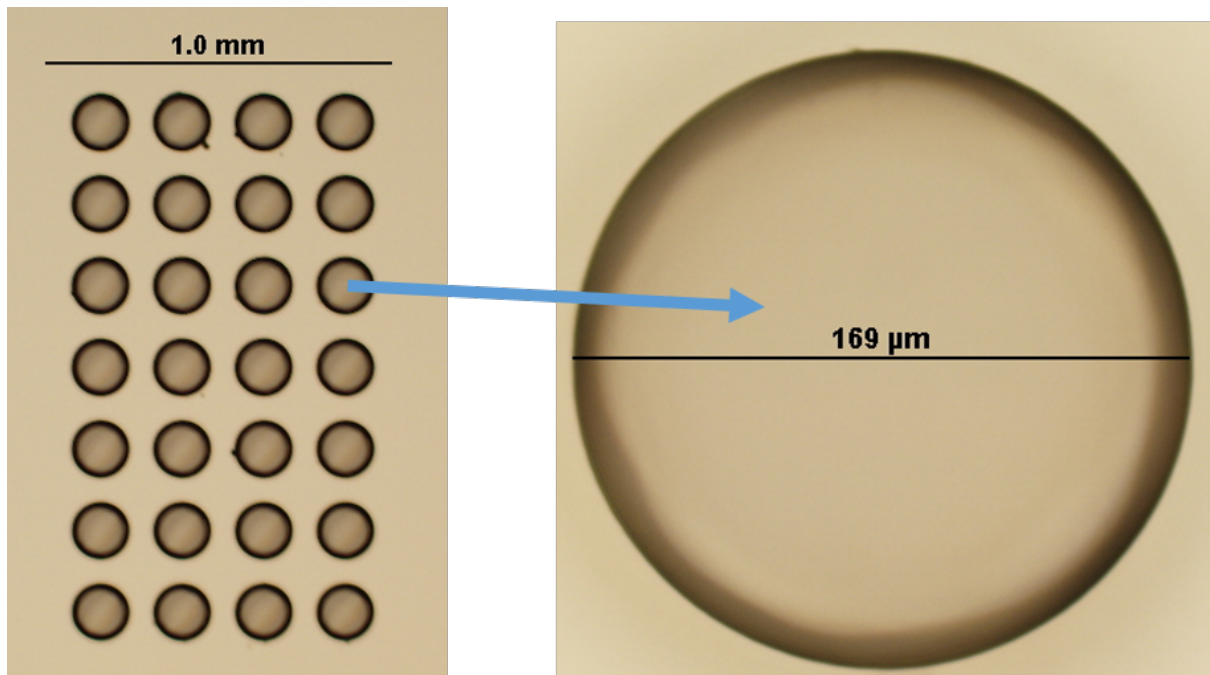


Figure 4.14: *Custom Microfluidic through-holes in PDMS for mammalian cell isolation and tracking*

In order for cells to obtain a good morphology in these glass-PDMS interface devices, it is necessary to coat the device in Type I Rat Collagen (Sigma-Aldrich, C3867), prepared according to manufacturers instructions, prior to cell incubation and adhesion.

PDMS is highly absorbing of the extracellular polymer matrix, which in turn is absorbing of the ethidium fluorescent protein in subsequent assays. This is displayed in the bright red halo surrounding PDMS chamber walls in Figure 4.15:

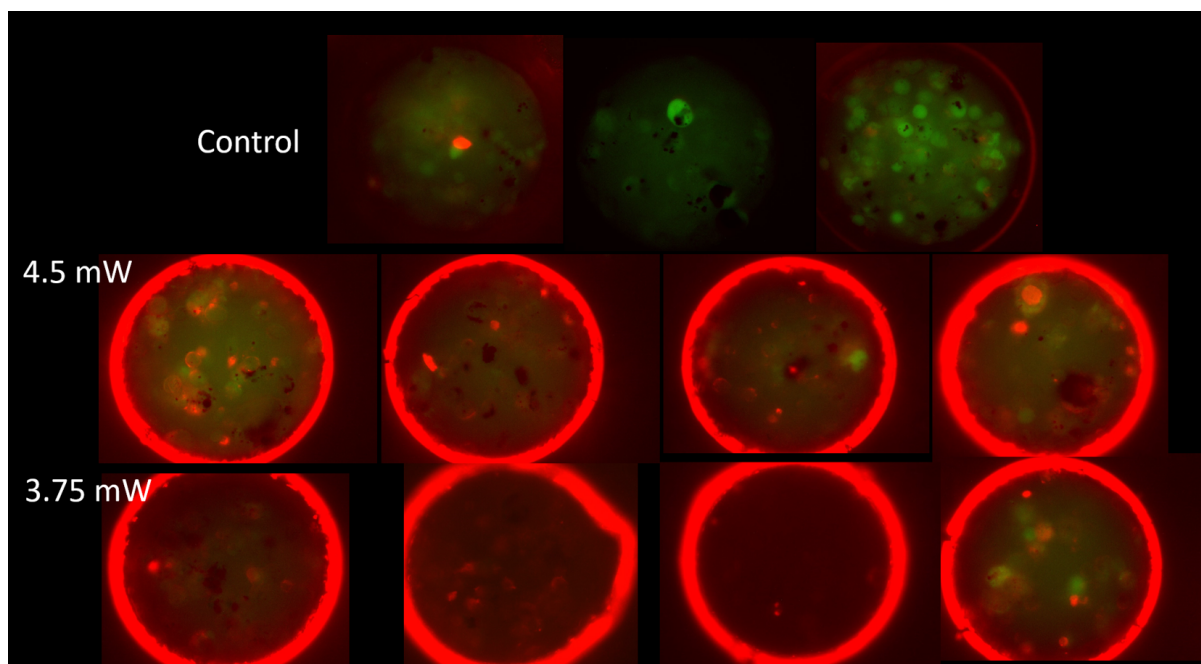
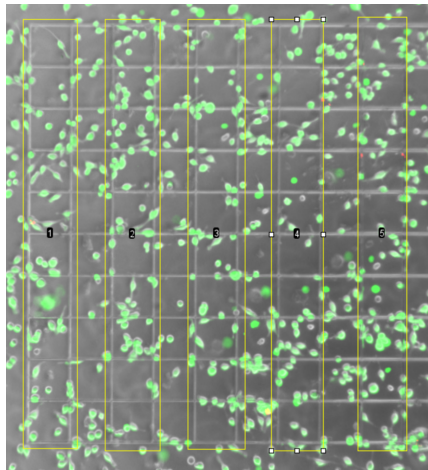


Figure 4.15: *Collagen and fluorophore auto fluorescence in PDMS devices interfering with fluorescent assay*

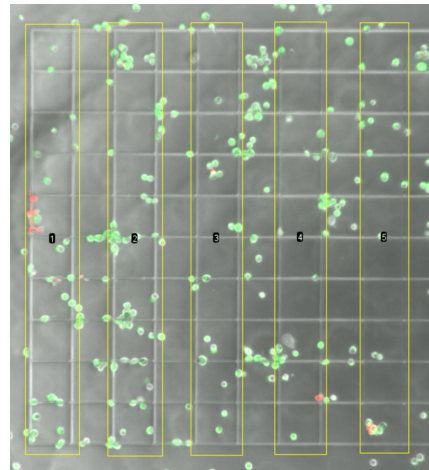
Ultimately, it was determined that a grid-based corning glass device with a PDMS support was sufficient for the experimental timeframe. The grid was significantly larger than the field of view used to collect fluorescent data, so any absorbance of the collagen-coated PDMS would not interfere with fluorescent images. However, the grid does not provide a barrier for cell signaling. Given sufficient time, cells from other areas can grow into previously irradiated sections of the grid, obfuscating results. Timing of fluorescent data collection is important for this method. For a discussion of gridded coverslip preparation, laser experiment procedure, see Methods.

4.8.2 Fluorescent Data

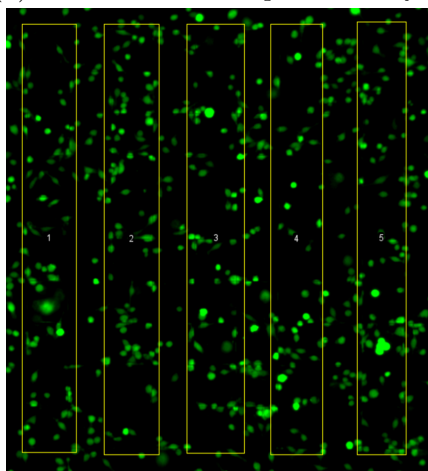
Cells were grown on gridded coverslips for the purpose of cell tracking over time. One column of the grid was selected to irradiate with a laser. The data in Figure 4.16 is shown post 24 hours of exposure to laser irradiation. The cells in column 1 were exposed to 55 mW for 5 s, and then incubated for 24 hours before fluorescent data was collected.



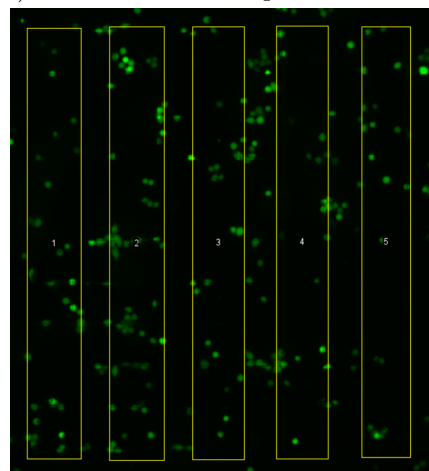
(a) *False Color Composite - Unfed*



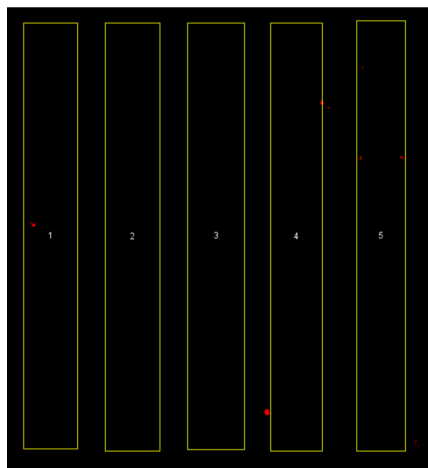
(b) *False Color Composite + M@G*



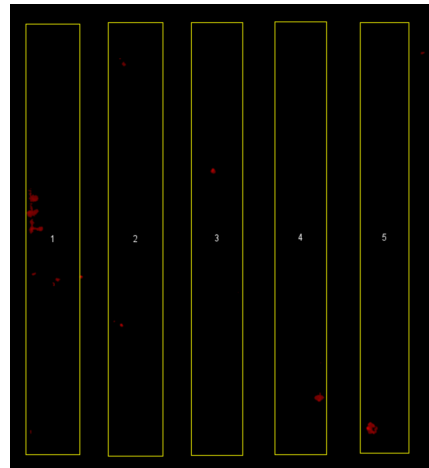
(c) *Calcein*



(d) *Calcein*



(e) *Ethidium*



(f) *Ethidium*

Figure 4.16: *Fluorescent Data on Gridded Coverslips from EVOS at 4x*: A comparison of growth response after 24 hours post laser treatment. On the lefthand side, panels a) c) e) show the response of VM-M3 cells after feeding with melanin, and laser irradiation in column 1. On the righthand side, panels b) d) f) show the response of unfed VM-M3 cells treated in the same conditions, with laser irradiation also in column 1. The top row, figures a) and b) are the false color composite overlay of the green fluorescent response from the Calcein dye, the red fluorescent response from the Ethidium dye, and the brightfield image of the cells from white light. The second row c) and d) displays the fluorescent signal from only the calcein dye, staining living cells. The third row e) and f) displays the fluorescent signal from only the ethidium dye, staining dead cell nuclei. Yellow rectangles guide the eye qualitatively to the five grid columns that are compared, and laser irradiation is constrained to the first column

This data is a representative sample of population data processing post laser irradiation. The first row represents an overlay of three separate images taken on the EVOS fluorescent microscope: one bright field and two fluorescent channels. The fluorescent channels are obtained by excitation with a diode, which is filtered from the final result. Images are recorded on greyscale, and colorized though ImageJ in post-processing.

For cells that were not fed particles, shown on the left-hand side, the ratio of dead to living cells is not statistically different between the first column, which received laser treatment, and the remaining columns 2, 3, 4, and 5. For cells that were pre-fed melanin, column 1 displays a larger cluster of dead cells, as noted by red dots, relative to the non-irradiated columns 2, 3, 4 or 5. Column 1 also displays living cells, as shown in the second row in green, at a comparable density to the remaining columns. In order to deconvolute the effect of cell migration and doubling time on the data, experiments were repeated with the timescale shortened between laser treatment and fluorescent assay.

4.8.3 Results

Results of population based experiments are shown in Figure 4.17. This data was taken 6 hours post laser treatment. The power density that cells received was $10^7 \text{ W}/m^2$. Cells were grown on gridded coverslips, and 5 samples were taken per treatment. The results are averaged in Figure 4.17.

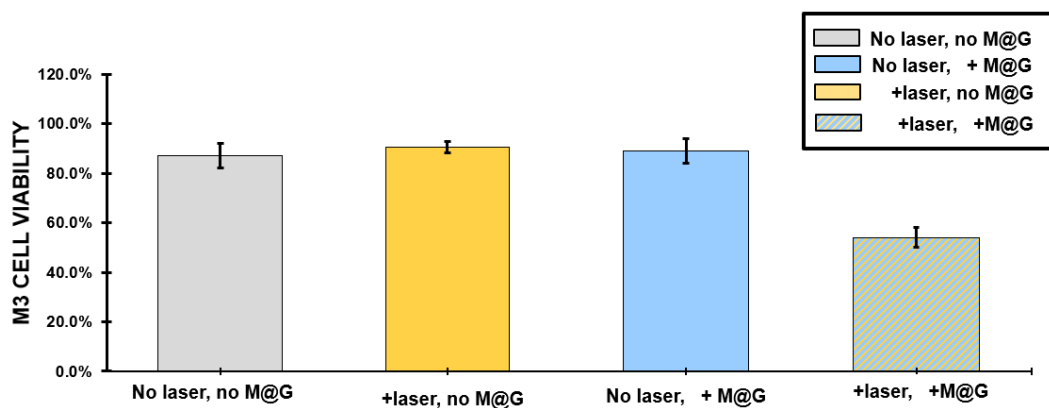


Figure 4.17: *Population of Cells post Treatment*: The data shown here represents the average change in population viability for cells in the gridded coverslip set-up. From left to right: The first column is a control, cells that were neither fed nanoparticles nor irradiated. The second column shows cells that recieved laser treatment, but were not fed melanin nanoparticles prior to irradiation. The third column shows cells that were fed nanoparticles, but not irradiated. The fourth column shows the result of both nanoparticle and laser treatment.

It is clear that at this low concentration of nanoparticles, sensitization is necessary in order for laser treatment at this power density to negatively impact cell viability. Nanoparticle treatment or laser treatment alone did not statistically effect viability at a population level, while the combination of nanoparticle and laser treatment statistically decreased cell viability.

4.9 Discussion

We have confirmed via precise z-stack optical microscopy that VM-M3 macrophage-like cells will take up melanin particles where they will aggregate within the cellular cytoplasm and vacuoles, and the proposed mechanism for this action is phagocytosis [86] . This mechanism can be exploited to further promote nanoparticle uptake with knowledge of the Warburg effect by coating particles with glucose. At non-toxic doses, particles will accumulate within the cell, but the cell will still be able to function and divide, passing particle aggregates to offspring. Glucose coated melanin nanoparticles, like their uncoated counterparts, convert light to heat efficiently. We have shown them to cause acute hyperthermia with 532nm CW laser irradiation over 5-30 second period, while not damaging healthy cells. If shorter, non-ionizing wavelengths can be delivered to target cells, then targeted cells will be selectively damaged when sensitized with melanin nanoparticles. Further considerations of this work, including discussions of *in vitro* and *in vivo* correlations, are proposed in the concluding chapter.

Chapter 5

Conclusions and Future Outlook

5.1 Conclusion

5.2 Summary

In chapter three, selective damage of biomolecules under the morse potential via non-ionizing radiation was discussed within the context of THz radiation was explored via simulation. It was shown that systems of this class, such as the DNA molecule undergoes a clear transition from linear response to a nonlinear domain, and within that nonlinear domain dissociation occurred at frequencies that were selective to the dynamics of the specific molecular bond. This work contributes to the theoretical framework of targeting bio-species by coupling molecular resonances to electromagnetic radiation. However, specific and targeted dissociation of complex biomolecules such as DNA with electromagnetic radiation is not experimentally feasible at this time. Experimental explanations and clarity regarding the interaction of THz radiation with biomolecules remain elusive for many reasons: 1) there are no standardized experimental protocols for studying the

interaction of THz with bio-organisms and, most importantly, 2) there are insufficient THz sources and tools available to enable an accurate assessment of initial functional states of the biological objects in question [17].

In the fourth chapter, selective damage through photothermal heating was demonstrated with the addition of biocompatible melanin nanoparticles to an *in vitro* model of malignant cancer. In this work, we demonstrated that malignant metastatic cancer cells spontaneously self-sensitize to radiation in the visible (or NIR) range by massively ingesting MNPs, which then acts as a highly absorbing dye. The process of the nanoparticle ingestion can be further enhanced by glucose coating. With increasing concentration, that glucose-coated MNPS exert a cytotoxic effect in cancer cells, even in the absence of radiation, when accumulation is high. Further action is needed to determine the mechanism for the ‘over-eating’ behavior that we see *in vitro*. In addition to exploring this mechanism *in vitro*, it remains to be seen how, if at all, the particles accumulate *in vivo*. We demonstrated theoretically and experimentally that moderate intensity visible radiation (532 nm), with power density 10^7 W/m² is safe for unfilled cells, but lethal to cells filled with MNPs. The MNP-filled cells dramatically overheat, leading to a rapid pressure increase due to vapor formation, and eventually lysis. Even higher power radiation leads to cell shrinking and melting.

5.3 Future Outlook

5.3.1 *In Vitro In Vivo* Correlation for Melanin Nanoparticle Photothermal Therapy

The melanin-nanoparticle assisted photothermal therapy method demonstrated in chapter four is highly target selective *in vitro*. One logical next step is the correlation of this method for an *in vivo* system. The demonstration of this experiment in a mouse model could support a basis for a novel photodynamic cancer therapy, targeting the circulating tumor cells, which mediate metastasis. In such a therapy, either metastatic cells from melanoma could be studied (self-sensitized CTCs), or non-melanin containing tumors could be loaded with nanoparticles via an intravenous injection. In one possible scenario one could expose the blood of the mouse model externally, in a dialysis-like scheme, since the radiation at the 532 nm wavelength does not penetrate the human tissue well. In any *in vivo* scenario, it would be necessary to investigate is the impact of healthy cells on melanin debris from particles either injected into the blood stream or into the tumor, or debris from target cells post radiation. What is the effect on leukocytes, and in particular of the myeloid lineage, or other macrophages in blood that might come in contact with these debris? If MNPs are injected intravenously into a tumor, must be understood whether existing macrophages in the blood stream would also internalize MNPs, and, if so, at what rate? Some existing work has investigated this specific uptake by shielding melanin nanoparticles in red-blood cell camouflaged lysosomes, and the specificity and uptake efficiency of this process should be compared with the selective preference of tumor cells to glucose coatings in accordance with the warburg effect [96]

A simplifying suggestion in place of the dialysis-like scheme would be to use longer wave-

length radiation. Looking in the 700-800 nm wavelength transmission window would allow a non-invasive version of this therapy due to longer penetration depth in skin, with a direct radiation exposure of a near skin vein (*e.g.* in the wrist) [97]. Melanin's broadband absorption decreases at higher wavelengths, so these nanoparticles would necessarily require more laser power, creating the need to investigate the correct input energy to balance absorption of melanin particles with surrounding chromophores. Future experiments will be designed to answer these questions, and in general would aim at reducing power levels at any chosen radiation frequency, so that an irreversible destruction can be achieved to the target cells, without affecting healthy cells. Proposed here cancer therapy via blood treatment, could dramatically reduce the chance of metastasis.

5.3.2 Nanoparticle Applications for Chronic Inflammation

A different avenue that this work could be applied to is the control, but not destruction, of targeted cells using light. Proposed here is the application of photo-electric particles toward control, but not killing, of macrophage cells. Macrophages part of the innate immune system, and active in inflammation and infection [98]. Chronic inflammation is associated with changes to macrophage phenotype within the body, with also accompanies obesity and insulin resistance, as well as the tumor environment in cancer [88] [99] [100]. The phenotype of the macrophage is important for how it plays a role in these diseases: for example, in cell culture the same macrophage cell contributed to the apoptosis of cancer cells when expressing a certain phenotype, but was protective toward tumor cells when differentiated into a different phenotype [98]. Previous studies have demonstrated the ability to control the phenotype of macrophages via ion channels, by using drugs which target ion-based membrane receptors such as potassium or calcium ion channels [101].

An alternate way to achieve this result is by creating a localized electric potential with a sufficiently dipolar distribution, which results in a current density that acts on voltage-sensitive ion channel [102]. Just as there exists a class of nanomaterials that effectively convert light to heat, there also exist nanomaterials that convert light to electricity—largely for the applications of solar technology. Instead of drug targeting, it may be possible to apply photo-electric nanoparticles toward the control of macrophage phenotype states.

To measure macrophage polarization states, there are a number of experimental tools, including microscopic, chemical, and fluorescent-based assays detailed in this work. Some measurable ways that distinct macrophage phenotypes differ is in their cell surface markers, secreted cytokines, and biological functions [103]. The methods used to sensitize materials to cells, functionalize their surfaces for enhanced uptake, and assess cell viability post nanoparticle treatment can also be applied toward assessing compatibility of photoelectric particles. Similarly, the experimental set-up used to couple light to biological cells *in vitro* for photothermal therapies could also be applied to photo-electric stimulation of cells.

Controlling macrophage polarization, as measured by resting membrane potential V_{mem} , has important implications for future therapies, and the extent to which one can control macrophage polarization bioelectrically remains largely unexplored [99].

Chapter 6

Works Cited

References

1. Nanomedicine Market Size, Growth | Global Industry Report, 2018-2025 Available from: <https://www.grandviewresearch.com/industry-analysis/nanomedicine-market>.
2. Kostevšek N (2020) A Review on the Optimal Design of Magnetic Nanoparticle-Based T2 MRI Contrast Agents. *Magnetochemistry* 6: 11.
3. Ou H, Li J, Chen C, et al. (2019) Organic/polymer photothermal nanoagents for photoacoustic imaging and photothermal therapy in vivo. *Sci China Mater* 62: 1740–1758.
4. Poinard B, Neo SZY, Yeo ELL, et al. (2018) Polydopamine Nanoparticles Enhance Drug Release for Combined Photodynamic and Photothermal Therapy. *ACS Appl Mater Interfaces* 10: 21125–21136.

5. Choi YH, Han H-K (2018) Nanomedicines: current status and future perspectives in aspect of drug delivery and pharmacokinetics. *Journal of Pharmaceutical Investigation* 48: 43–60.
6. Gabriele VR, Shvonski A, Hoffman CS, et al. (2020) Towards spectrally selective catastrophic response. *Phys Rev E* 101: 062415.
7. Gabriele VR, Mazhabi RM, Alexander N, et al. (2021) Light- and Melanin Nanoparticle-Induced Cytotoxicity in Metastatic Cancer Cells. *Pharmaceutics* 13: 965.
8. Electromagnetic radiation (2021) *Simple English Wikipedia, the free encyclopedia*.
9. Moan J, Peak MJ (1989) Effects of UV radiation on cells. *Journal of Photochemistry and Photobiology B: Biology* 4: 21–34.
10. Sowa P, Rutkowska-Talipska J, Sulkowska U, et al. (2012) Ionizing and non-ionizing electromagnetic radiation in modern medicine. *Polish Annals of Medicine* 19: 134–138.
11. Razhev AM, Chernykh VV, Bagayev SN, et al. (2017) Pulsed UV laser technologies for ophthalmic surgery. *J Phys: Conf Ser* 793: 012022.
12. Ryan JL (2012) Ionizing Radiation: The Good, the Bad, and the Ugly. *Journal of Investigative Dermatology* 132: 985–993.
13. Baskar R, Lee KA, Yeo R, et al. (2012) Cancer and Radiation Therapy: Current Advances and Future Directions. *Int J Med Sci* 9: 193–199.
14. Nomura S, Morimoto Y, Tsujimoto H, et al. (2020) Highly reliable, targeted photothermal cancer therapy combined with thermal dosimetry using a near-infrared absorbent. *Sci Rep* 10: 9765.

15. Pilát Z, Jonáš A, Ježek J, et al. (2017) Effects of Infrared Optical Trapping on *Saccharomyces cerevisiae* in a Microfluidic System. *Sensors* 17: 2640.
16. Griffiths PR, Haseth JAD (2007) Fourier Transform Infrared Spectrometry, John Wiley & Sons.
17. Cherkasova OP, Serdyukov DS, Ratushnyak AS, et al. (2020) Effects of Terahertz Radiation on Living Cells: a Review. *Opt Spectrosc* 128: 855–866.
18. Alexandrov BS, Phipps ML, Alexandrov LB, et al. (2013) Specificity and Heterogeneity of Terahertz Radiation Effect on Gene Expression in Mouse Mesenchymal Stem Cells. *Sci Rep* 3: 1184.
19. Ash C, Dubec M, Donne K, et al. (2017) Effect of wavelength and beam width on penetration in light-tissue interaction using computational methods. *Lasers Med Sci* 32: 1909–1918.
20. Effects of Pulsed Electromagnetic Field Therapy on Pain, Stiffness, Physical Function, and Quality of Life in Patients With Osteoarthritis: A Systematic Review and Meta-Analysis of Randomized Placebo-Controlled Trials | Physical Therapy | Oxford Academic Available from: <https://academic.oup.com/ptj/article-abstract/100/7/1118/5816580>.
21. Schena E, Saccomandi P, Fong Y (2017) Laser Ablation for Cancer: Past, Present and Future. *Journal of Functional Biomaterials* 8: 19.
22. Gamage S, Howard M, Makita H, et al. (2018) Probing structural changes in single enveloped virus particles using nano-infrared spectroscopic imaging. *PLOS ONE* 13: e0199112.

23. Lee SY, Yoon K-A, Jang SH, et al. (2009) Infrared spectroscopy characterization of normal and lung cancer cells originated from epithelium. *J Vet Sci* 10: 299–304.
24. Karsten AE, Singh A, Karsten PA, et al. (2013) Diffuse Reflectance Spectroscopy as a Tool to Measure the Absorption Coefficient in Skin: South African Skin Phototypes. *Photochemistry and Photobiology* 89: 227–233.
25. Kuo A, Silverberg N, Fernandez Faith E, et al. (2021) A systematic scoping review of racial, ethnic, and socioeconomic health disparities in pediatric dermatology. *Pediatric Dermatology* 38: 6–12.
26. Cargou S (2020) PDMS membrane: thickness of a spin coated PDMS layer. *Elveflow*.
27. Leica DM R Instructions (1999).
28. ZEISS Microscopy Online Campus | Microscopy Basics | Kohler Illumination Available from: <http://zeiss-campus.magnet.fsu.edu/articles/basics/kohler.html>.
29. DNA (2022) *Wikipedia*.
30. Ward JF (1988) DNA Damage Produced by Ionizing Radiation in Mammalian Cells: Identities, Mechanisms of Formation, and Reparability, In: Cohn WE, Moldave K (Eds.), *Progress in Nucleic Acid Research and Molecular Biology*, Academic Press, 95–125.
31. Tapia-Rojo R, Mazo JJ, Falo F (2010) Thermal and mechanical properties of a DNA model with solvation barrier. *Phys Rev E* 82: 031916.

32. Zhou Y, Karplus M, Ball KD, et al. (2002) The distance fluctuation criterion for melting: Comparison of square-well and Morse potential models for clusters and homopolymers. *J Chem Phys* 116: 2323–2329.
33. Implementation of a Morse potential to model hydroxyl behavior in phyllosilicates: The Journal of Chemical Physics: Vol 130, No 13 Available from: https://aip.scitation.org/doi/full/10.1063/1.3103886?casa_token=RiIrAFfMFBAAAAAA%3A08_nvj4JUKFLvpm2KhwiWJLUNrkCp4QSFTDUN4Gl-OARZ7Aa1baHI5yssLRatcqP0HLJ2pPrcw.
34. Classical Motion under a Morse Potential | Nature Available from: <https://www.nature.com/articles/1801352a0>.
35. Mandziuk M, Schlick T (1995) Resonance in the dynamics of chemical systems simulated by the implicit midpoint scheme. *Chemical Physics Letters* 237: 525–535.
36. Ginzburg LR, Gromov M (1979) Structural Stability and Morphogenesis. An Outline of a General Theory of Models. Rene Thom , D. H. Fowler. *The Quarterly Review of Biology* 54: 126–127.
37. Symon, Mechanics, 3rd Edition | Pearson Available from: <https://www.pearson.com/us/higher-education/program/Symon-Mechanics-3rd-Edition/PGM18050.html>.
38. Solid State Physics - 1st Edition Available from: <https://www.elsevier.com/books/solid-state-physics/burns/978-0-12-146071-6>.
39. Swanson ES (2011) Modeling DNA response to terahertz radiation. *Phys Rev E* 83: 040901.

40. Lie GC, Yuan J (1986) Bistable and chaotic behavior in a damped driven Morse oscillator: A classical approach. *J Chem Phys* 84: 5486–5493.
41. Morse potential in DNA molecule – An experiment proposal | SpringerLink Available from: <https://link.springer.com/article/10.1007/s12038-012-9232-4>.
42. Peyrard M, Bishop AR (1989) Statistical mechanics of a nonlinear model for DNA denaturation. *Phys Rev Lett* 62: 2755–2758.
43. Ayyappan N, Maria Joy C, Kavitha L (2022) Stability analysis of DNA with the effect of twist and Morse potential. *Materials Today: Proceedings* 51: 1793–1796.
44. Lin W (2015) Introduction: Nanoparticles in Medicine. *Chem Rev* 115: 10407–10409.
45. Caldas M, Santos AC, Veiga F, et al. (2020) Melanin nanoparticles as a promising tool for biomedical applications - a review | Elsevier Enhanced Reader. *Acta Biomaterialia* 105: 26–43.
46. Rauscher H, Sokull-Klüttgen B, Stamm H (2012) The European Commission’s recommendation on the definition of nanomaterial makes an impact. *Nanotoxicology* 7: 1195–1197.
47. Modena MM, Rühle B, Burg TP, et al. (2019) Nanoparticle Characterization: What to Measure? *Advanced Materials* 31: 1901556.
48. Pharmacology CDDWCYRKD of, Pharmacy C of, University KH, et al. (2019) Research Outreach, Using photodynamic therapy to target circulating tumour cells, 2019. Available from: <https://researchoutreach.org/articles/using-photodynamic-therapy-to-target-circulating-tumour-cells/>.

49. Photodynamic Therapy | JNCI: Journal of the National Cancer Institute | Oxford Academic Available from: <https://academic.oup.com/jnci/article/90/12/889/960771?login=true>.
50. Dolmans DEJGJ, Fukumura D, Jain RK (2003) Photodynamic therapy for cancer. *Nat Rev Cancer* 3: 380–387.
51. Lucky SS, Soo KC, Zhang Y (2015) Nanoparticles in Photodynamic Therapy. *Chem Rev* 115: 1990–2042.
52. Cline B, Delahunty I, Xie J (2019) Nanoparticles to mediate X-ray-induced photodynamic therapy and Cherenkov radiation photodynamic therapy. *WIREs Nanomedicine and Nanobiotechnology* 11: e1541.
53. Yang X, Yang M, Pang B, et al. (2015) Gold Nanomaterials at Work in Biomedicine. *Chem Rev* 115: 10410–10488.
54. Norouzi H, Khoshgard K, Akbarzadeh F (2018) In vitro outlook of gold nanoparticles in photo-thermal therapy: a literature review. *Lasers Med Sci* 33: 917–926.
55. Kim HS, Lee DY (2018) Near-Infrared-Responsive Cancer Photothermal and Photodynamic Therapy Using Gold Nanoparticles. *Polymers* 10: 961.
56. Photodynamic effect of functionalized single-walled carbon nanotubes: a potential sensitizer for photodynamic therapy - Nanoscale (RSC Publishing) DOI:10.1039/C3NR06835H Available from: https://pubs.rsc.org/en/content/articlehtml/2014/nr/c3nr06835h?casa_token=iXe3EdyVzEcAAAAA:tbxrzQNwOA195TlRupbRsSLBDAwU7zFlh4pSymu8Pu7ouFrf_8hTpPjMbh3mL9nv8v3vdb5a40A4.